AEDC-TR-69-225

AN EXPERIMENTAL INVESTIGATION OF SURFACE CONDITIONS ON HYPERBOLOIDS AND PARABOLOIDS AT A MACH NUMBER OF 10

Herbert R. Little

ARO, Inc.

January 1970

VON KÁRMÁN GAS DYNAMICS FACILITY

ARNOLD ENGINEERING DEVELOPMENT CENTER

AIR FORCE SYSTEMS COMMAND

ARNOLD AIR FORCE STATION, TENNESSEE

NOTICES

When U. S. Government drawings specifications, or other data are used for any purpose other than a definitely related Government procurement operation, the Government thereby incurs no responsibility nor any obligation whatsoever, and the fact that the Government may have formulated, furnished, or in any way supplied the said drawings, specifications, or other data, is not to be regarded by implication or otherwise, or in any manner licensing the holder or any other person or corporation, or conveying any rights or permission to manufacture, use, or sell any patented invention that may in any way be related thereto.

Qualified users may obtain copies of this report from the Defense Documentation Center.

References to named commercial products in this report are not to be considered in any sense as an endorsement of the product by the United States Air Force or the Government.

AN EXPERIMENTAL INVESTIGATION OF SURFACE CONDITIONS ON HYPERBOLOIDS AND PARABOLOIDS AT A MACH NUMBER OF 10

Herbert R. Little
ARO, Inc.

FOREWORD

The research reported herein was sponsored by Headquarters, Arnold Engineering Development Center (AEDC), Air Force Systems Command (AFSC), Arnold Air Force Station, Tennessee, under Program Element 62201F, Project 8953, Task 03.

The results of the research were obtained by ARO, Inc. (a subsidiary of Sverdrup & Parcel and Associates, Inc.), contract operator of AEDC, AFSC, under Contract F40600-69-C-0001. The work was performed under ARO Project Nos. VT5703 and VT5818 during the period from April 1967 through January 1969. The manuscript was submitted for publication on September 9, 1969.

Portions of the material herein were presented as a thesis in partial fulfillment of the requirements for the degree of master of science from The University of Tennessee Space Institute.

The author would like to express his appreciation to Mr. Jack D. Whitfield, chief of the von Kármán Facility, and Dr. Wendell S. Norman, Manager of the Hypervelocity Branch, for their support; to Mr. B. J. Griffith, Assistant Manager, Hypervelocity Branch, and Dr. Clark H. Lewis of the Virginia Polytechnic Institute for their invaluable assistance in establishing the goals of the experiments; to Dr. John C. Adams, Supervisor, Theoretical Gas Dynamics Section, for the use of some numerical results; and to Messrs. R. K. Matthews and D. E. Boylan of the von Kármán Facility for the use of some previously unpublished data. Special thanks are expressed to Mr. James R. Wolfe for his care in the machining and fabrication of all the models used in this study, to Mr. Allen D. Thomas, for many helpful suggestions on model construction details, and to the wind tunnel operating personnel for their efforts in obtaining the data in this study.

This technical report has been reviewed and is approved.

David C. Reynolds
1st Lt, USAF
Research Division
Directorate of Plans
and Technology

Harry L. Maynard
Colonel, USAF
Director of Plans
and Technology

ABSTRACT

Data on analytic bodies are presented for Reynolds numbers from 22 to 65,000 (based on model nose radius) at a Mach number of 10. The test bodies are hyperboloids having asymptotic half-angles of 10, 22.5, and 45 deg and paraboloids; data are presented for steady-state skin temperatures, surface pressures, drag, and total skin friction. Shock-layer pitot pressure distributions are presented for two hyperboloids at selected Reynolds numbers. The results include an assessment of the modified Newtonian impact theory for use in inviscid pressure distributions. The effects of viscous interactions on skin temperature, pressure, drag, and skin friction are examined. Comparisons with numerical results of second-order boundary-layer and fully viscous shock-layer theories are made.

CONTENTS

APPENDIXES

I. ILLUSTRATIONS

Figure

NOMENCLATURE

A	Surface area, in.^{2}
A_B	Base area, πR_B^2, in.^{2}
a	Constant in equation of hyperbola (Eq. 1)
B_0, B_1, B_2, B_3	Constants in polynomial curve fit for paraboloid drag
b	Constant in equation of hyperbola (Eq. 1)
C_D	Drag coefficient, $D/q_\infty A_b$
C_{D_p}	Pressure drag coefficient
C_{D_T}	Total drag (pressure plus friction) obtained by direct measurement
C_f	Skin friction coefficient
C_∞	Form of Chapman-Rubesin viscosity coefficient $(\mu_w/\mu_\infty)(T_\infty/T_w)$
C_*	Form of Chapman-Rubesin viscosity coefficient $(\mu_*/\mu_\infty)(T_\infty/T_*)$ (Ref. 31)
D	Drag force, lb
D_B	Base diameter, $2R_B$, in.
d	Power in curve fit of pressure data (Eq. 10)
H_o	Stagnation enthalpy, ft^2/sec^2
K_n	Knudsen number
k_1, k_2	Constants in curve fit of hyperboloid drag data (Eq. 12)
L	Axial length, in.
M_∞	Free-stream Mach number
P	Constant in equation of parabola (Eq. 2)
p_1	Pressure at orifice, lb/in.^{2}
p_2	Pressure at transducer, lb/in.^{2}
p_o	Reservoir pressure, lb/in.^{2}
p_o'	Stagnation pressure behind a free-stream normal shock, lb/in.^{2}

p_T	Pitot pressure in shock layer of model, lb/in.^{2}
p_w	Static pressure at model surface, lb/in.^{2}
p_∞	Free-stream static pressure, lb/in.^{2}
q_∞	Free-stream dynamic pressure, $1/2\ (\rho_\infty U_\infty^2)$, lb/in.
R_B	Base radius of test body 0.300 in., in.
R_{B_L}	Base radius of model, in.
Re_2	Shock Reynolds number, $\rho_\infty U_\infty R_N/\mu_o$
Re_∞	Unit free-stream Reynolds number, $\rho_\infty U_\infty/\mu_\infty$ 32.2 x 12, in.$^{-1}$
$Re_{\infty, D}$	Free-stream Reynolds number based on base diameter
$Re_{\infty, L}$	Free-stream Reynolds number based on model length
Re_{∞, R_N}	Free-stream Reynolds number based on nose radius
R_N	Stagnation point radius of curvature, in.
R_w	Local model radius, in.
r	Radial coordinate in axisymmetric system
S	Surface distance, in.
T_1	Temperature at orifice, °K
T_2	Temperature at transducer, °K
T_o	Stagnation temperature, °K
T_w	Steady-state wall temperature, °K
T_∞	Free-stream static temperature, °K
U_∞	Flow velocity, ft/sec
$\bar{v}_\infty$	Viscous interaction parameter, $M_\infty \sqrt{C_\infty/Re_{\infty, L}}$
$\bar{v}_*$	Viscous interaction parameter, $M_\infty C_*/\sqrt{Re_{\infty, L}}$ (Ref. 31)
x	Abscissa in two-dimensional system
Y	Distance normal to model surface, in.
y	Ordinate in two-dimensional system
Z	Axial coordinate in axisymmetric system
ϵ	Van Dyke expansion parameter
θ_A	Asymptotic half-angle of hyperboloid, deg

θ_w	Local wall angle, deg
μ_o	Viscosity at stagnation temperature, lb-sec/ft^2
μ_w	Viscosity at model wall temperature, lb-sec/ft^2
μ_∞	Viscosity at free-stream temperature, lb-sec/ft^2
ρ_∞	Free-stream density, lb-sec^2/ft^4
ϕ	Sweep angle generating bodies of revolution, deg

SUBSCRIPTS

EXP	Experimental
N	Newtonian impact theory
o	Stagnation condition
w	Condition at model wall

SUPERSCRIPT

*	Distance normalized by stagnation point radius of curvature

SECTION I
INTRODUCTION

The last decade has seen a tremendous emphasis placed on the problems of hypersonic flight and reentry, particularly for blunt, slender bodies. Since early efforts to analytically describe the flows about such bodies were unsuccessful, designers relied heavily on experimental data. In recent years, however, theories have been advanced which have promise of adequately describing surface conditions and flow fields. For example, Lewis and Whitfield (Ref. 1) presented numerical results which approximated the surface conditions on, and flow field about, a short, 9-deg half-angle blunt cone to a fair degree. Their approach, however, was limited by the fact that it did not properly account for the interaction between the viscous (boundary-layer) flow and the inviscid (outer) flow. The interaction was significantly affected by shock-induced vorticity. Earlier, Davis and Flügge-Lotz (Ref. 2) had presented second-order solutions for the stagnation regions of blunt axisymmetric bodies following the theory of van Dyke (Ref. 3). Their method was extended by Lewis (Ref. 4) and Adams (Ref. 5) to include downstream portions of blunt bodies. Davis (Ref. 6) quite recently published solutions of the fully viscous shock-layer problem.

Of the above mentioned works, only those of Lewis and Whitfield (Ref. 1) and Lewis (Ref. 4) provided comparisons with experimental data. Even in those two cases, the comparisons are hampered by the lack of consistent experimental data representing a wide range of conditions. There are, in fact, very few examples of experimental data which are adequate in scope to allow meaningful comparisons with theoretical solutions.

The present work was undertaken to provide a comprehensive set of experimental data which could define surface conditions from the near-inviscid, or thin boundary-layer, regime to the fully viscous shock-layer regime, where the boundary layer extends from the body to the shock. The flow regimes, which depend on the rarefaction of the free-stream flow and the bluntness of the body, cannot be defined exactly, but only approximately. To accomplish this purpose, a Mach number of 10 was chosen, because it is high enough to be considered hypersonic and because a sufficient range of Reynolds numbers is obtainable at that Mach number in the VKF wind tunnels. The models which were used were analytic bodies, specifically hyperboloids and paraboloids, because their continuous geometries are easily handled numerically. (See, for example, the results of the AGARD Seminar on Numerical Methods for Viscous Flows, Teddington, England, September 18-21, 1967.)

The data to be presented are for hyperboloids having asymptotic half-angles of 10, 22.5, and 45 deg and for paraboloids; included are drag, pressure, and skin temperature measurements for Reynolds numbers from 60,000 to 22, based on model nose radius. The data were obtained at steady-state conditions. Mach number variations are from 9.19 to 10.12. Skin friction, which could not be measured directly, is calculated indirectly. The drag is measured on a family of models, each having the same nose radius and asymptotic angle but different lengths. From the difference between integrated pressure distributions over the longest model of the family (denoted as test body) and the measured drag distribution, a distribution of skin friction drag is obtained. The local skin friction is then calculated numerically. Several shock-layer pitot surveys are presented for high Reynolds number conditions on the 10- and 45-deg hyperboloids.

Any time experimental data from a single source are used for reference purposes, there exists the possibility of consistent errors or misleading information concerning test conditions, methods of data reduction, or data corrections. To lessen the possibility of such an occurrence, all pertinent test conditions are explained as to source and method of calculation, experimental data are tabulated in corrected and uncorrected forms, and all basic data plots are presented with grids to facilitate reading.

SECTION II
DESCRIPTION OF EXPERIMENTAL APPARATUS

2.1 WIND TUNNELS

2.1.1 Tunnel C

The hypersonic wind tunnel used for the high Reynolds number portion of the testing is designated as the Gas Dynamic Wind Tunnel, Hypersonic (C) and is illustrated in Fig. 1, Appendix I. It is a continuously operating, closed-circuit facility which operates at stagnation pressures from 200 to 1800 psia (pounds per square inch, absolute) and at stagnation temperatures of about 1000°K. The test gas (air) is expanded through an axisymmetric contoured nozzle to a nominal Mach number of 10 in the 50-in.-diam test section. Reynolds numbers of 25,800 and 126,700 per inch were obtained by varying the reservoir supply pressure. Sting mounted models may be inserted into the free stream from a model installation tank which permits model changes or repairs to be made while the tunnel is in operation. Detailed information

regarding the design and operation of Tunnel C is included in the report by Sivells (Ref. 7).

2.1.2 Tunnel L

Low Reynolds number data were taken in the Gas Dynamic Wind Tunnel, Hypersonic (L), shown in Fig. 2. It is a low density, hypersonic, continuous flow, arc-heated, ejector-pumped facility, which uses nitrogen or argon as the test gas. Two contoured nozzles were used in the present investigations. The nozzles differ in the Reynolds numbers available; one has a unit Reynolds number of about 400 per inch, and the other has Reynolds numbers of 1000, 1600, and 3000 per inch. The small inviscid core in each limited model size to a maximum diameter of 0.600 in. For the conditions tested, impact pressure surveys of the nozzles have revealed no gradients in the region occupied by the models or their flow fields. A detailed description of the design and preliminary calibration of Tunnel L is given by Potter, et al. (Ref. 8).

2.2 MODELS

In general, each type of data (drag, surface pressure, or skin temperature) required a different model construction technique; significant details of fabrication are discussed later in this section. The forebody surface geometries, however, had a common source: all were generated from hyperbolas or parabolas. In dimensional form, these may be expressed as

$$x^2/a^2 - y^2/b^2 = 1 \qquad \text{(hyperbola)} \qquad (1)$$

$$x = 2P\,y^2 \qquad \text{(parabola)} \qquad (2)$$

In Fig. 3, the details of the geometries are shown; note that the axisymmetric coordinates originate at the intersection of the hyperboloid with the x-axis rather than at the apex of the asymptotic cone. The models will be referred to as hyperboloids and paraboloids, since the names imply bodies of revolution. In discussion and display of the data, body coordinates will be normalized by the nose radius, $R_N = b^2/a$ (hyperboloid) and $R_N = 2P$ (paraboloid).

In all, almost one hundred models were tested; the geometries and type of data obtained on each are tabulated in Appendix II. The large number of models involved required the use of a coded denotation to identify each:

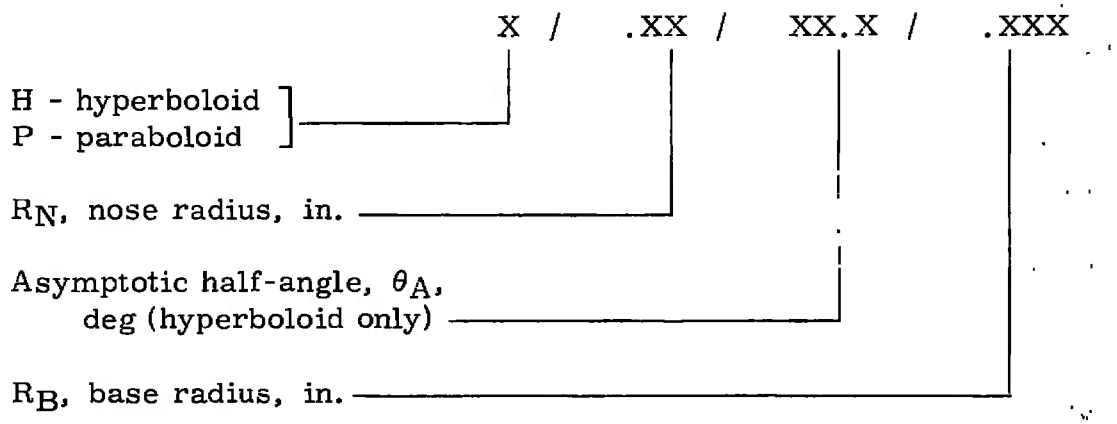

The variations in geometry used were, for the hyperboloid: three asymptotic half-angles, θ_A = 10, 22.5, 45 deg; nose radii from 0.05 to 0.25 in.; and base radii from 0.100 to 0.300 in. For the paraboloid, nose radii were 0.100, 0.150, 0.200, and 0.250 in., with base radii varying from 0.100 to 0.300 in.

Machining of the forebodies required the use of templates for producing the body contours. Optical comparator verification of the model coordinates revealed deviations of less than ±0.0002 in. from the desired shapes.

2.2.1 Drag Models

About eighty of the one hundred models tested were drag models. The basic construction was the same in all cases: The forebody was machined from solid stainless steel, followed by a flat base from which there protruded a small mounting stub (see Fig. 4). The mounting stub was necessary because the models were not long enough to contain the balance sting. To reduce tare loads, a sting shield was added, extending from the balance shield to within 0.030 in. of the model base. The test arrangement is illustrated in Fig. 5.

Families of drag models were used to obtain drag distributions over several test bodies. In a family, models had the same nose radius and asymptotic angles but different lengths. One such family, H/.05/10/.100 .300, is shown in Fig. 6.

2.2.2 Pressure Models

The pressure models were of two types: (1) two large hyperboloids, used in Tunnel C to obtain pressure distributions at near-inviscid conditions, and (2) seven small hyperboloid and paraboloid models, used in

Tunnels C and L to obtain pressures for correlation with drag family measurements.

The large models, shown in Fig. 7, had 6-in. base diameters and 0.500-in. nose radii. Each model had 20 pressure taps located in opposing-rays on the surface. Measurements of surface temperatures were made with Chromel®-Alumel® thermocouples welded to the inside model wall in a slot where the wall thickness was 0.060 in.

The small models were designed for operation in both Tunnels C and L; therefore, 0.600 in. was the maximum base diameter. The small size also limited the number of pressure taps (four static pressure taps and a pitot pressure port); and since time for running the models was limited, a quick-change arrangement was necessary. Figure 8 illustrates the design used for the Tunnel C tests.

2.2.3 Skin Temperature Models

Since only weak influences of geometry were expected in the equilibrium skin temperatures, only three models were used, representing extremes in model geometry: (1) H/.05/10/.300, the longest, most slender model tested, (2) H/.05/45/.300, a blunt model with a small nose radius, and (3) H/.25/45/.300, the bluntest model tested. The models were Eloxed® to a wall thickness of 0.010 in. or less and the thermocouples (Chromel-Alumel) welded to the inside surfaces. Locations of the thermocouples could not be accurately determined upon installation, so X-ray photographs were taken, clearly defining the position of each thermocouple. The mounting of the skin temperature models for the Tunnel C tests is shown in Fig. 9.

2.3 INSTRUMENTATION

Instrumentation for the force tests was common to both Tunnels C and L. The force balance, which has been used by several investigators (Refs. 9 and 10), was a one-component, low-load device using a Shaevitz transformer as the sensing element. In Tunnel L, data readout was on a voltmeter displaying the output from a 20-kHz carrier amplifier. For the Tunnel C tests, the amplifier output was simultaneously delivered to a voltmeter and to the tunnel data system.

Pressure data for the Tunnel L tests were read on a voltmeter as in the force tests. In Tunnel C, the data were obtained through the standard tunnel data system. Skin temperature data were obtained by direct reading of the thermocouple output in Tunnel L; while in Tunnel C, the standard data reduction methods were used.

SECTION III
DESCRIPTION OF PROCEDURES

3.1 TEST CONDITIONS

For the Tunnel C portion of testing, recent pitot pressure surveys provided current calibration data for determining test conditions. As part of the standard tunnel operation, a pitot probe was inserted into the flow at intervals to make possible corrections in Mach number necessitated by changes in the humidity of the test air. Calculations of the Tunnel C test conditions involved accounting for real-gas effects.

The Tunnel L test conditions were obtained from pitot pressure surveys run concurrently with the present data tests. The method of determining flow conditions was as described by Lewis and Arney (Ref. 11) and Potter, et al. (Ref. 8).

Calculation of flow conditions for Tunnels L and C is consistent insofar as thermodynamic properties are concerned; however, viscosities are ordinarily calculated from different sources. To make the present data consistent, compatible viscosity laws have been used for air and nitrogen (Fig. 10). The viscosity data are taken from Hilsenrath, et al. (Ref. 11) and Yos (Ref. 12). Below 100°K a straight line extrapolation from the Hilsenrath data to zero is used. A complete listing of flow conditions is presented in Appendix II.

3.2 PROCEDURE

Procedures in the drag tests required some care in order to obtain good data. The force balance was temperature-sensitive and would drift during heating and cooling. It was determined, however, that, by taking several drag points at close time intervals, one could obtain an equilibrium condition on balance heating. The data obtained in this manner are exemplified by the drag points in Fig. 11a. Note that the drag increases steadily for several points and then reaches a level about which additional points are scattered. In general, the procedure was to discard the first three points and average the remaining points. Up to a total of ten points was taken in order to obtain one drag reading. The usual scatter about the final average was ±1 percent.

Model alignment was the chief concern in the pressure distribution tests. In Tunnel C, any effects of misalignment were easily resolved. On each model, data points were taken with the model at 0- and 180-deg

roll angles. The resulting data were averaged to obtain a final result. In Tunnel L, however, the model position was fixed during a tunnel run. To verify measurements, the models were installed and run two times at each condition. In Fig. 11b, examples of the data obtained are shown; note that scatter in the Tunnel L data is considerably larger than for the Tunnel C results. Later in Section III, corrections to the Tunnel L data will be discussed. It should be noted that, because of the low pressures in Tunnel L, as much as 1 hr was required to reach equilibrium conditions at the transducer.

Shock-layer pitot pressure surveys were conducted at two locations on each of the large hyperboloid models. For the 10-deg hyperboloid, surveys were normal to the model surface — a convenient direction for comparison with boundary-layer analyses. The 45-deg hyperboloid wall, however, was too steep to permit surface normal traverses; therefore, all data were taken on lines normal to the model centerline. For both models, the pitot tube alignment was approximately at 2-deg incidence to the model surface. Previous experience indicates that the resulting incidence to the model flow field total velocity is imperceptible in a pitot pressure measurement.

The skin temperature data were obtained with the models at near-steady-state conditions. To determine the time at which suitable temperature levels were reached, the most rearward thermocouple was monitored until a change of less than 1 percent occurred in a 3-min period. In Tunnel C, the models reached 90 percent of steady-state surface temperature in less than 1 min, and in Tunnel L the time was about 2 min.

3.3 PRECISION

The precision of any experimental data must be considered as a function not only of the direct measurements but also the flow conditions. The estimated uncertainties of the data are as follows:

	Uncertainty, percent	
	C_D	p_w/p_o'
Tunnel C	±7	±1
Tunnel L	±7	±5

The figure of ±5 percent for pressure measurements in Tunnel L refers only to the uncorrected data. Corrections for thermal transpiration and orifice heat transfer, discussed below, were as high as +50 percent. No precision has been assigned the corrected data.

3.4 CORRECTIONS TO EXPERIMENTAL DATA

3.4.1 Drag

In any test facility, small day-to-day variations in calculated flow conditions may occur because of simple experimental uncertainty and variations in test gas humidity and ambient temperature. In the present tests, the important result of these was a general uncertainty in the value of local test section impact pressure, p_0' (and hence dynamic pressure, q_∞).

The drag tests could not be coupled directly with pitot pressure measurements because of equipment installation limitations, so a "reference drag body" to monitor changes in dynamic pressure was used. A flat-face disk was chosen because it was thought to have a nearly constant drag coefficient over the range of conditions of the present tests.

To assure the validity of the disk in the role of dynamic pressure monitor, a series of drag measurements was made in conjunction with pitot pressure measurements. In order to cover the Reynolds number range, four models were used, with diameters of 0.200, 0.400, 0.500, and 0.600 in. (The 0.600-in. disk was used as the reference body.) The results of this investigation are shown in Fig. 12 where the drag coefficient is seen to be nearly constant from near-inviscid conditions to a lower Reynolds number of 170, based on model diameter. The lowest Reynolds number data shown were at first thought to be in error; however, repeated measurements verified its level. The first-collision drag curve of Miller (Ref. 14) is shown to indicate the predicted point of drag increase at low Reynolds numbers.

The disk data were used in the following manner: The disk drag was measured several times during each operating shift, and for a given model the drag coefficient was calculated by

$$C_D \text{ (model)} = \frac{D_1}{D_2}(1.72)$$

where

D_1 = measured drag on the model

D_2 = measured drag on the disk

and

1.72 = expected value of disk drag coefficient

The correction, in most cases, served to bring repeat data within ±2 percent, which was much better than the estimated uncertainty of the drag coefficients (±7 percent). Figure 13 illustrates the effect of the correction.

In any sting-mounted drag test, two factors must be taken into account: base drag and tare loads. If the base pressure is equal to the free-stream pressure, no correction is required. No base pressure measurements were made during the present tests; however, measurements using the present balance and similar models indicate that base drag corrections would be no more than plus one-half of 1 percent in Tunnel L. Under Tunnel C conditions, one would expect base- to free-stream pressure ratios of about 0.5 (Ref. 15) which would result in a maximum drag correction of -1.5 percent (for H/.05/10/.300). Tare loads (forces on the balance with the model independently supported near to, but not touching, the sting) were measured for one of the smaller models (R_B = 0.100) and found to be negligible.

3.4.2 Pressure

The uncertainties in pitot pressures did not affect the pressure tests because each model was equipped with a pitot pressure port, which read the impact pressure directly (subject to corrections discussed below for Tunnel L). Each normalized pressure was thus based on an immediate, local value of the impact pressure. One problem which might have occurred in very low density flow is a decrease in observed pitot pressure when the probe size is very small. Based on the work of Potter and Bailey (Ref. 16) in Tunnel L, the present models were large enough to avoid the region of pressure decrease.

In Tunnel C, no further corrections to the pressure data were required; however, the very low pressures in Tunnel L required corrections of thermomolecular pressure effects after the method of Kinslow and Arney (Ref. 17). Before the correction is described, a brief discussion will be directed to the choice of hot-wall models for the present tests.

The two possibilities for pressure models were (1) internally water-cooled models in which the temperature is constant from the orifice (model surface) to the sensing transducer and (2) uncooled models, for which there is a temperature gradient from the model surface (at some steady state temperature dependent on tunnel flow conditions) to the water-cooled transducer. In order to effect corrections, the water-cooled model required specification of the heat-transfer rate at the model surface, while the uncooled models required only the steady-state

surface temperature. From the standpoint of correlation of the pressure data with the drag data, neither case is correct because the drag models probably did not reach steady-state temperatures in the course of obtaining drag points; however, the surface temperatures are well above cooling-water temperatures.

In the corrections, temperature is by far the easier wall condition to specify because of its relative insensitivity to model geometry and ease of measurement. Also, any surface heat transfer to a cold-wall model would have to be determined by some theoretical means, which would compromise the experimental nature of the data. (At the time of the present tests, it was not feasible to obtain experimental heat-transfer rate data on the small models in Tunnel L.) The obvious choice for model type was, therefore, the uncooled, hot-wall models.

The basic correction to the hot-wall data was for thermal transpiration; that is, a correction to account for the pressure gradient induced by the temperature gradient in the pressure tube. From Kinslow and Arney (Ref. 17), the semiempirical equation describing the transpiration phenomenon may be written as

$$\sqrt{\frac{(1 - T_1/T_2)^{1/2}}{(1 - P_1/P_2)^{1/2}}} = 1.0 + 0.275\,(Kn)^{-1}\,(T_1/T_2)^{2/3} + \frac{0.625\,(Kn)^{-1}\,(T_1/T_2)^{2/3}}{1.0 + 24.0\,[(Kn)^{-1}\,(T_1/T_2)^{2/3}]^2} \qquad (3)$$

where 1 refers to conditions at the model surface and 2 refers to conditions at the transducer. The experimental data from which Eq. (3) was derived were in the range

$$0.5 \leq T_1/T_2 \leq 2.0$$

a fact which strains the applicability in the present case, where T_1/T_2 was as low as 0.2. The difficulty was overcome by applying the correction sequentially over a number of temperature ranges, each within the region of validity. It was discovered that successively smaller steps in temperature made slight changes in the correction. The results of the above exercise are shown in Fig. 14.

Though the model testing was done at equilibrium temperatures, it was not accomplished with zero heat-transfer rate, there being considerable radiative transfer to the cold tunnel walls (T_∞ = 300°K). The radiative transfer was, of course, balanced by a convective transfer to the model wall, which dictated a further correction to the pressure data.

Since the conductive heat-transfer rate along the model surface was quite small, it was assumed that the radiative and convective rates were in balance.

The radiative transfer was determined by assuming that the shape factor for concentric spheres applied and that the model surface was at the average of the temperatures measured. The model emissivity was taken to be 0.70 (Ref. 18). Values of the resulting radiative flux were quite small. Corrections for heat-transfer effects on pressure may be determined from Eq. (48) of Kinslow and Arney. It is a sixth-degree polynomial for which parametric graphical solutions have been plotted.

The results of the corrections are illustrated in Fig. 15. Note that the application of small temperature gradients to the thermal transpiration equation results in a correction which is equal and opposite to that effected by the radiative flux. The maximum correction encountered was about +50 percent, at the lowest Reynolds number.

3.5 NUMERICAL DATA REDUCTION

Correlation of the experimental drag and pressure data was achieved by use of a short computer program. The chief calculations of the program were as follows:

1. Compute Newtonian impact theory pressure distributions and integrate to obtain drag.
2. Curve-fit the experimental pressure data and integrate for pressure drag.
3. Curve-fit the measured total drag distributions.
4. Using the difference between the total drag and the pressure drag for skin friction drag, numerically differentiate to obtain local skin friction coefficient.

The first function of the program was to compute body coordinates. For the axial and radial components, nondimensionalized (by nose radius, R_N) coordinates (nondimensionalized distances are denoted by an asterisk) are

$$Z^* = -a^2/b^2 + \sqrt{a^2/b^2\,(a^2/b^2 + r^{*2})} \quad \text{(hyperboloid)} \tag{4}$$

and

$$Z^* = r^{*2}/2 \quad \text{(paraboloid)} \tag{5}$$

Surface distances (Ref. 19) on the hyperboloid are given in differential form,

$$dS^* = \sqrt{\frac{(1 - a^2/b^2)r^{*2} + a^2/b^2}{a^2/b^2 + r^{*2}}}\, dr^* \qquad \text{(hyperboloid)} \qquad (6)$$

which was numerically integrated. For the paraboloid, surface distances were computed from

$$S^* = \frac{r^*}{2}\sqrt{r^{*2} + 1} + \frac{1}{2}\ln\left(\sqrt{1 + r^{*2}} + r^*\right) \qquad \text{(paraboloid)} \qquad (7)$$

Modified Newtonian impact theory was used to estimate inviscid pressure distributions (see Section IV). The normalized Newtonian distribution is given by

$$(p_w\, p_o')_N = \sin^2\theta_w\,(1 + p_\infty\, p_o') + p_\infty\, p_o' \qquad (8)^1$$

where $\sin\theta_w = dr/ds$. The Newtonian pressure drag is then

$$C_{D_N} = \int_0^{S^*}\left[(p_w\, p_o')_N - p_\infty\, p_o'\right]\frac{2r^*\sin\theta_w}{(q_\infty/p_o')\,R_B^{*2}} \qquad (9)$$

The experimental data did not include enough points to allow any direct numerical manipulations upon them; thus, all data were curve-fitted by using the method of least squares. The pressure data proved to be the more difficult to fit suitably, since there were only five points per case. Polynomials up to sixth degree were attempted, but the results were unsatisfactory. Therefore, the very simple relationship

$$(p_w/p_o')_{EXP} = \sin^d\theta_w \qquad (10)$$

was used. The sine function was chosen because the inviscid pressures were given by $\sin^2\theta_w$ (neglecting p_∞), making it reasonable to assume that the viscous-interacting pressures for a moderate-length body could be represented by the sine to some power less than two. The trigonometric function would not be adequate for a very long hyperboloid, because the viscous and inviscid representations would remain a fixed distance apart as the asymptotic angle was approached, whereas one

---

[1]In all cases involving Newtonian theory, ratios of free-stream and after shock conditions are taken for a perfect gas at Mach number 10. Experimental data make use of actual tunnel conditions.

would expect the viscous induced pressure to approach the inviscid pressure for a very long body (Ref. 4). For the present relatively short bodies, however, the power function seems to be adequate. Having the curve-fitted data, one could then obtain the total pressure drag by integrating

$$C_{D_p} = \int_0^{S^*} [(p_w/p_o')_{EXP} - p_\infty/p_o'] \frac{2r^* \sin \theta_w}{(q_\infty/p_o')R_B^{*2}} dS^* \tag{11}$$

Each series of drag bodies was comprised of nine models, giving very good distributions upon which to base curve-fits. Two types of curves were used. For the hyperboloid

$$C_{D_T} = k_1 (R_w^*)^{k_2} \tag{12}$$

was sufficient for all cases. The paraboloid data, having an inflection in the distribution, required a polynomial. Though polynomials up to degree six were tested, the third-degree curve was best for all paraboloid cases.

Having the measured surface quantities as functions of body locations, one could then proceed to calculate components of pressure and drag. The friction-drag component was simply defined as

$$C_{D_f} = C_{D_T} - C_{D_p} \tag{13}$$

and from the friction drag coefficient the local skin friction was derived. Rather than attempt to curve-fit the friction drag and differentiate to obtain the skin friction, a very simple numerical derivative was used

$$C_f = \frac{\Delta C_{D_f} \pi R_B^{*2}}{\Delta A \cos \theta_w} \tag{14}$$

where the delta (Δ) quantities are the differences in the given parameters (C_{D_f} and A) between adjacent stations, dictated by step size in r*. The procedure was not entirely successful, for though the resulting distributions in skin friction were smooth, near the 0.25-in. nose radius bodies, the pressure drag exceeded the total drag (both curve-fitted), yielding a negative skin friction. Explanations for some of this behavior are given later in Section V.

SECTION IV
SOME THEORETICAL CONSIDERATIONS

4.1 INVISCID PRESSURE DISTRIBUTIONS

On any blunted body in inviscid supersonic flow, there exists the possibility of two flow regimes: (1) a region of subsonic flow near the stagnation point and (2) supersonic flow over the downstream portion of the body. For such bodies, the surface pressures may be quite reliably predicted by a number of numerical techniques. One widely used approach is that of Inouye, Rakich, and Lomax (Ref. 20), from which the present solutions were obtained. Their solutions are obtained from an inverse method for the subsonic flow and the method of characteristics for the supersonic flow. The results are presented only in tabular form; that is, the solutions cannot be expressed analytically. For the present models, however, an analytical pressure distribution was readily available. Results from the modified Newtonian impact theory (Eq. 8) compare favorably with results from the more complicated method of characteristics. Figure 16 illustrates the comparison of the two results. Note that there is no characteristics solution shown for the 45-deg half-angle hyperboloid. The solution was attempted; however, the computer program failed to complete the blunt-body solution. A further discussion of this particular case is included in Section V.

4.2 VISCOUS INTERACTIONS

Ferri and Libby (Ref. 21) first noted that there is an interaction between the boundary layer and the outer inviscid flow field on a blunt body. They termed the influence vorticity interaction, deriving their results from the entropy gradient produced by a curved shock. Since that time a number of authors, notably Hayes and Probstein (Ref. 22) and Ferri, Zakkay, and Ting (Ref. 23) have derived terms defining the so-called vorticity interaction. Van Dyke (Ref. 3) was the first to adequately define the interaction by including shock-induced vorticity among seven second-order boundary-layer effects. Davis and Flügge-Lotz (Ref. 2), following the theory of van Dyke and using a finite-difference scheme developed by Flügge-Lotz and Blottner (Ref. 24), presented solutions for the stagnation regions of blunt bodies. The approach was further refined, and solutions for downstream regions were published by Lewis (Ref. 4) and Adams (Ref. 5). Davis (Ref. 6) extended the approach to the fully viscous shock-layer problem.

In the numerical approaches mentioned above, one has the choice of several theoretical models, depending primarily on the degree of rarefaction of the flow under consideration. Each of the theories has a restricted range of applicability. Numerous authors have attempted to define the various flow regimes which may occur, and the parameters used differ widely. Figure 17 is a depiction of the regimes as defined in the classic paper by Probstein and Kemp (Ref. 25). Also shown are several other parameters which have been used to predict the growth of viscous effects. No one of these could be expected to be all-inclusive; however, each has some merit. The $\bar{v}_\infty$ and $\bar{v}^*$ include the wall temperature as a variable and have been used successfully to predict drag, $\bar{v}_\infty$ (Ref. 26), and heat-transfer, $\bar{v}^*$ (Ref. 27), behavior. The van Dyke expansion parameter, ϵ, appears in series form in the matching between the viscous and inviscid flow fields in second-order theory and thus is very useful in describing the growth of viscous effects in second-order boundary-layer theory. It does not, however, include the wall temperature of the model.

In the present discussion, the $\bar{v}_\infty$ parameter will be used, since wall temperatures vary widely for the data. Where comparisons with theory may be made, both $\bar{v}_\infty$ and ϵ will be specified.

SECTION V
PRESENTATION AND DISCUSSION OF EXPERIMENTAL RESULTS

The data to be presented were corrected as outlined in Section III. All data, both corrected and uncorrected, are tabulated in Appendix II.

5.1 HIGH REYNOLDS NUMBER DATA

The high Reynolds number data were obtained primarily to make comparisons with inviscid pressure distributions. Figure 18 shows the distributions obtained for the 10-deg hyperboloid. Note that the higher Reynolds number data agree quite well with the inviscid distributions except on the downstream portion of the body where viscous interaction effects may be significant.

In Fig. 19, data for the 45-deg hyperboloid are shown. In contrast to Fig. 18, there is definite disagreement between the data and the Newtonian distribution.

Note that the pressure ratio is everywhere above that required to produce sonic flow on the body ($p_w/p_o' = 0.5283$). This may explain the failure of the numerical solution mentioned in Section IV where, in order to complete a solution, a sonic line must be established in the body shock layer.

The skin temperature data obtained on the large hyperboloids are shown in Fig. 20. Note that the blunter model (Fig. 20a) has a stagnation point temperature which is 4 percent higher than that of the 10-deg hyperboloid. The model geometry, however, does not influence the gradient in temperature along the model surface.

The shock-layer pitot survey data were obtained to show the effect of shock-induced vorticity on a measured flow field quantity. From them one may gain some insight into the extent of vorticity effects on the boundary layer.

Figure 21 shows the surveys obtained on the 10-deg hyperboloid. As mentioned above in Section III, the traverse is normal to the model surface. Note that, for both stations surveyed, the inviscid portion of the shock layer has a nearly linear variation of pitot pressure which, by its slope, indicates a strong entropy gradient.

The 45-deg hyperboloid results are presented in Fig. 22, where the surveys are normal to the model centerline. The flow field character is quite different from the 10-deg body at both survey stations. At $S/R_N = 1.87$ (Fig. 22a), there is a short region of strong pressure gradient which decreases rapidly near the shock. Farther downstream at $S/R_N = 6.54$ (Fig. 22b), the shock layer is at a constant pitot pressure from $Y/R_N = 0.5$ to the shock.

From the pitot survey results, one would expect that the effects of shock-induced vorticity on the 45-deg hyperboloid would decrease quite rapidly as the body length is increased. In contrast, the 10-deg hyperboloid shows no evidence of the entropy gradient weakening as far downstream as $S/R_N = 12$. The same deduction may be derived from examination of the body slopes; i. e., the 45-deg hyperboloid goes quite rapidly to the asymptotic half-angle ($\theta_w - \theta_A = 0.5$ deg at $S/R_N = 7.0$), whereas the 10-deg hyperboloid has a local slope of 13.7 deg at $S/R_N = 16.0$.

5.2 LOW REYNOLDS NUMBER DATA

5.2.1 Skin Temperature

The skin temperature data obtained on the small models are summarized in Fig. 23. As expected, the effects of model geometry on temperatures are not large. There is, however, a geometry influence from which temperatures for the bodies not tested may be inferred. Figure 24 illustrates the variation of model stagnation point wall temperature with Reynolds number and stagnation temperatures, T_o. Note that there is a consistent trend of the temperatures which is attributed to the body length, Reynolds number, and tunnel stagnation temperature (controlling the radiative flux to the tunnel wall). From the data shown, one may select the appropriate stagnation point temperature; the body temperature distribution may be obtained simply by using the same slopes shown in Fig. 23.

5.2.2 Pressure

The use of the small pressure models resulted in data at conditions where significant viscous interaction was present, even in Tunnel C. Figure 25 presents pressure distributions obtained on the seven models along with the curve fit used in the data reduction program.

In general, the pressure ratio, p_w/p_o', increases with decreasing Reynolds number for the small-nose models (Figs. 25a through d). An exception is the lowest Reynolds number data (Re_{∞, R_N} = 22 and 44), which are consistently lower than data at the next highest Reynolds number -- a decrease contrary to all expectations. The 45-deg hyperboloid (H/.05/45/.300) data disagree with the inviscid distribution in a manner similar to that observed on the large models (Fig. 19).

The 0.25-in. nose radius models (Fig. 25e, f, and g) showed only small influences of viscous interaction, as might be expected. The two hyperboloids have subsonic flows over their entire lengths, while the paraboloid sonic point occurs on the body for all conditions. Note that the 45-deg hyperboloid disagrees with the inviscid distribution just as was seen on the longer models.

The curve-fit data provide an interesting comparison between the various bodies, since the pressure distributions may be represented by the power d to which $\sin \theta_w$ is taken. Figure 26 illustrates the comparison among the bodies having natural sonic points. There is a definite trend established in these data shown, which produces scatter in the resulting pressure of only ±15 percent when the wall angle is

15 deg. The scatter decreases at higher body angles, where most of the data were taken.

5.2.3 Drag

The drag distributions obtained on the seven test bodies are presented in Figs. 27 through 33. Also shown are the integrated inviscid and total pressure drag and the skin friction drag. Note that in some cases the friction drag attains a positive value at some distance from the model nose; generally, in these cases, the pressure drag was very slightly larger than the total measured drag. This fact may be a failure of the curve-fits to represent the drag or pressure distributions, or it may be an indication of inaccuracy of the experimental data.

One characteristic of the blunt-body data should be noted at this point: In nearly every case for the 0.25-in. nose radius bodies, the integrated pressure drag is higher than the measured total drag except near the model base. This may be because the very blunt bodies did not have a "natural" sonic point; that is, the pressure on the body was everywhere above the ratio $p_w/p_o' = 0.5283$. In such cases, sonic flow must be established by a sudden expansion near the model base, which in turn tends to decrease the pressure just ahead of the base. The data of Boison and Curtiss (Ref. 28) demonstrate this effect for several spherical segments. The result of the sonic flow being established at the base is that each drag model of a family would have a lower drag than the pressure distribution from the test body would predict at the same point. Thus, the drag distribution is meaningless for all models not having natural sonic points.

A summary of the drag data would be desirable at this point; however, the wide range of conditions (Reynolds number, wall temperature) and geometries make such a display somewhat cumbersome. Figure 34 shows many of the variations in drag which occurred with changes in the viscous interaction parameter, $\bar{v}_\infty$. (Note that the drag coefficient is referenced to the local base area, rather than the area for a 0.300-in. radius, as was the case with the drag distributions.) In general, for each geometry considered separately, there is an increase with $\bar{v}_\infty$.

A simple example of the effect of Reynolds number on pressure distributions was shown in Fig. 26, where deviation from the Newtonian distribution served as a basis. A similar demonstration for the drag data was obtained from observation of the Newtonian drag, which is strongly dependent on a bluntness ratio, L/R_B, presented in Fig. 35a. Combination of the experimental data of Fig. 34 with the Newtonian drag

curve results in an assessment of viscous interaction effects represented by $\bar{v}_\infty$ (Fig. 35b). The data shown are for both the slender bodies and the blunt bodies where the sonic point was at the model base.

5.2.4 Skin Friction

One aim of the drag distribution efforts was to obtain local skin friction. The method of calculation, described in Section III, did not restrict the skin friction in regard to form, since only a simple numerical difference was used. Mention was made in Section III of difficulty encountered in calculating values for some cases; that difficulty may be attributed directly to the high pressures on the very blunt bodies. Near the stagnation point of some of the more slender bodies, the pressure drag exceeded total drag, resulting in negative values for skin friction.

The small-nose radius, 45-deg hyperboloid (H/.05/.45/.300) serves as a good example for the behavior of the blunt-body skin friction results. The data, shown in Fig. 36a, are quite erratic, showing no particular trend with body location or the test conditions. Obviously such results do not fulfill the objectives of the study; no further data on the blunt bodies will be considered.

For the more slender, small-nose radius models, the skin friction calculation was quite successful. Figures 36b, c, and d (H/.05/10/.300, H/.05/2.25/.300, and P/.10/.300, respectively) show the data obtained. Note that no data appear near the stagnation point. Though for some cases the skin friction appeared to be reasonable over the entire body, no actual drag or pressure data were available for the stagnation regions, making any derived results highly speculative. At the lowest Reynolds number, the friction coefficient is quite high compared to the higher Reynolds number results. Recalling the pressure data, one may conclude that the low Reynolds number friction data are unrealistic.

The remaining distributions comprise the total of the skin friction data. There are reasonable, consistent trends on all three bodies. On the paraboloid (Fig. 36d) a peak is seen near $S/R_N = 1.5$. This peak would be expected on all bodies somewhere in the nose region.

5.3 COMPARISON WITH THEORY

The stated purpose of this investigation was to provide experimental data of sufficient scope to allow comparisons with theory. Two main sources of viscous-flow calculations will be used: the second-order

boundary-layer results of Adams (Ref. 5) and Davis' fully viscous shock-layer approach (Ref. 6). While other published theoretical results may be applicable to the geometries and conditions of the present study, none on the particular bodies are known to the author.

Recalling the disagreement of the pressure distribution on the 45-deg hyperboloid with the Newtonian pressure distribution, one might speculate whether only those analytic bodies lacking natural sonic points would have experimental distributions different from Newtonian results. Some results (Ref. 29) on ellipsoids are presented in Fig. 37 along with the present high Reynolds number data. Note that the bluntness of the ellipsoid does have an effect on the pressure distribution; the blunter the body, the lower is the pressure when compared with Newtonian. The data of Boison and Curtiss (Ref. 28) indicate that spherical segments without natural sonic points have experimental pressures which are below Newtonian results. The 45-deg hyperboloid data, being higher than the Newtonian predictions, are thus unsupported by experimental data on other blunt bodies.

Comparison of the small-model data with the numerical results of Adams (Refs. 5 and 30) and Davis (Ref. 6) is presented in Figs. 38a through c. Because the theoretical results are not at the specific conditions of the present tests, the data are shown as functions of $\bar{v}_\infty$. Pressure distributions (Fig. 38a) reveal that pressures are fairly well represented by the second-order theory or viscous shock-layer theory; both methods use Newtonian impact theory to calculate the pressure distributions on the displaced (by viscous interaction effects) body. Note that the very low Reynolds number pressure and skin friction data are omitted from Fig. 38 since the pressure data appear to be incorrect. One of the second-order cases shown was prepared especially for comparison in this work; it will be discussed further, later in this section.

The growth of skin friction is shown in Fig. 38b. For the 10-deg hyperboloid the comparison with second-order theory is excellent, even at very low Reynolds numbers where the results would not be expected to be valid. One suspects the agreement to be fortuitous, however, when the results from the 22.5-deg hyperboloid and the paraboloid are observed. Note that the influence of wall temperature predicted by the second-order theory is only slight. The fully viscous shock-layer results of Davis (Ref. 6) show good agreement for the 22.5-deg hyperboloid; the particular case shown is within the expected range of validity.

Drag data (Fig. 38c) appear in much the same fashion as the pressure and skin friction. The theory points are restricted to second-order results only, since Davis did not present gross effects, such as drag

components. Note the excellent agreement of the Adams case calculated for the conditions of the present test.

The expected range of validity for the second-order theory is for values of the van Dyke expansion parameter, ϵ, less than 0.13 for the present length 10-deg hyperboloid (Ref. 30). The highest Reynolds number of the drag distribution tests corresponds roughly to the above value of ϵ. A calculation performed particularly for comparison at this condition is shown in Fig. 39. The pressure level (Fig. 39a) is slightly overpredicted by the theory (+10 percent) in the body region where the experimental data were obtained, whereas the curve fit of the experimental data rises to slightly more than the theory prediction near the model stagnation region.

Skin friction results are shown in Fig. 39b. The agreement is good downstream on the body; however, at about $S/R_N = 3$, the experimental skin friction suddenly decreases and falls below the theory curve. This may be attributed to the curve-fit problem near the model nose, where the pressure drag exceeds the total measured drag.

The growth of drag components along the body is shown in Fig. 39c, where the effects of the local distributions are clearly seen. The pressure drag is slightly higher than the theory predicts, in contradiction with the pressure distribution results. The disparity is caused by the difference between the real and perfect gas ratios, q_∞/p'_0. The theoretical and experimental skin friction components are in disagreement, again a result of the stagnation region problems.

The total drag gives a more positive comparison between theory and experiment, since the drag is directly measured. The agreement is excellent, particularly for the downstream portions of the body.

SECTION VI
CONCLUSION

An experimental investigation of several analytic bodies of revolution in hypersonic flow has been conducted; conditions on the bodies were as completely defined as was possible. In addition to the usual pressure, temperature, and drag data, a method of obtaining local skin friction indirectly has been presented. The skin friction data were successfully obtained subject to the following limitations:

1. The models must have natural sonic points.
2. In the absence of well-defined pressure distributions and drag data near the stagnation point, only the downstream portions of the body may have reasonable results.

Improvements to the data might be obtained by use of a skirt downstream of the actual drag body, simulating a continuation of the geometry. This method might also be used to perform tests on bodies which are too short to have natural sonic points.

High Reynolds number data indicate that, for continuous analytic bodies having natural sonic points, the modified Newtonian impact theory adequately predicts pressure distributions. The spherical segment data of Boison and Curtiss (Ref. 28) show that when the sonic point is at the model base, experimental data fall below the Newtonian results; their findings are in contrast to the present 45-deg hyperboloid data, which lie above the impact theory predictions.

Increases in pressure because of viscous interaction may be fairly well represented by a deviation from the Newtonian theory sine function exponent for slender bodies. Very blunt body viscous interaction, even those bodies for which the Newtonian theory is adequate, may not be represented by deviation from the exponent.

Drag data appear to be strongly dependent on the length to radius ratio of a particular body, even under conditions of viscous interaction. All inviscid data may be represented by a single drag curve, and viscous interactions appear as branches diverging from the inviscid data.

Comparisons with theory indicate that the growth of viscous interactions may be adequately predicted by a second-order boundary layer, and that, at conditions ideal to the theory, agreement with experimental data is excellent. Insufficient theoretical data were available to verify what limits might be placed on theoretical results.

The present study had several limitations which might be improved upon in similar future studies:

1. Heat-transfer rate data would certainly enhance the value of the results. Recent developments make such measurements possible.
2. The lengths of the bodies could be much greater to allow for more skin friction results.

3. For the blunted bodies of the present study, a Mach number of 10 should be sufficiently high to minimize effects of Mach number; however, data at additional Mach numbers, both higher and lower, would be beneficial.

4. As was mentioned above, the method of obtaining skin friction data on very blunt bodies might be feasible if extensions of the geometry could be simulated.

REFERENCES

1. Lewis, C. H. and Whitfield, J. D. "Theoretical and Experimental Studies of Hypersonic Viscous Effects." NATO AGARDograph 97, Part III, May 1965.

2. Davis, R. T. and Flügge-Lotz, I. "Second-Order Boundary-Layer Effects in Hypersonic Flow Past Axisymmetric Blunt Bodies." Journal of Fluid Mechanics, Vol. 20, Part 4, December 1964, pp. 593-623.

3. Van Dyke, M. "A Review and Extension of Second-Order Hypersonic Boundary-Layer Theory." Rarefied Gas Dynamics (J. A. Lauermann, Editor), Fluid Symposium Supplement 2, Vol. II, pp. 37-75, Academic Press, New York, 1963.

4. Lewis, C. H. "First- and Second-Order Boundary-Layer Effects at Hypersonic Conditions." Paper presented at the AGARD Seminar on "Numerical Methods for Viscous Flows," National Physical Laboratory, Teddington, England, September 18-21, 1967.

5. Adams, J. C., Jr. "Higher Order Boundary-Layer Effects on Analytic Bodies of Revolution." AEDC-TR-68-57 (AD667523), April 1968.

6. Davis, R. T. "The Hypersonic Fully-Viscous Shock-Layer Problem." Sandia Laboratories, SC-RR-68-840, December 1968.

7. Sivells, J. C. "Aerodynamic Design and Calibration of the VKF 50-in. Hypersonic Wind Tunnels." AEDC-TDR-62-230 (AD299774), March 1963.

8. Potter, J. L., Kinslow, M., Arney, G. D., Jr., and Bailey, A. B. "Description and Preliminary Calibration of a Low-Density Hypervelocity Wind Tunnel." AEDC-TN-61-83 (AD262466), August 1961.

9. Whitfield, J. D. and Griffith, B. J. "Viscous Effects on Zero-Lift Drag of Slender Blunt Cones." AEDC-TDR-63-35 (AD298278), March 1963.

10. Lewis, C. H., Marchand, E. O., and Little, H. R. "Mass Transfer and First-Order Boundary-Layer Effects on Sharp Cone Drag." AEDC-TR-66-37 (AD629955), March 1966.

11. Lewis, A. D. and Arney, G. D., Jr. "Vibrational Nonequilibrium with Nitrogen in Low-Density Flow." AEDC-TDR-63-31 (AD298320), March 1963.

12. Hilsenrath, Joseph, et al. Tables of Thermal Properties of Gases. National Bureau of Standards Circular 564, United States Department of Commerce, Government Printing Office, Washington, D. C., November 1, 1955.

13. Yos, J. M. "Transport Properties of Nitrogen, Hydrogen, Oxygen, and Air to 30,000°K." AVCO RAD-TM-63-7, March 1963.

14. Miller, J. T. "Calculation of Near-Free-Molecular Flux Distribution to Simple Bodies in Hypervelocity Flow." AEDC-TR-67-26 (AD649764), March 1967.

15. Zarin, N. A. "Base Pressure Measurements on Sharp and Blunt 9° Cones at Mach Numbers from 3.50 to 9.20." BRL-MR-1709, November 1965.

16. Potter, J. L. and Bailey, A. B. "Pressures in the Stagnation Regions of Blunt Bodies in the Viscous-Layer to Merged-Layer Regimes of Rarefied Flow." AEDC-TDR-63-168 (AD416004), September 1963.

17. Kinslow, M. and Arney, G. D., Jr. "Thermo-Molecular Pressure Effects in Tubes and at Orifices." NATO AGARDograph 119, August 1967.

18. Baumeister, Theodore (ed.). Mechanical Engineers' Handbook. McGraw-Hill Book Company, New York, 1958.

19. Adams, E. P. and Hippisley, R. L. Smithsonian Mathematical Formulae and Tables of Elliptic Functions. Smithsonian Institute Publication 2672. Washington: Government Printing Office, 1947.

20. Inouye, M., Rakich, J. V., and Lomax, H. "A Description of Numerical Methods and Computer Programs for Two-Dimensional and Axisymmetric Supersonic Flow Over Blunt-Nosed and Flared Bodies." NASA TN D-2970, August 1965.

21. Ferri, A. and Libby, P. A. "Note on an Interaction Between the Boundary Layer and the Inviscid Flow." Journal of the Aeronautical Sciences, Vol. 21, No. 2, February 1954, p. 130.

22. Hayes, W. D. and Probstein, R. F. Hypersonic Flow Theory. Academic Press, New York, 1959.

23. Ferri, A., Zakkay, V., and Ting, Lu. "Blunt Body Heat Transfer at Hypersonic Speed and Low Reynolds Numbers." Polytechnic Institute of Brooklyn Report 611, June 1960.

24. Flügge-Lotz, I. and Blottner, F. G. "Computation of the Compressible Laminar Boundary-Layer Flow Including Displacement-Thickness Interaction Using Finite-Difference Methods." Stanford University Report 131, January 1962.

25. Probstein, R. F. and Kemp, N. H. "Viscous Aerodynamic Characteristics in Hypersonic Rarefied Gas Flow." Journal of the Aerospace Sciences, Vol. 27, No. 3, March 1960, pp. 174-192.

26. Whitfield, J. D. and Griffith, B. J. "Hypersonic Viscous Drag Effects on Blunt Slender Cones." AIAA Journal, Vol. 2, No. 10, October 1964, pp. 1714-1722.

27. Griffith, B. J. and Lewis, C. H. "Laminar Heat Transfer to Spherically Blunted Cones at Hypersonic Conditions." AIAA Journal, Vol. 2, No. 3, March 1964, pp. 438-444.

28. Boison, J. C. and Curtiss, H. A. "An Experimental Investigation of Blunt Body Stagnation Point Velocity Gradient." American Rocket Society Journal, Vol. 29, February 1959, pp. 130-135.

29. Belotserkovskiy, O. M. "Supersonic Gas Flow Around Blunt Bodies, Theoretical and Experimental Investigations." NASA TT F-453, June 1967.

30. Adams, J. C., Jr. "Higher Order Boundary-Layer Effects for the AGARD Engineering Applications Body and Flow Conditions." Paper to be published in Proceedings of the AGARD Seminar on "Numerical Methods for Viscous Flows," Teddington, England, September 18-21, 1969.

APPENDIXES

I. ILLUSTRATIONS
II. TABLES

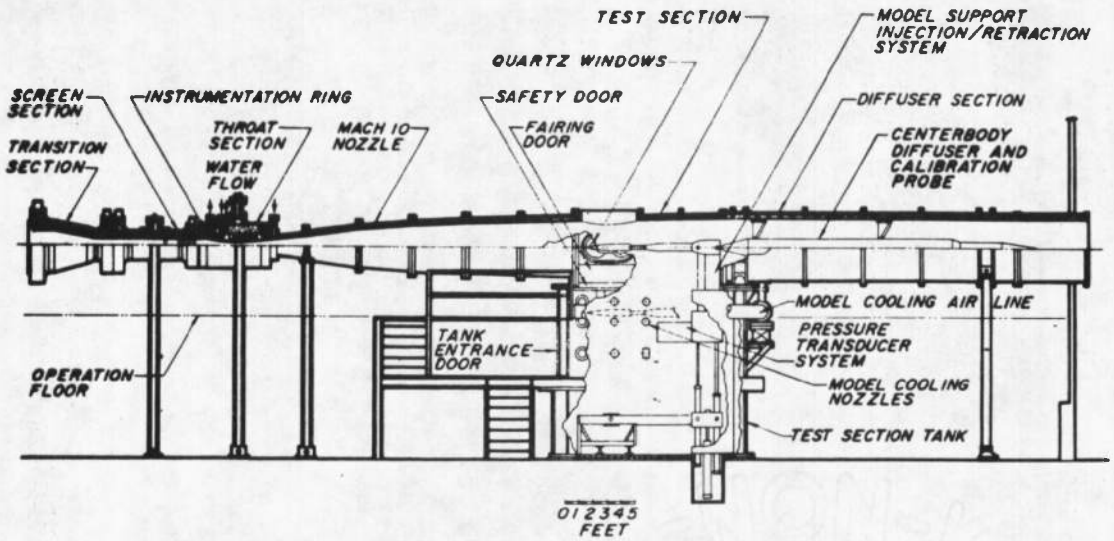

Tunnel Assembly

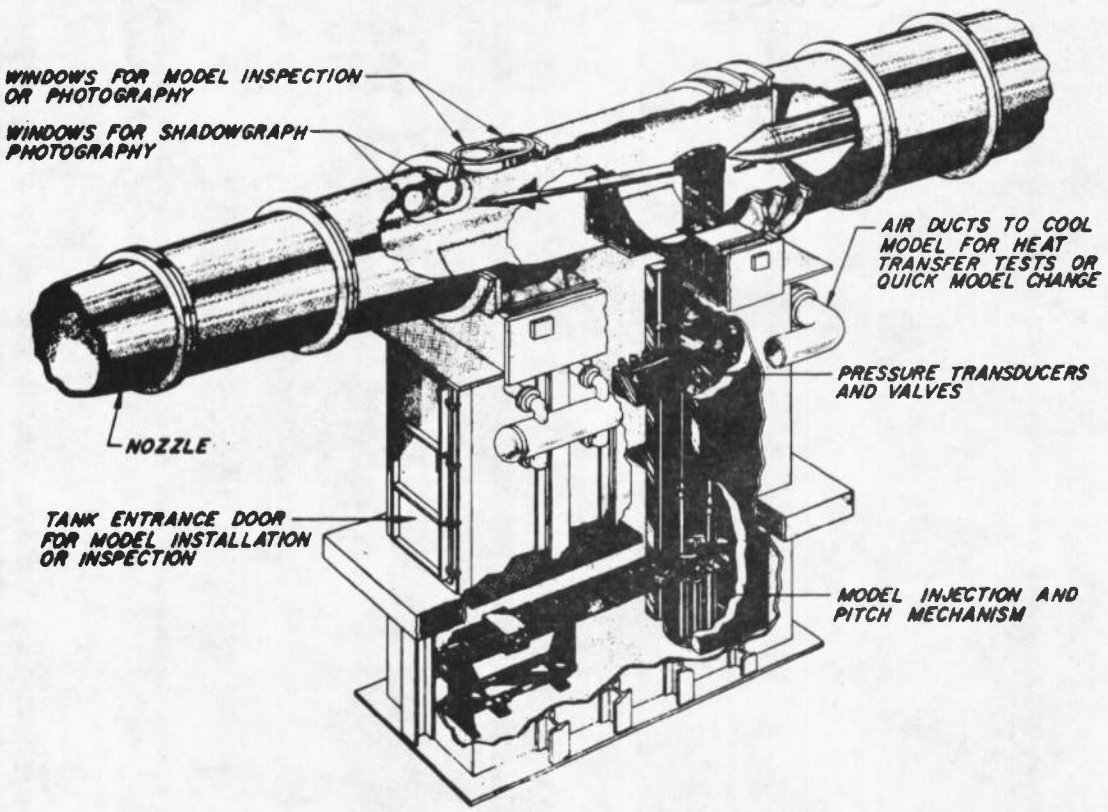

Test Section

Fig. 1 Tunnel C

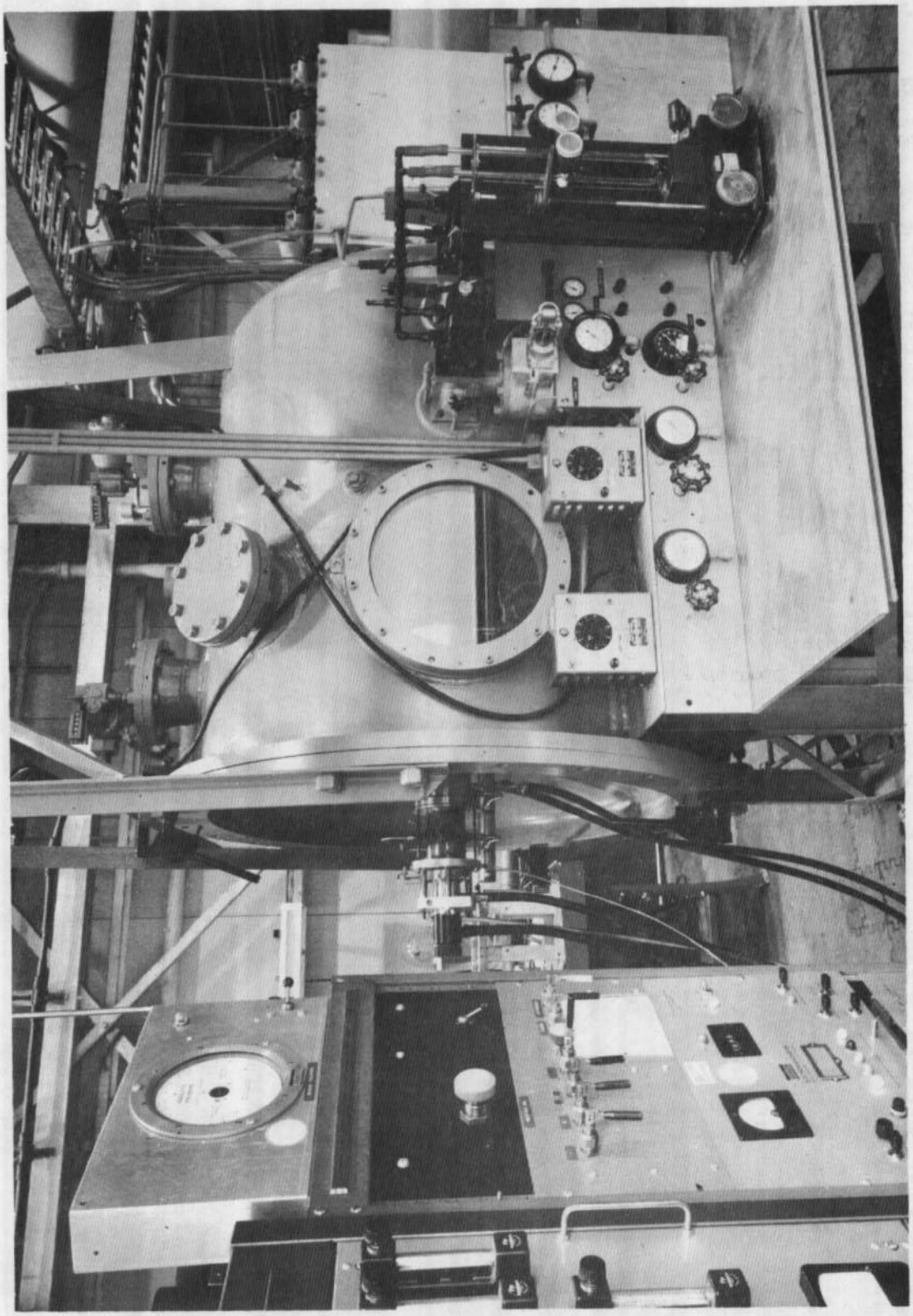

Fig. 2 Tunnel L

Coordinate Systems:

(x,y), generatrix (plane)
(r,z,ϕ), axisymetric body coordinates

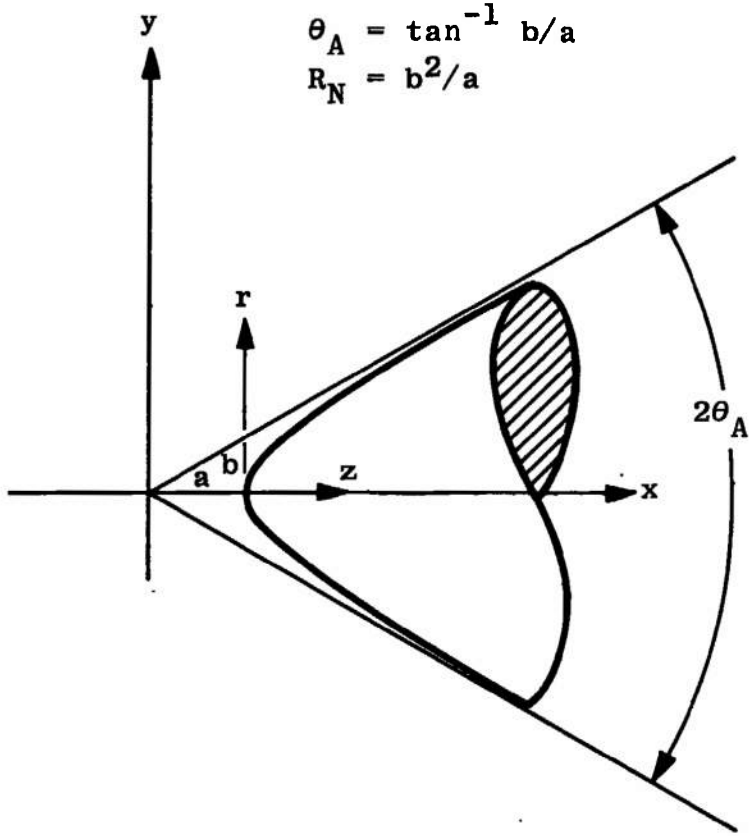

Hyperboloid

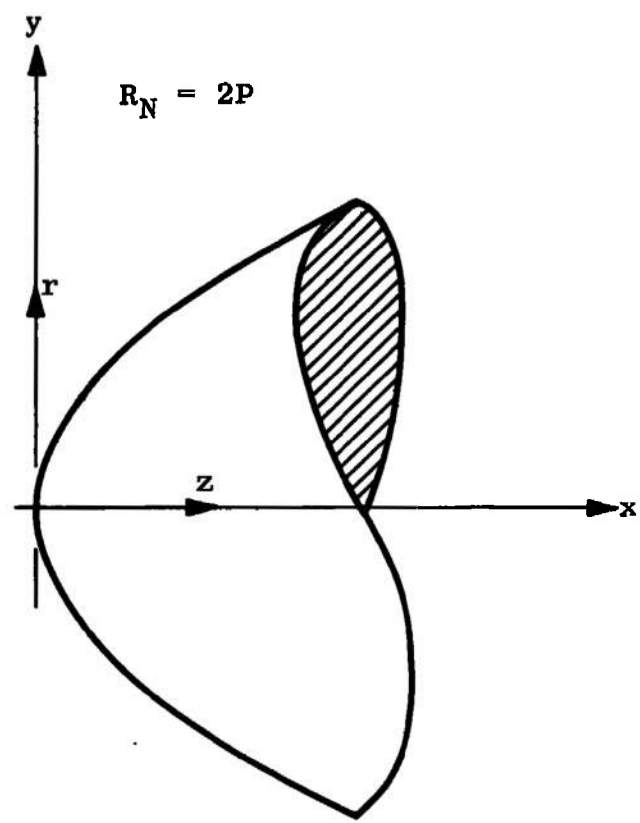

Paraboloid

Fig. 3 Geometry Details

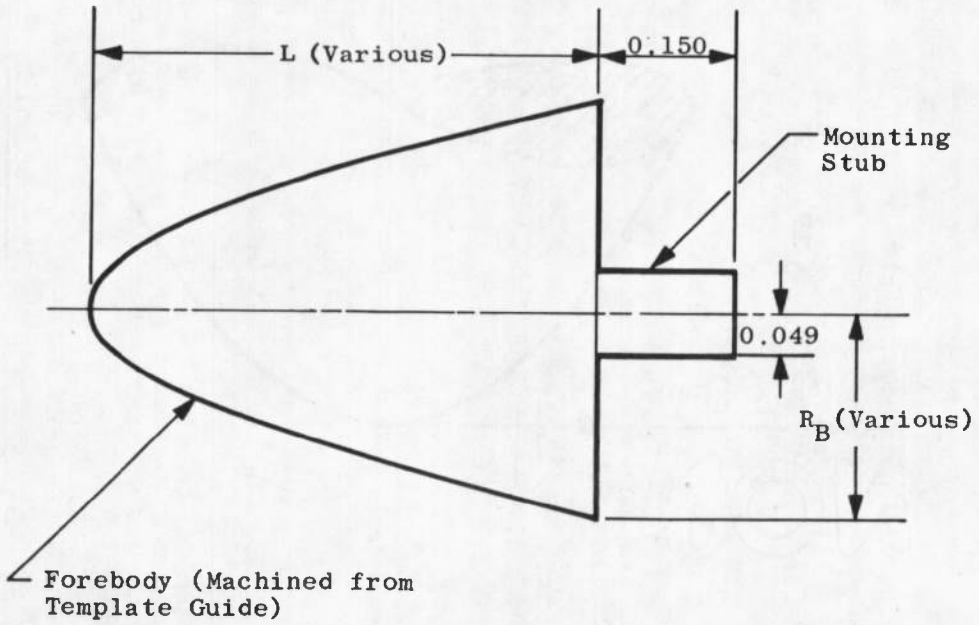

Fig. 4 Drag Model Construction

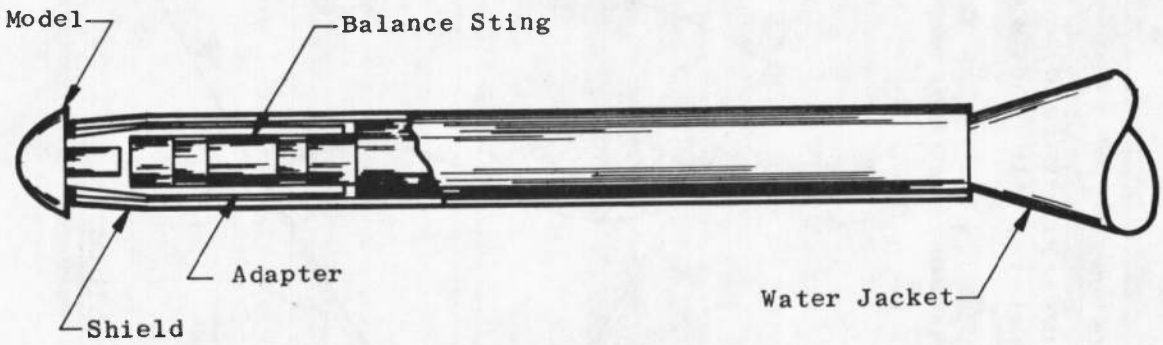

Fig. 5 Drag Test Model Mounting

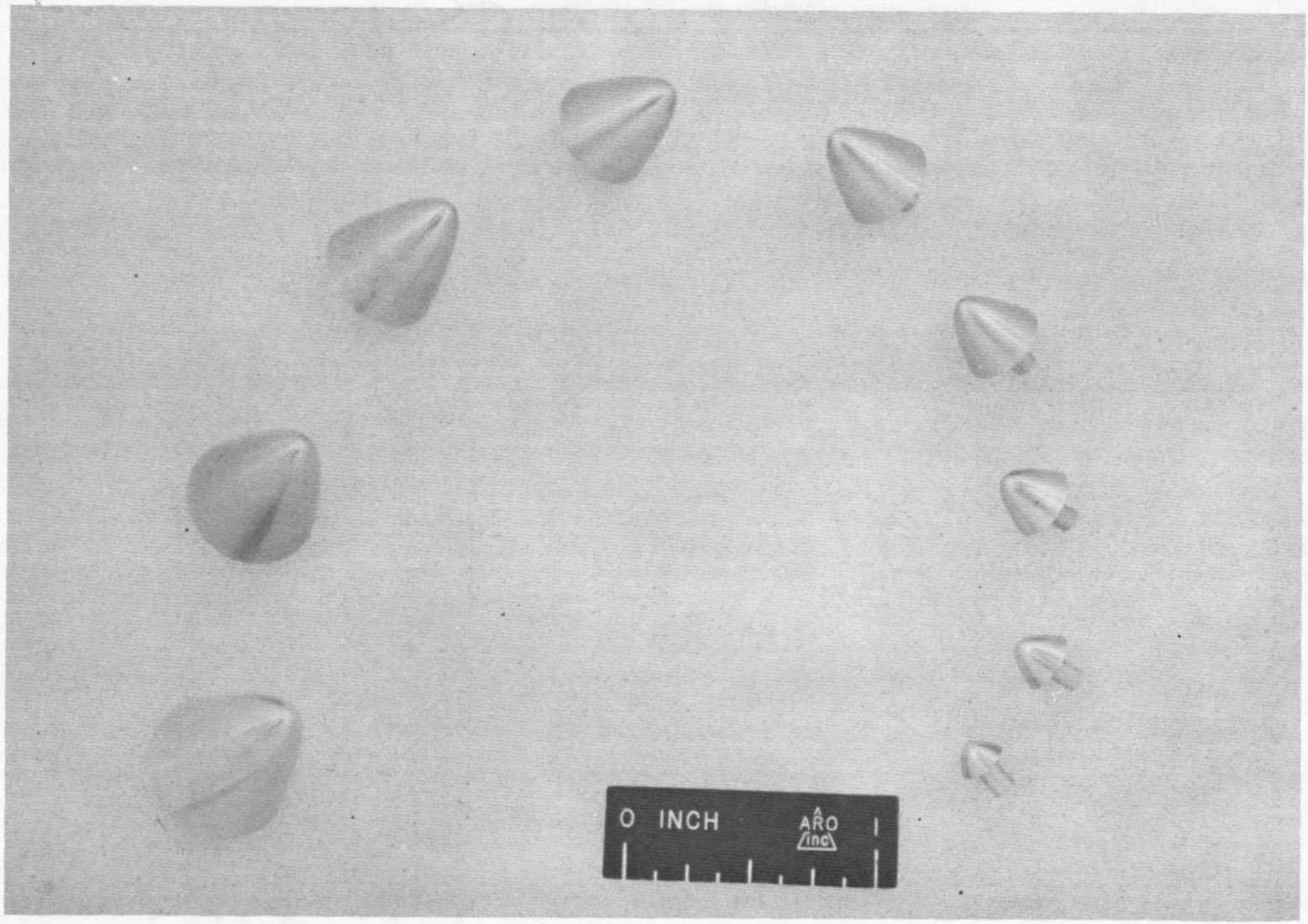

Fig. 6 Drag Models, H/.05/10/.300 Family

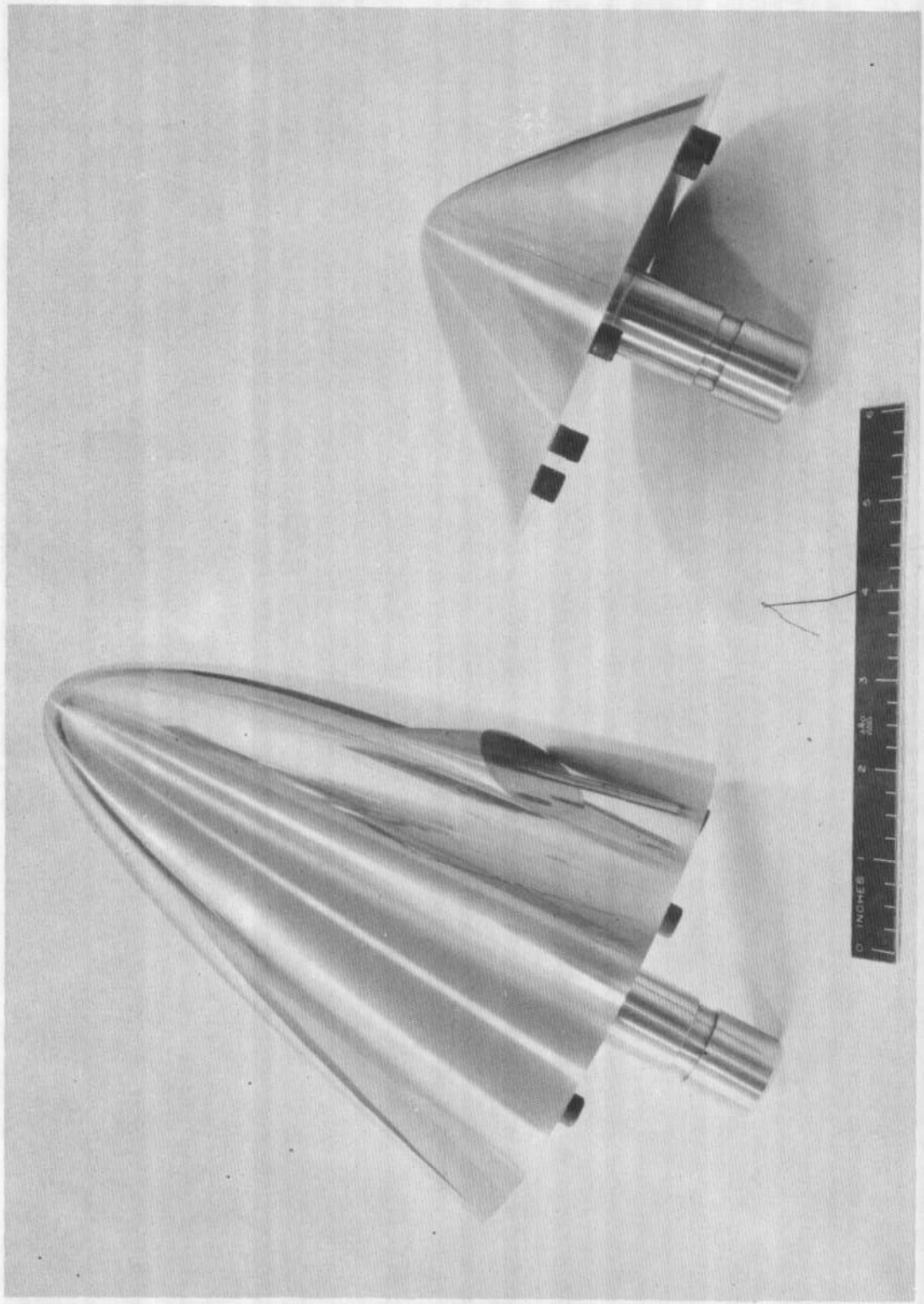

Fig. 7 Hyperboloid Models for High Reynolds Number Tests

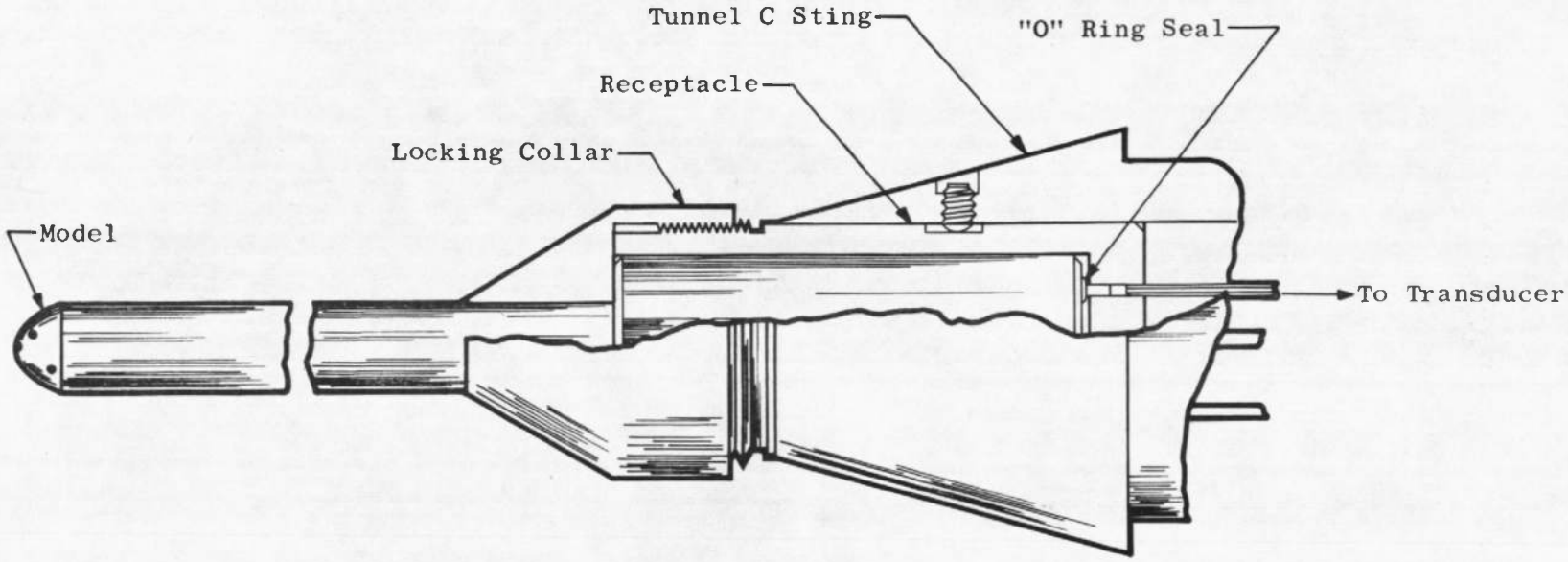

Fig. 8 Pressure Test Mounting, Small Models

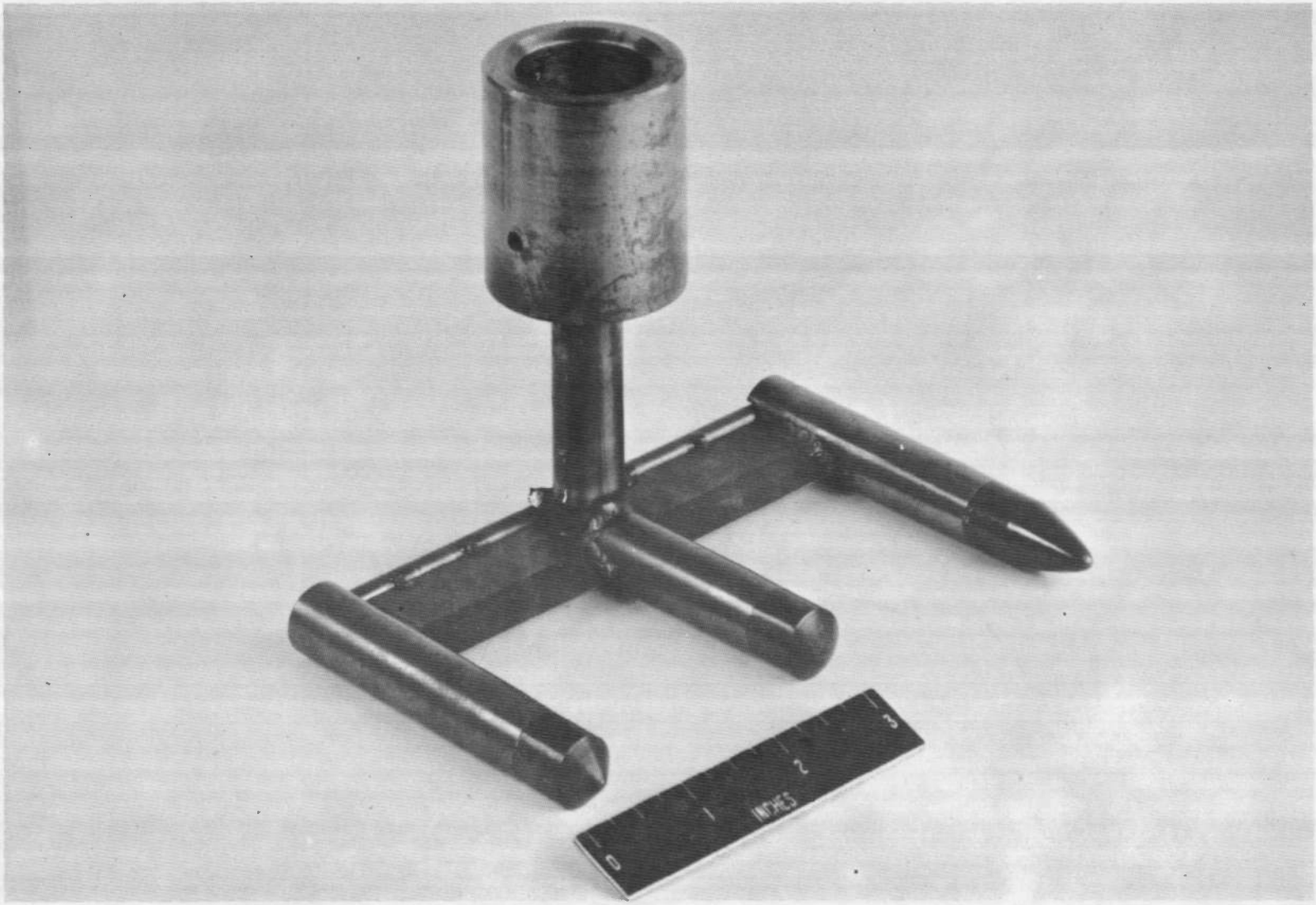

Fig. 9 Skin Temperature Model Mounting, Tunnel C Tests

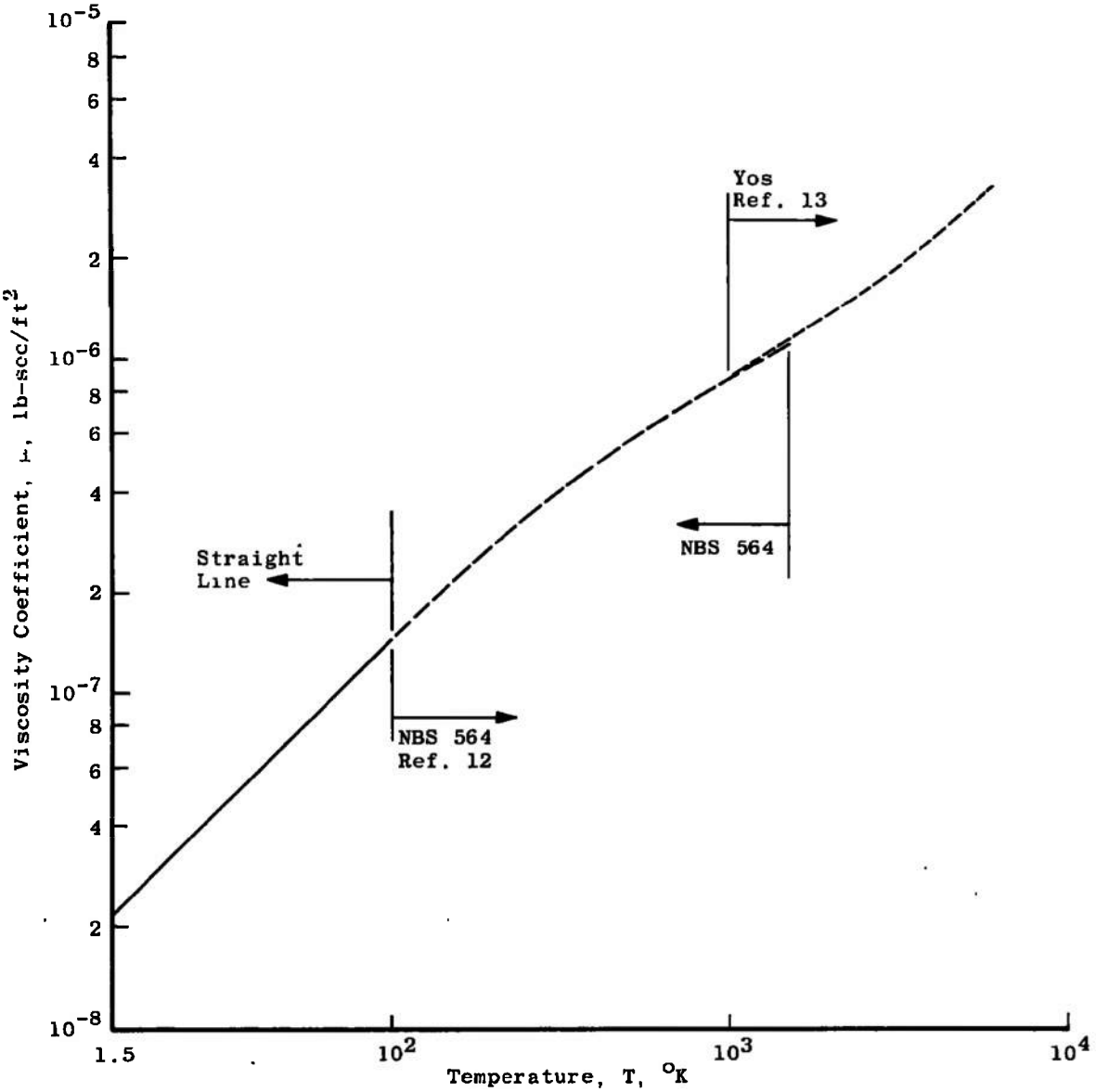

a. For Air

Fig. 10 Viscosity Data

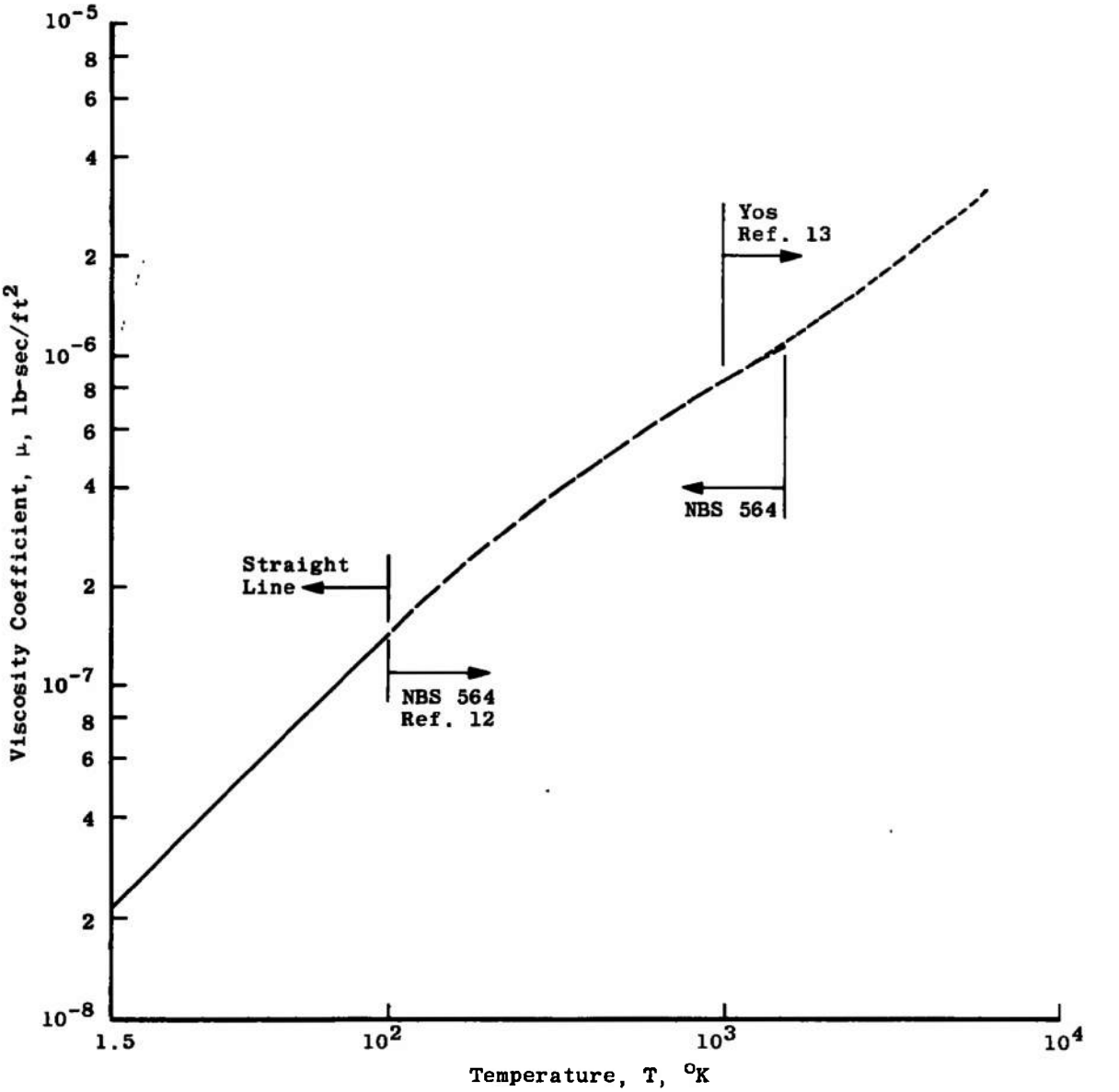

b. For Nitrogen

Fig. 10 Concluded

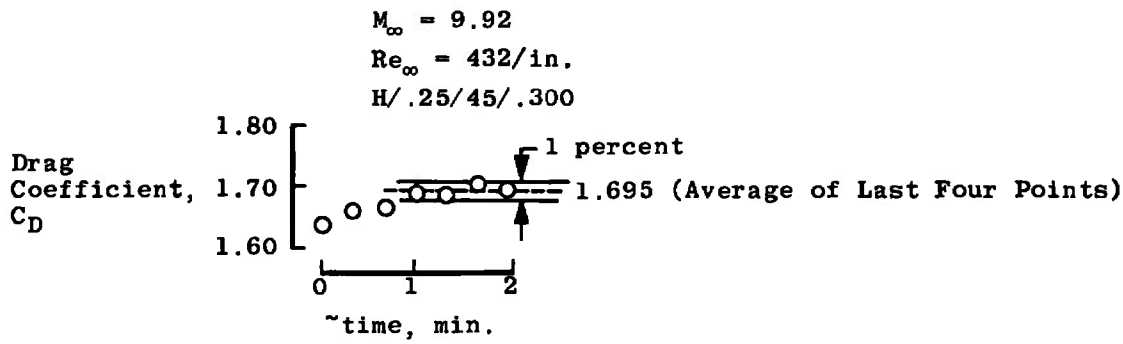

a. Example of Drag Data

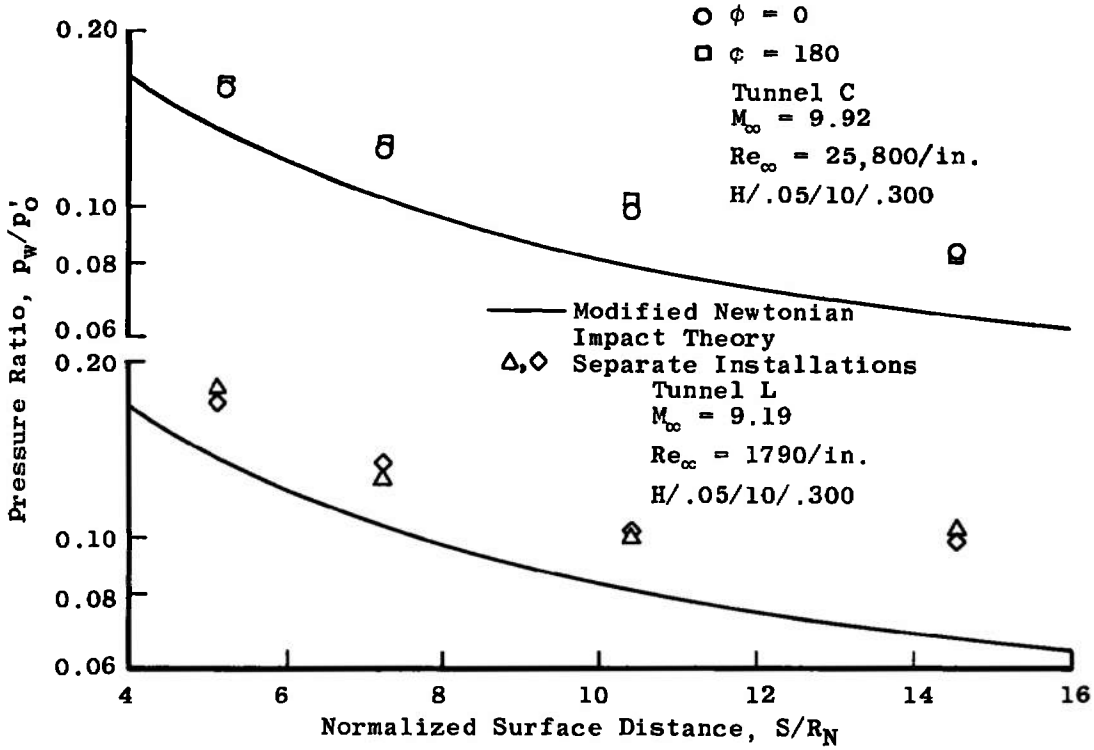

b. Examples of Uncorrected Pressure Data

Fig. 11 Typical Test Data

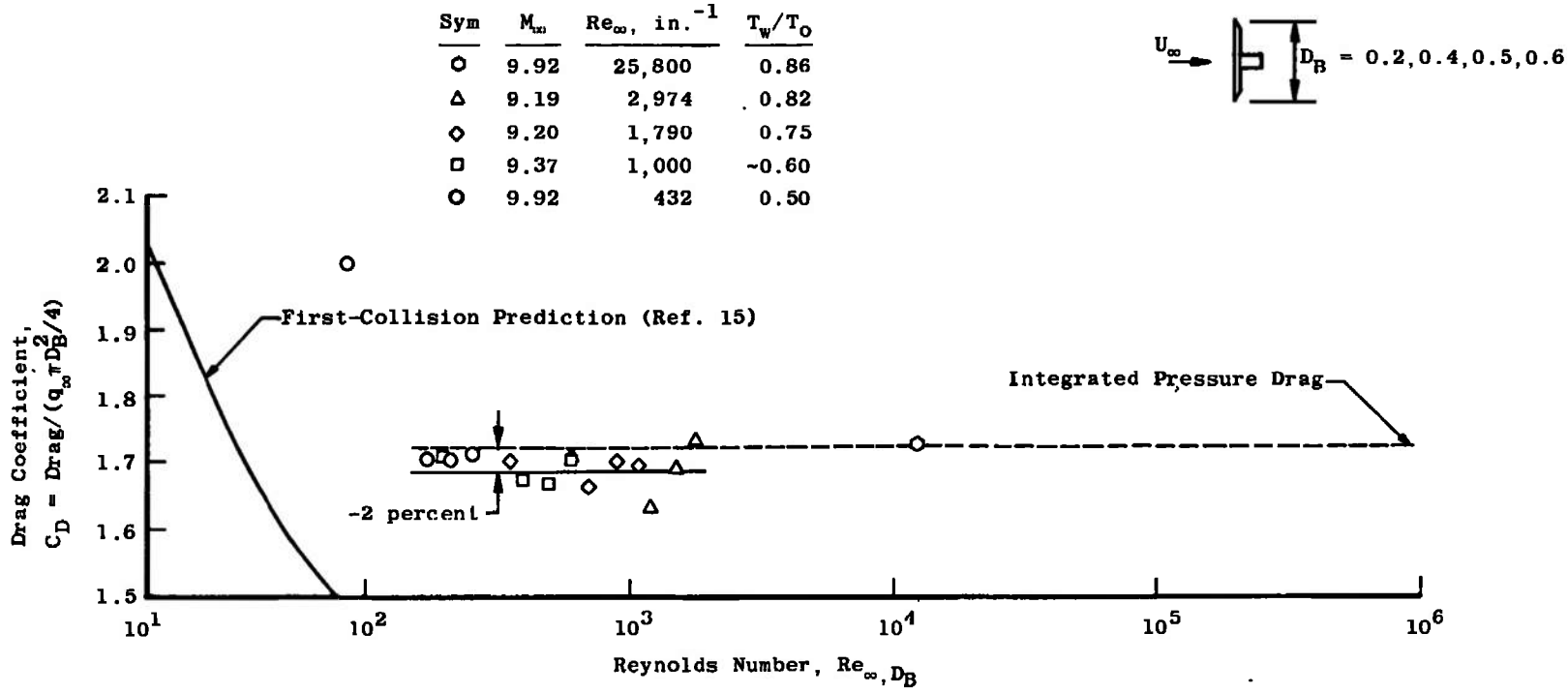

Fig. 12 Flat-Face Disk Drag

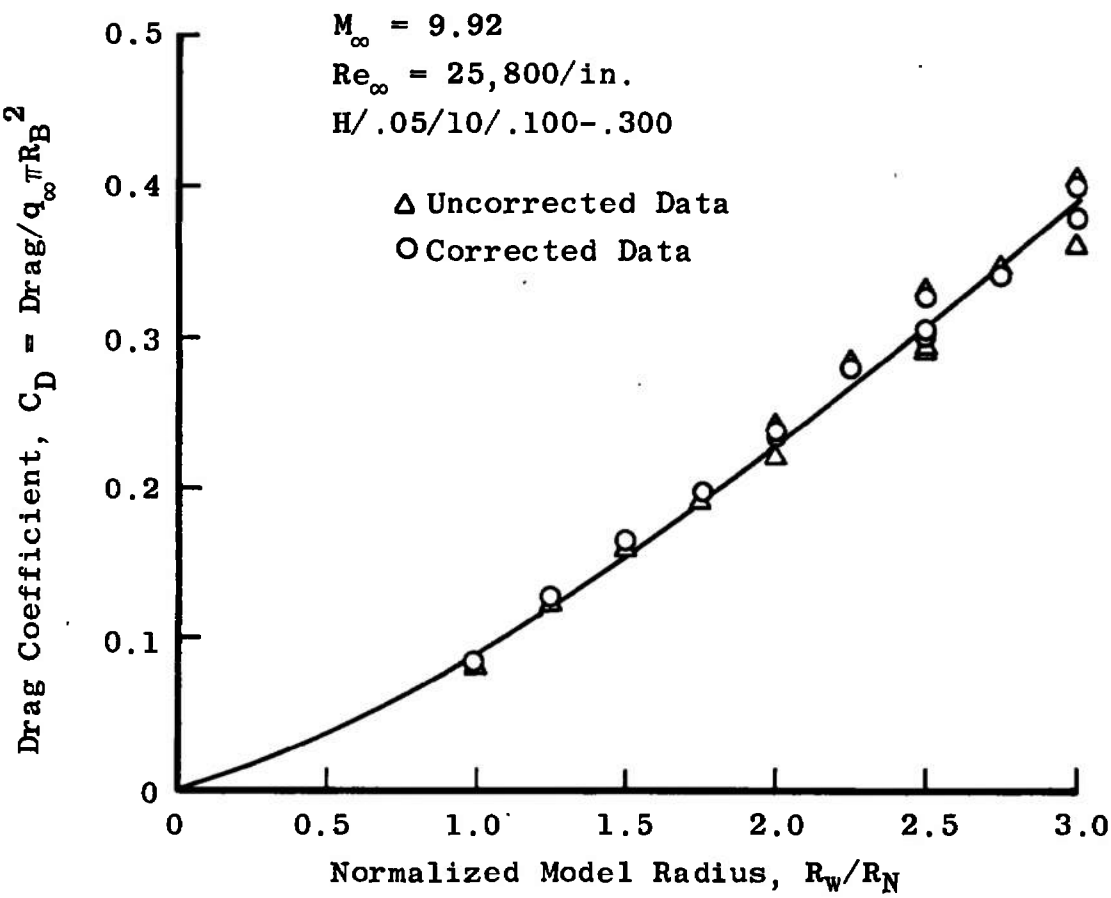

Fig. 13 Effect of Drag Data Correction

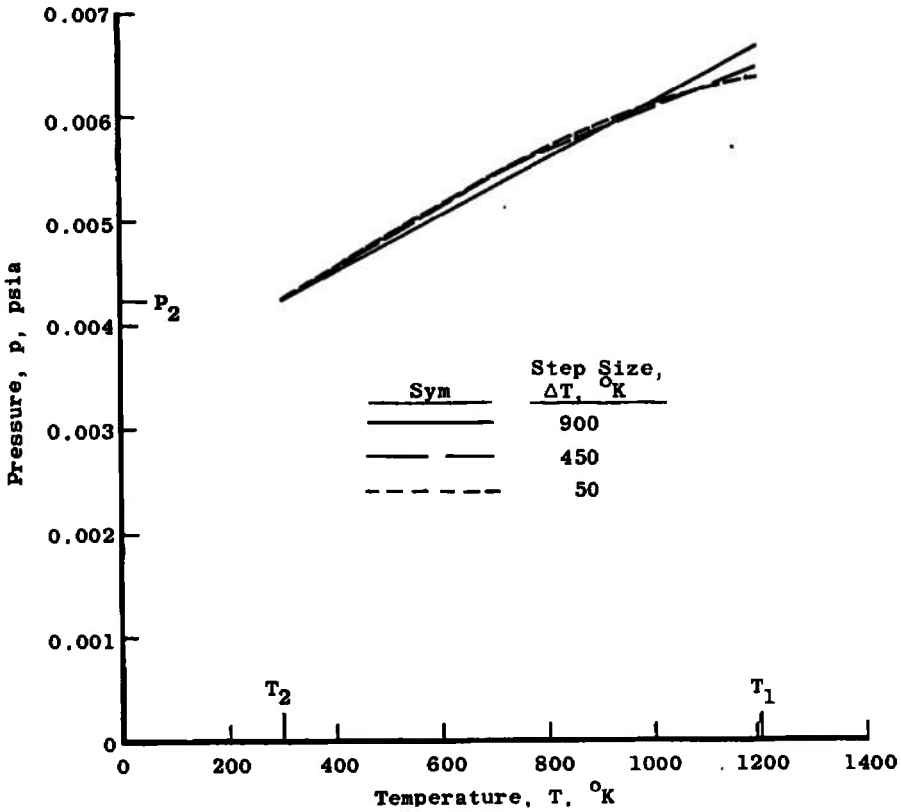

Fig. 14 Effect of Temperature Stepsize on Thermal Transpiration Correction

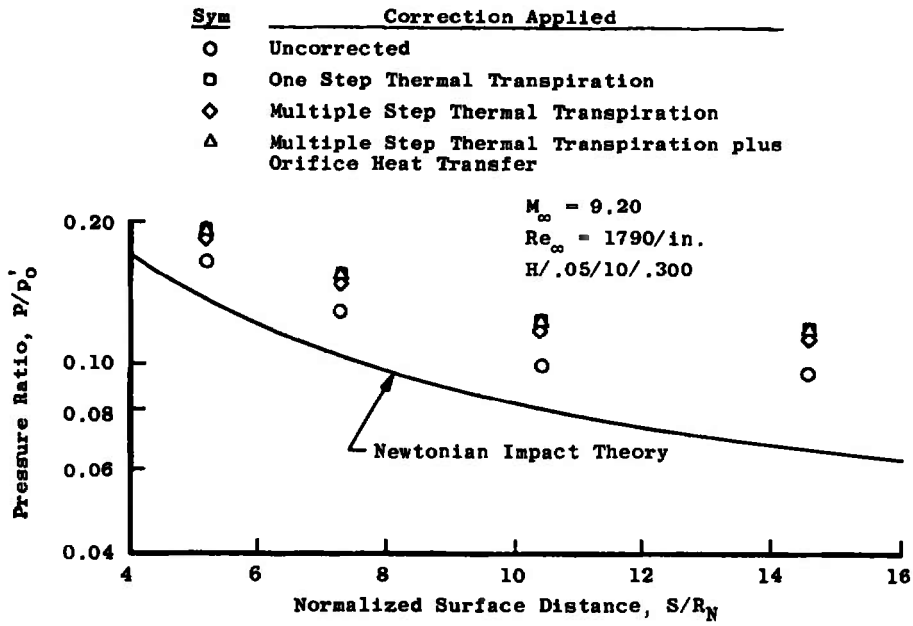

Fig. 15 Effect of Pressure Correction

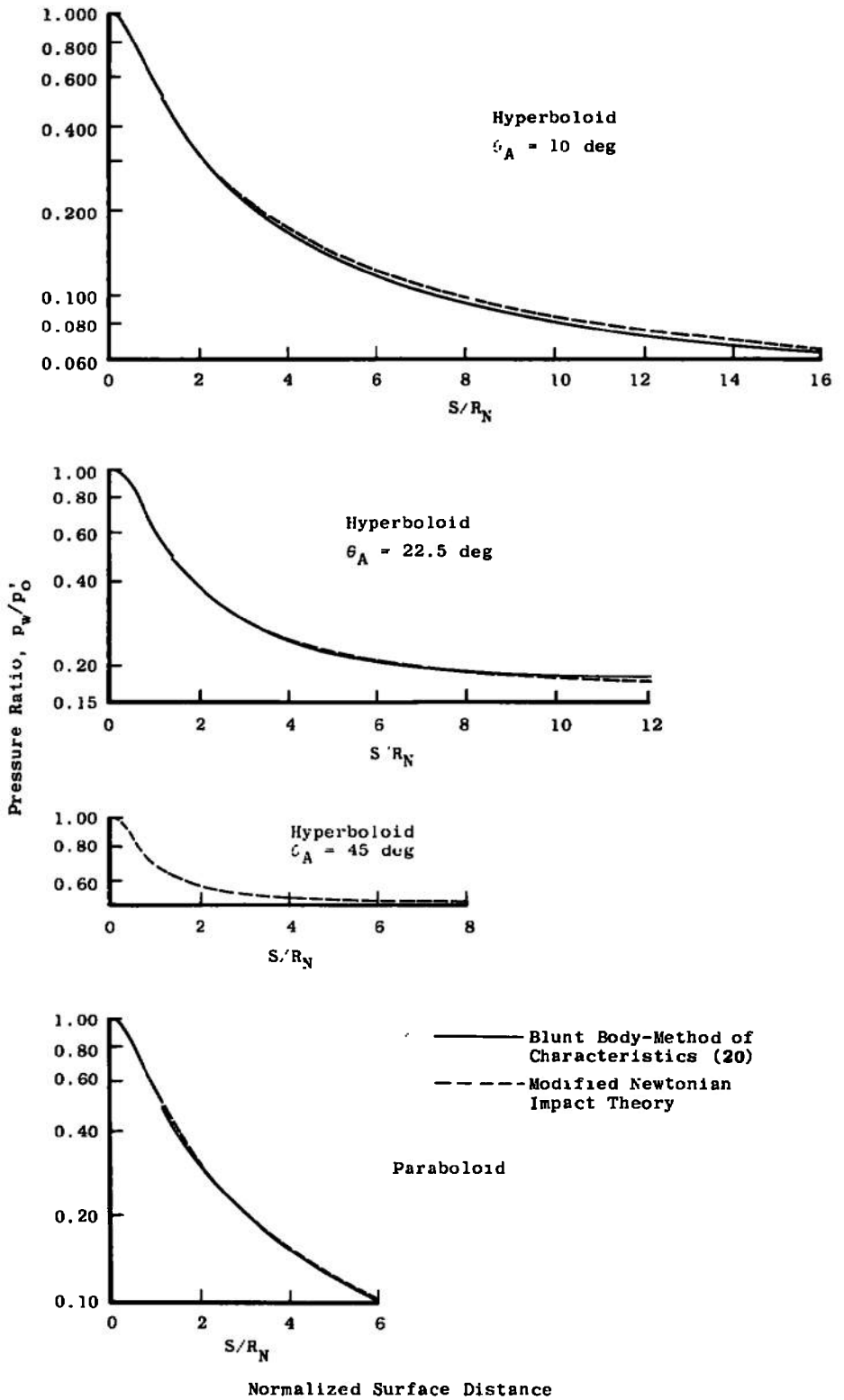

Fig. 16 Theoretical Inviscid Pressure Distributions

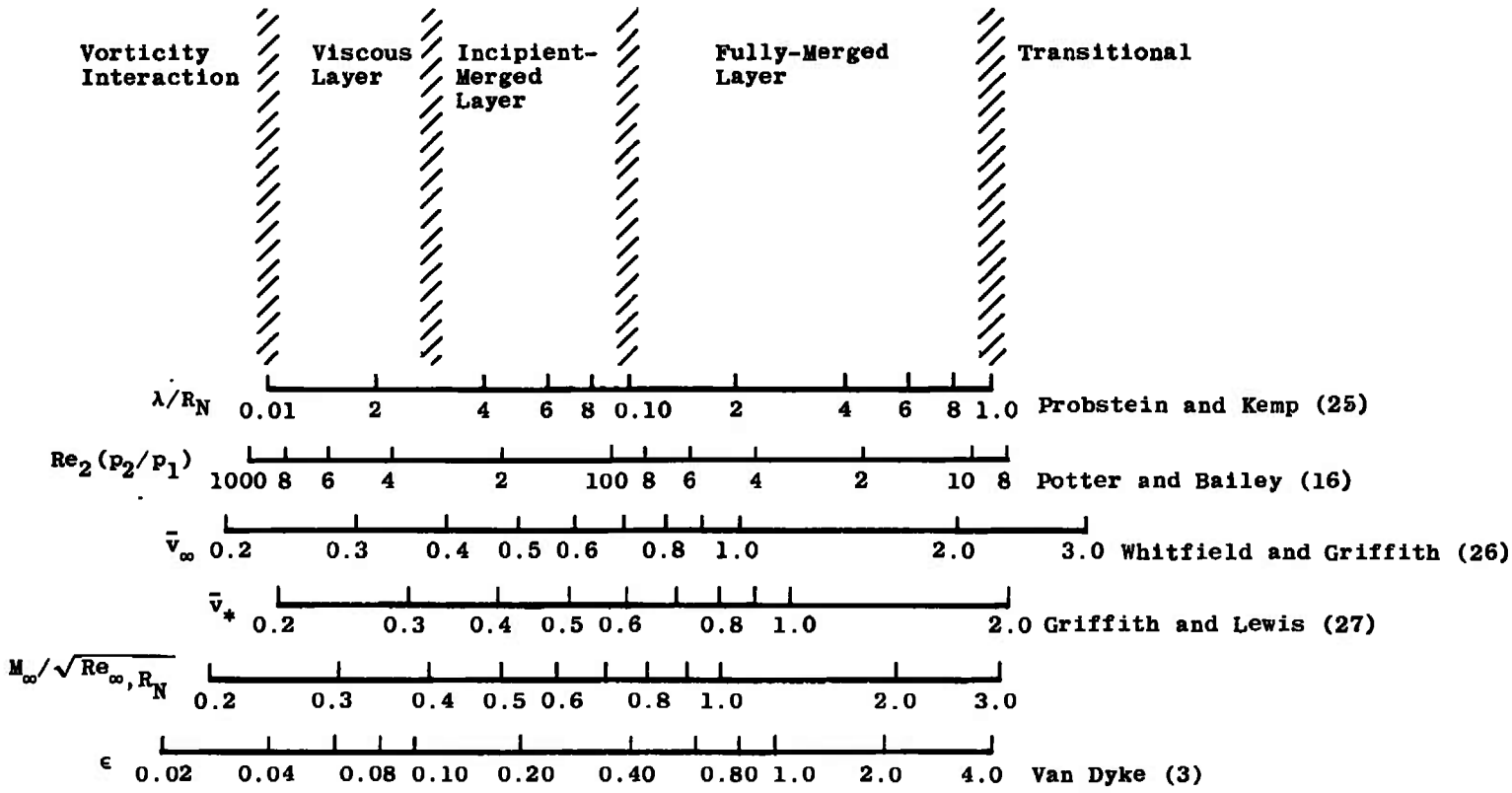

Fig. 17 Viscous Flow Regimes

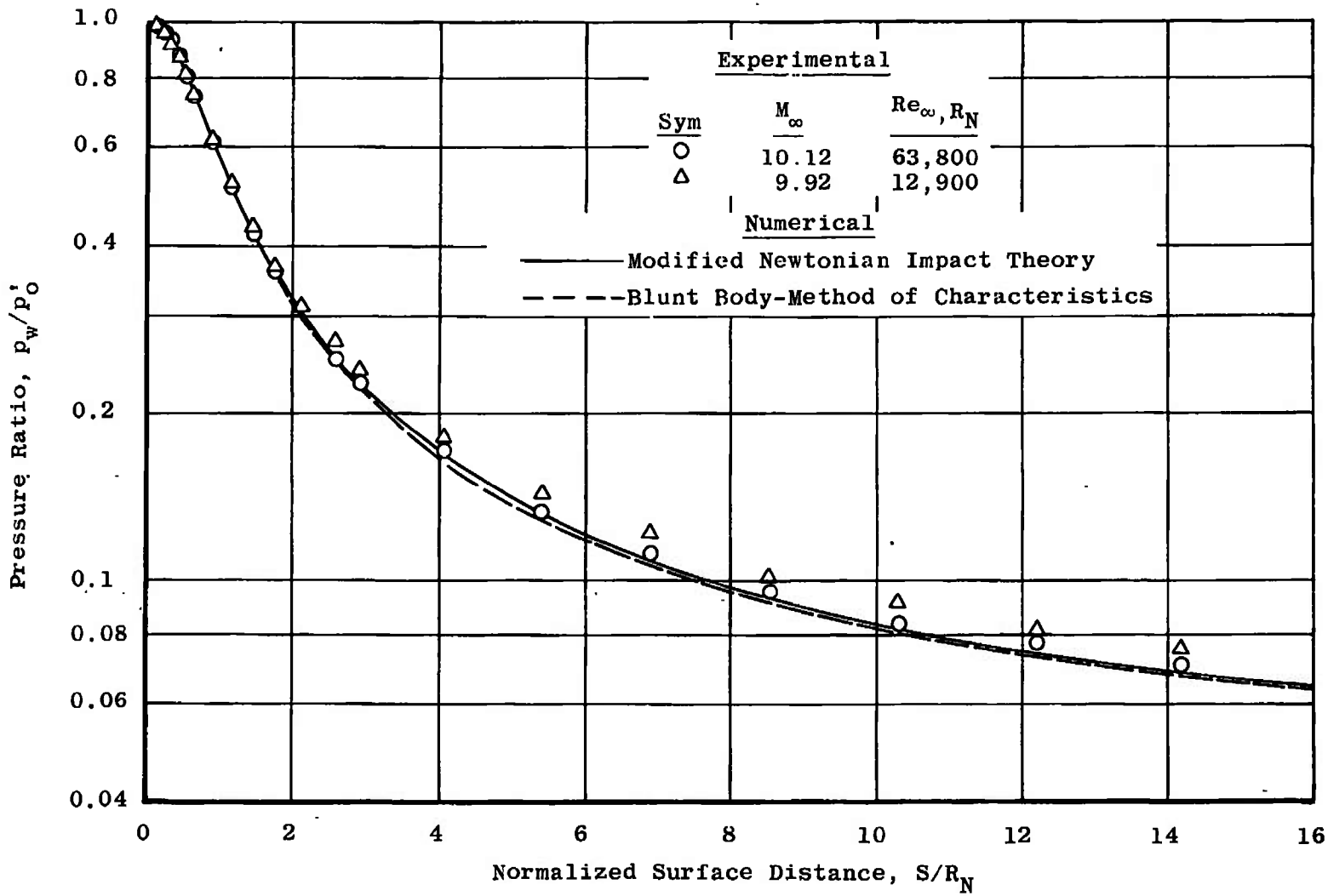

Fig. 18 Surface Pressure at High Reynolds Numbers, 10-deg Hyperboloid

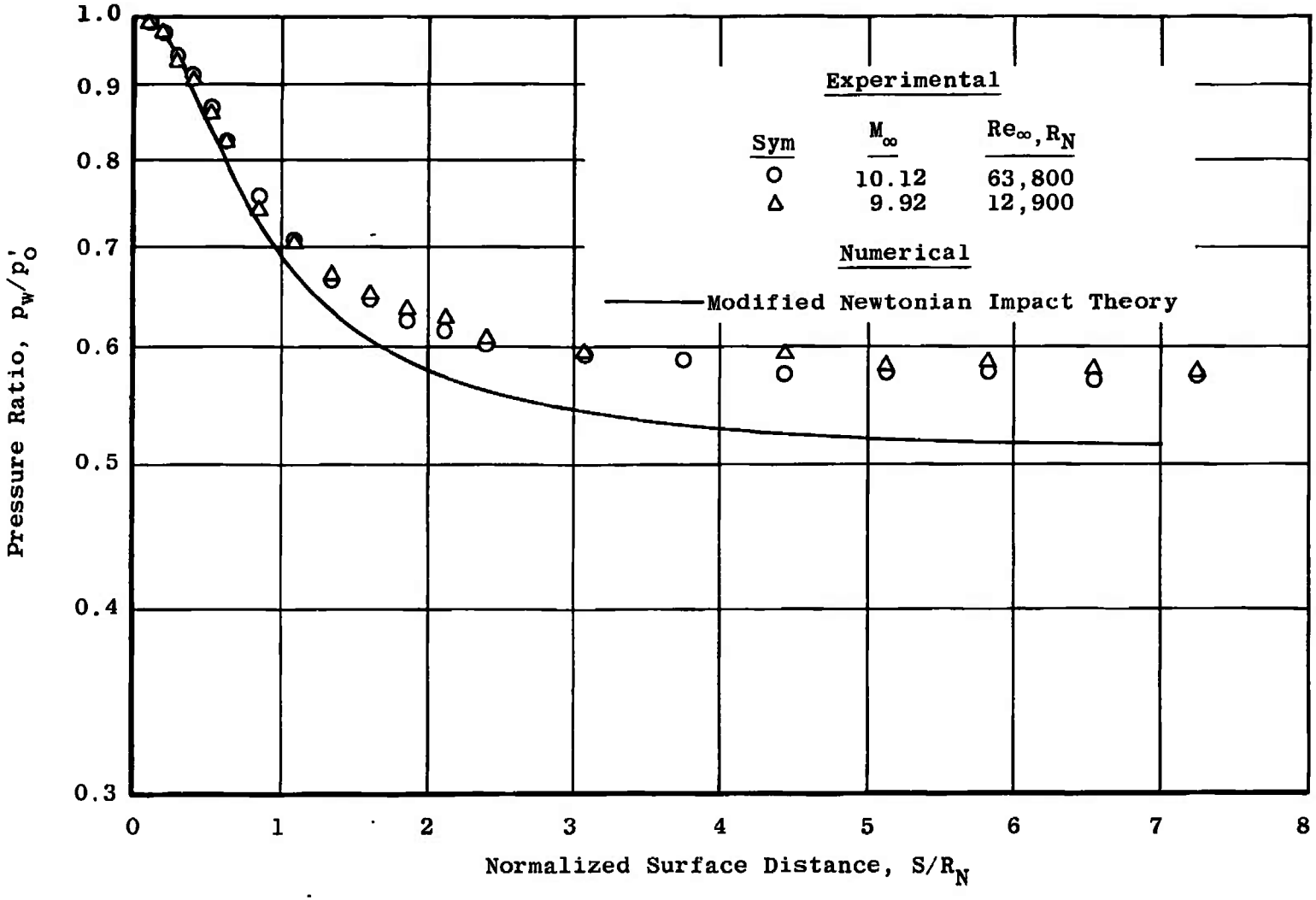

Fig. 19 Surface Pressure at High Reynolds Numbers, 45-deg Hyperboloid

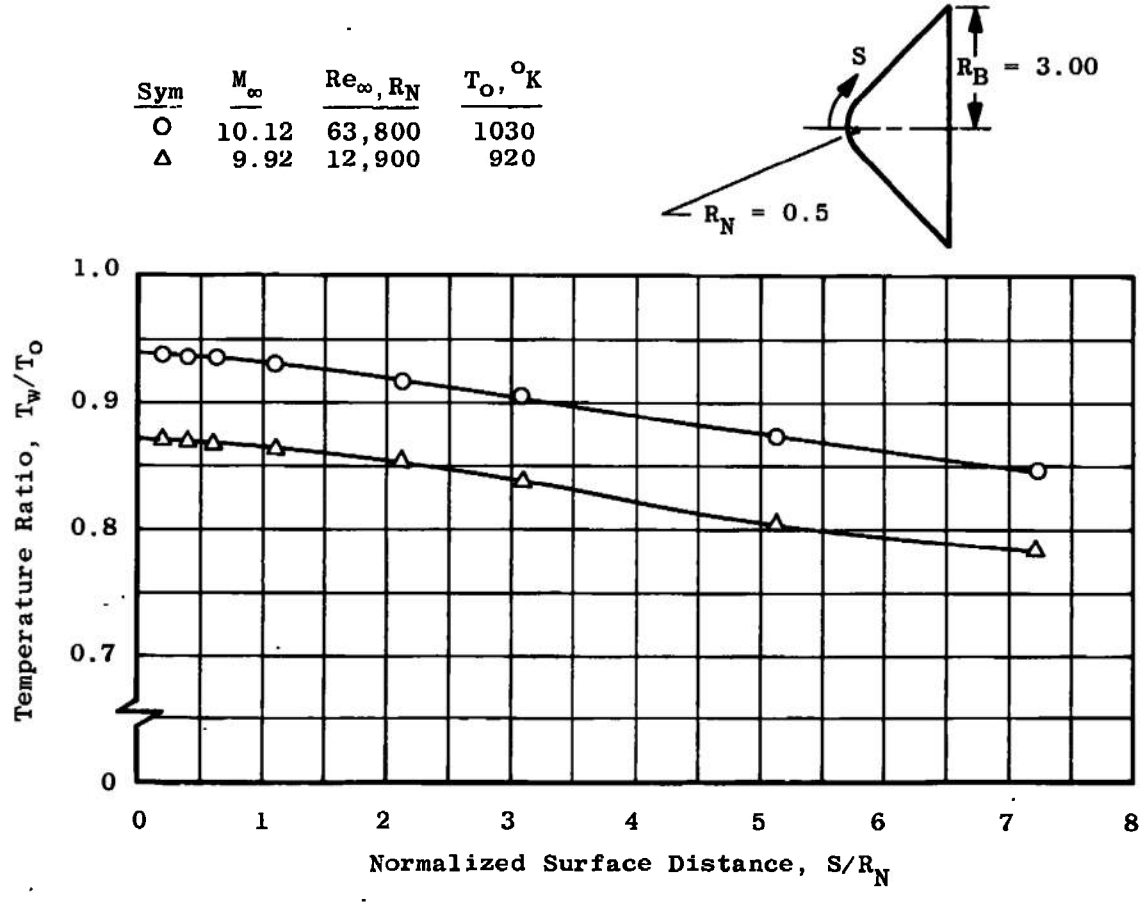

a. 45-deg Hyperboloid

Fig. 20 Steady-State Surface Temperature Distributions at High Reynolds Numbers

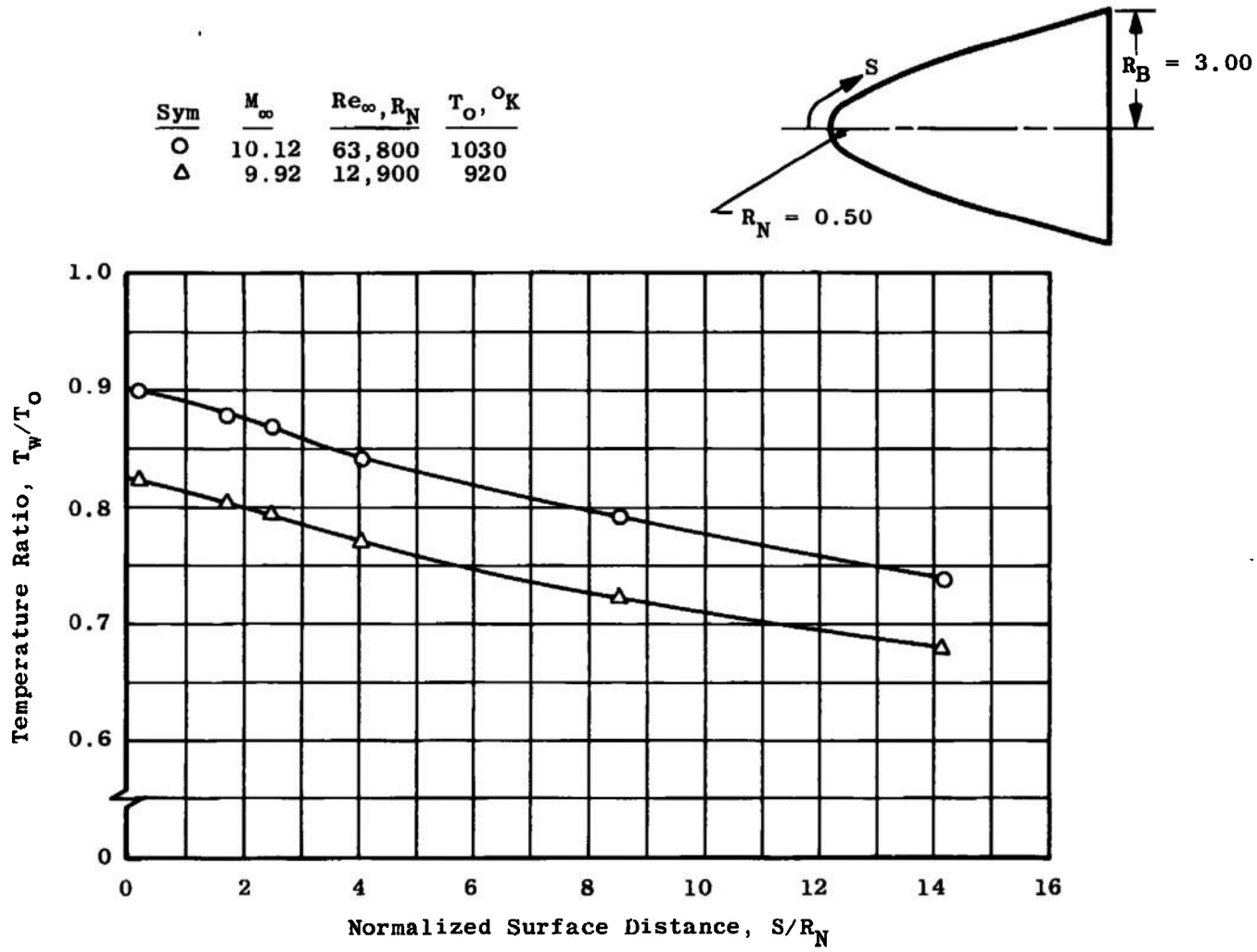

b. 10-deg Hyperboloid

Fig. 20 Concluded

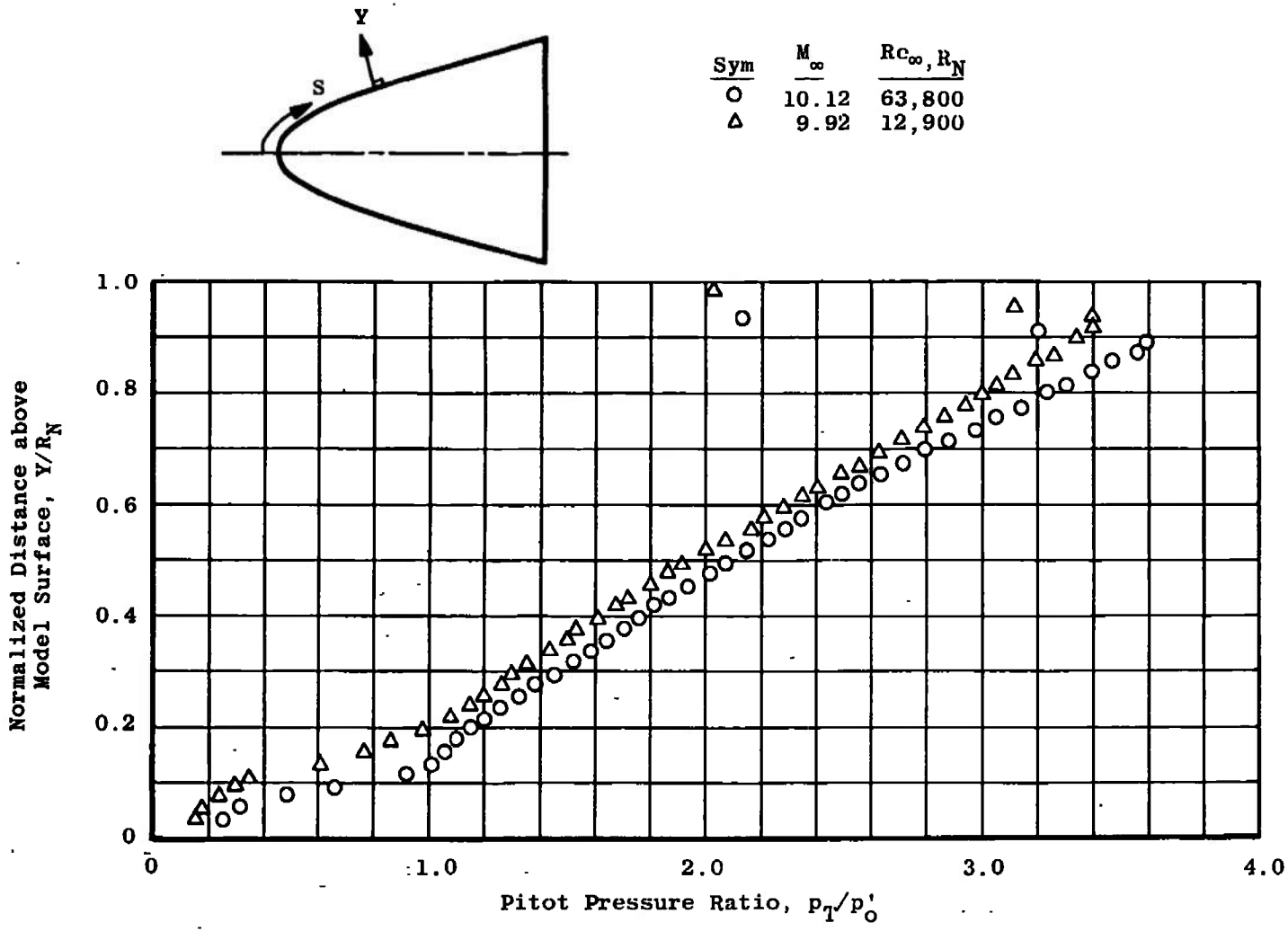

a. $S/R_N' = 2.91$

Fig. 21 Shock-Layer Pitot Pressure Surveys on a 10-deg Hyperboloid

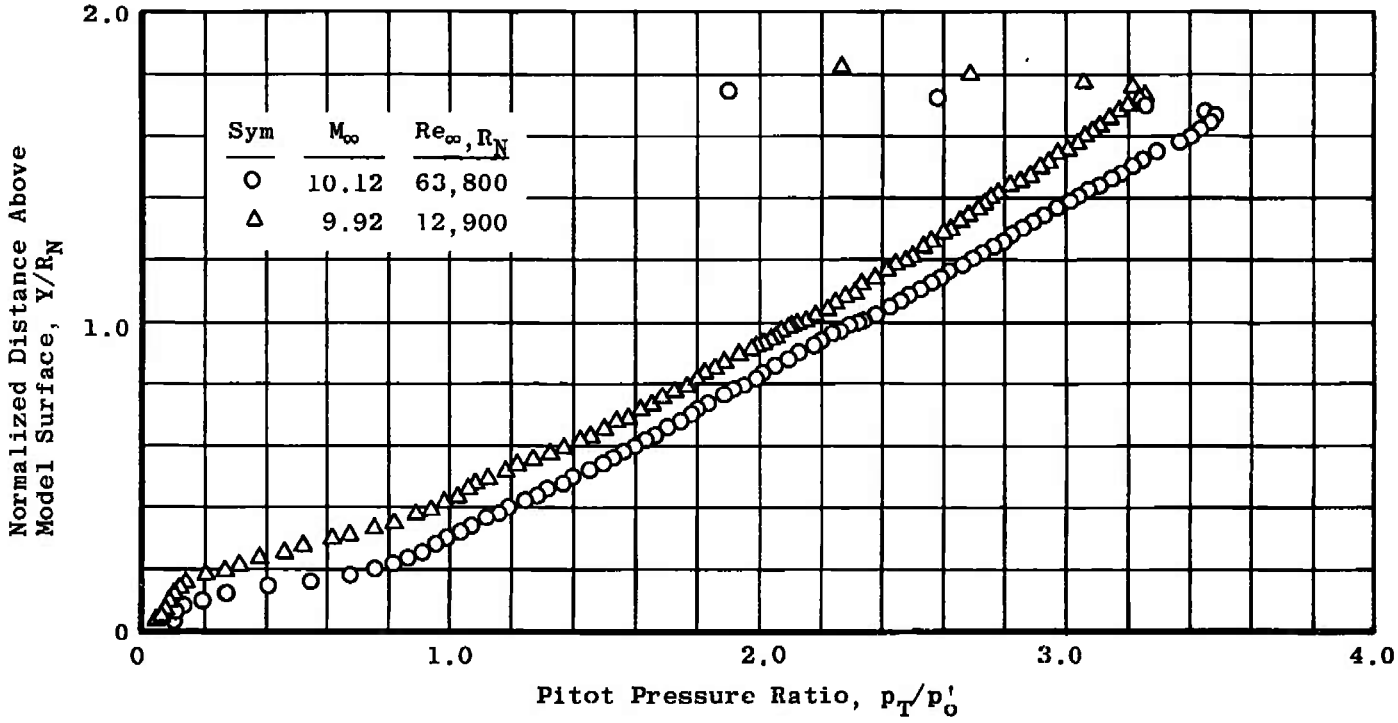

b. S/R_N = 12.20

Fig. 21 Concluded

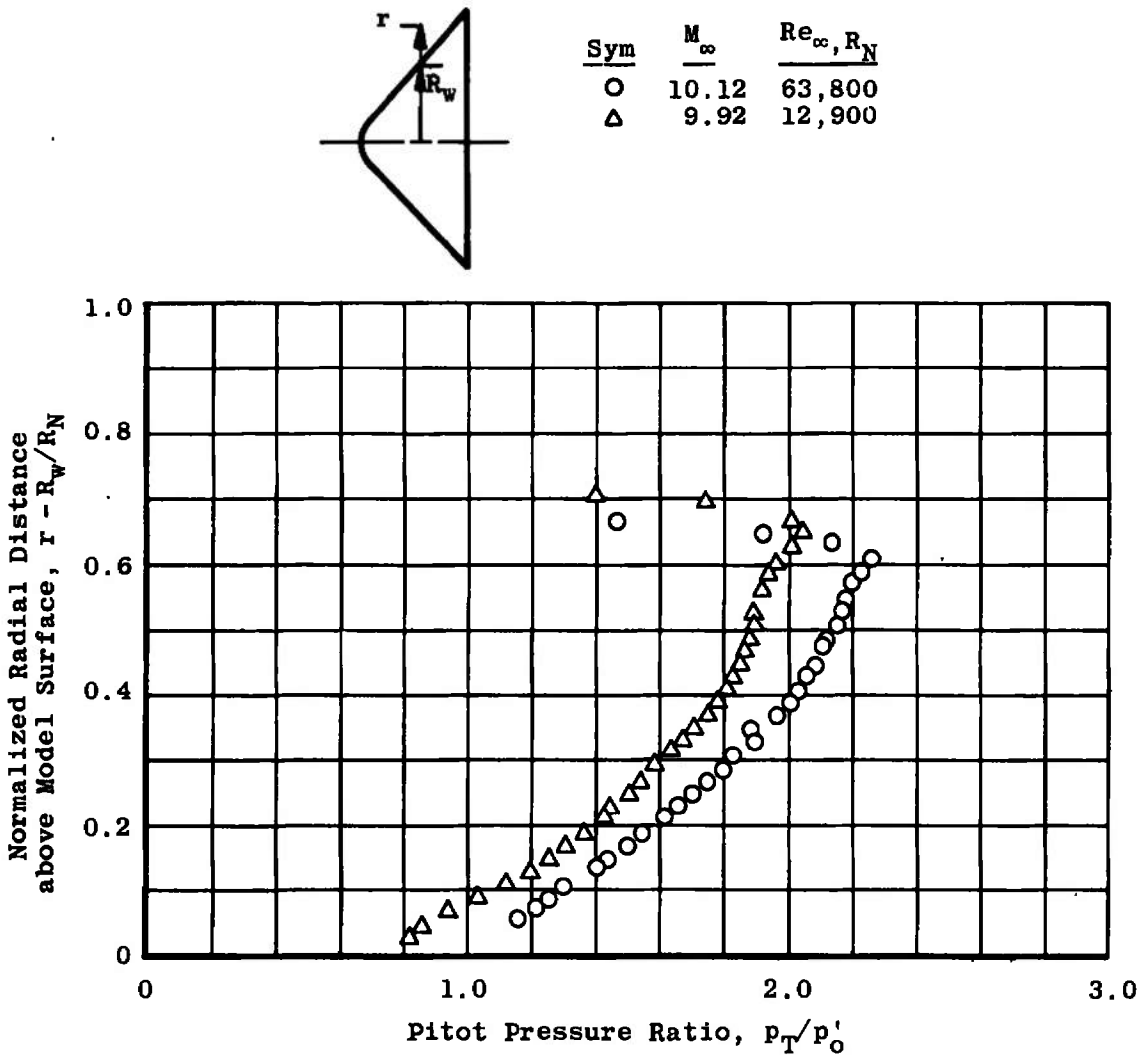

a. $S/R_N = 1.87$

Fig. 22 Shock-Layer Pitot Pressure Surveys on a 45-deg Hyperboloid

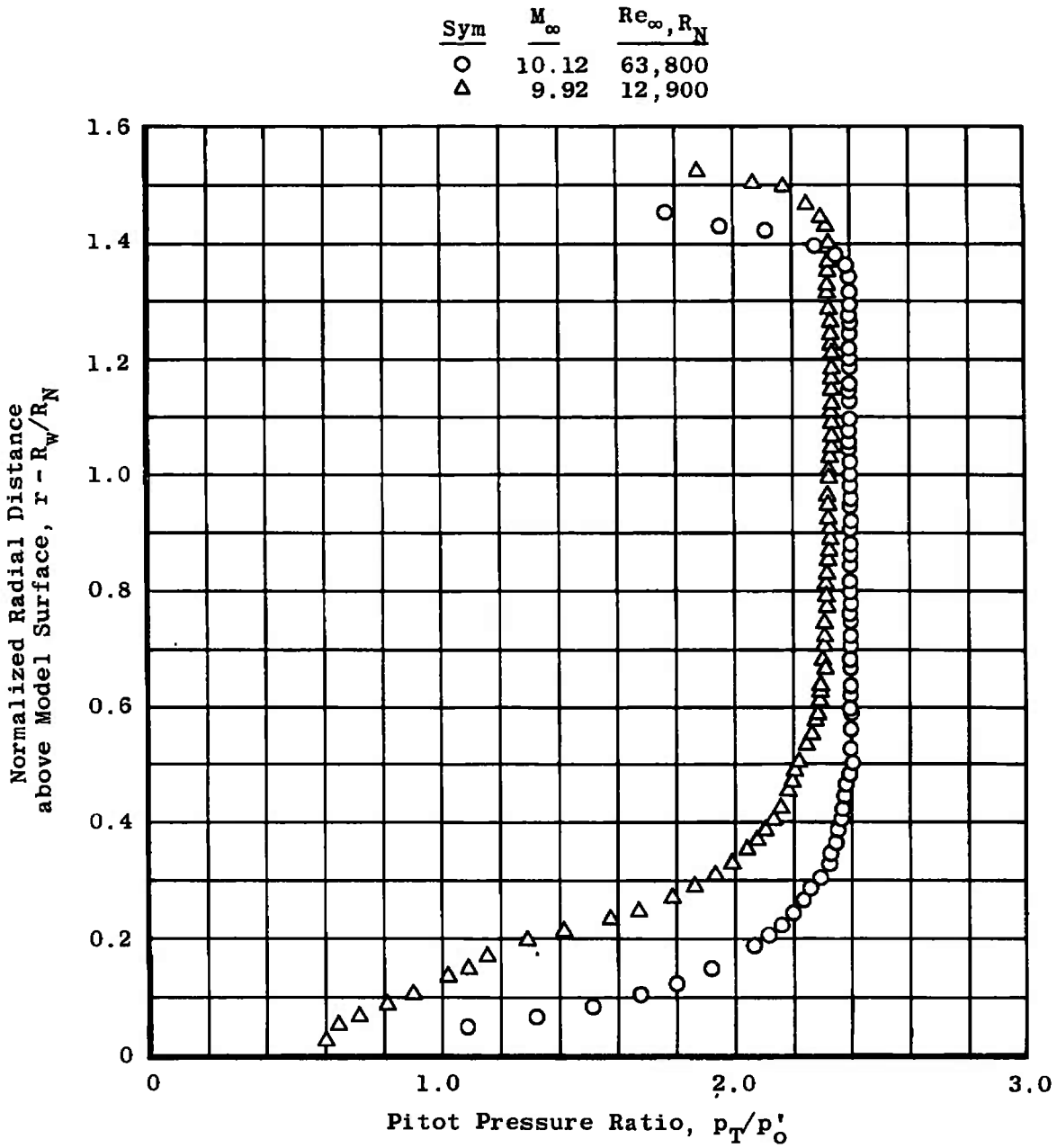

b. $S/R_N = 6.54$

Fig. 22 Concluded

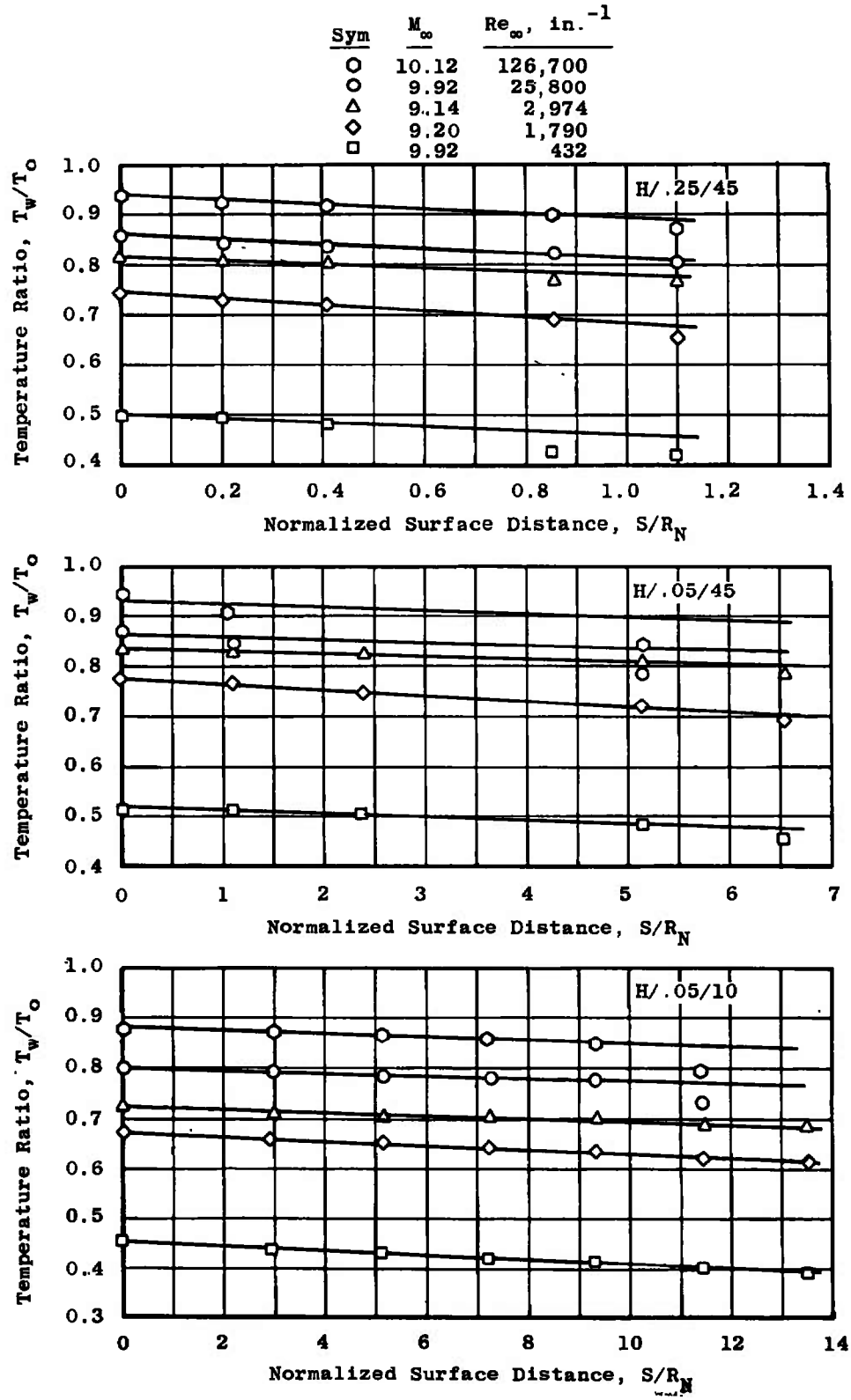

Fig. 23 Steady-State Skin Temperature Data on Hyperboloids at Low Reynolds Numbers

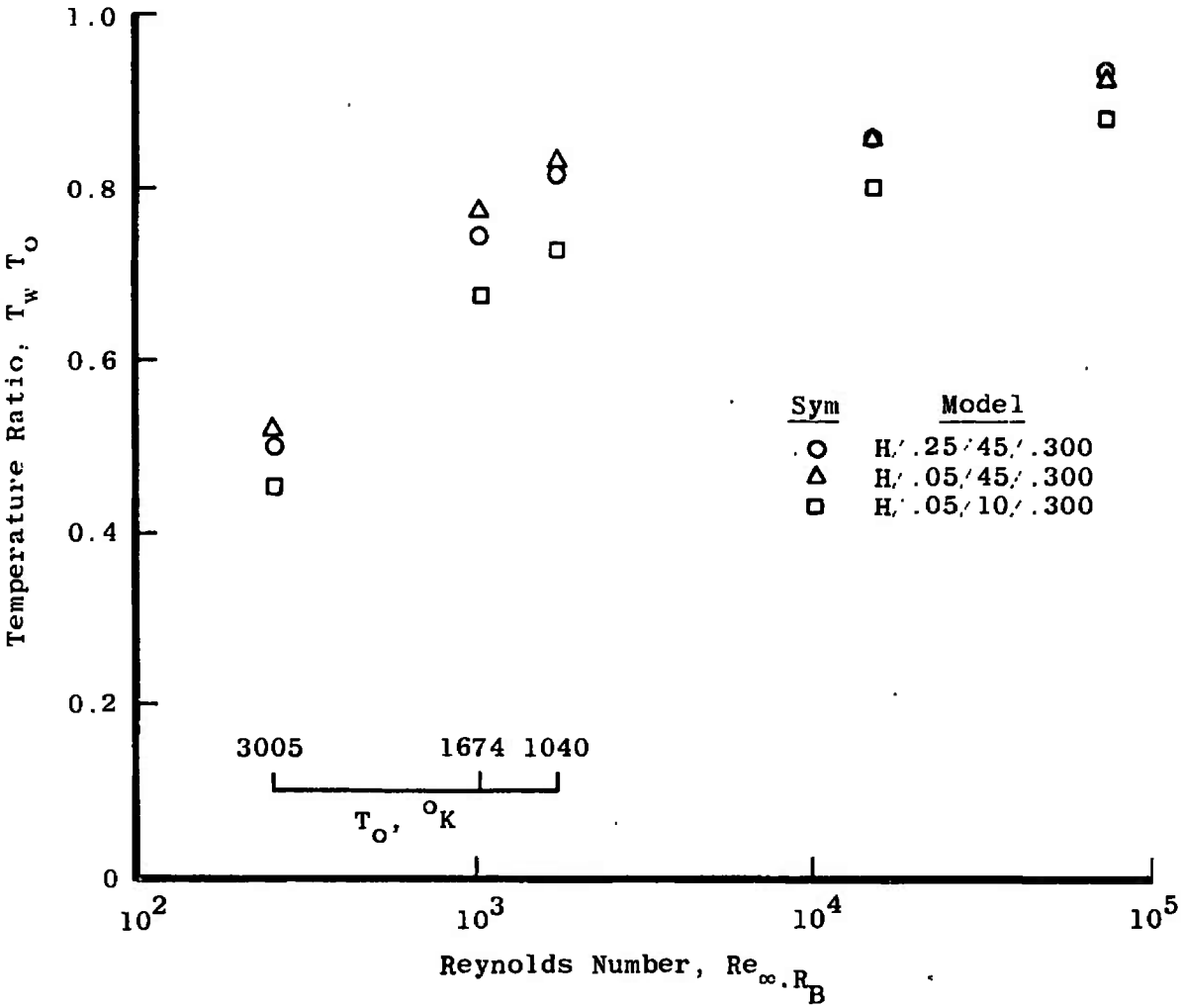

Fig. 24 Effect of Reynolds Number and Stagnation Temperature on Model Stagnation Point Temperature

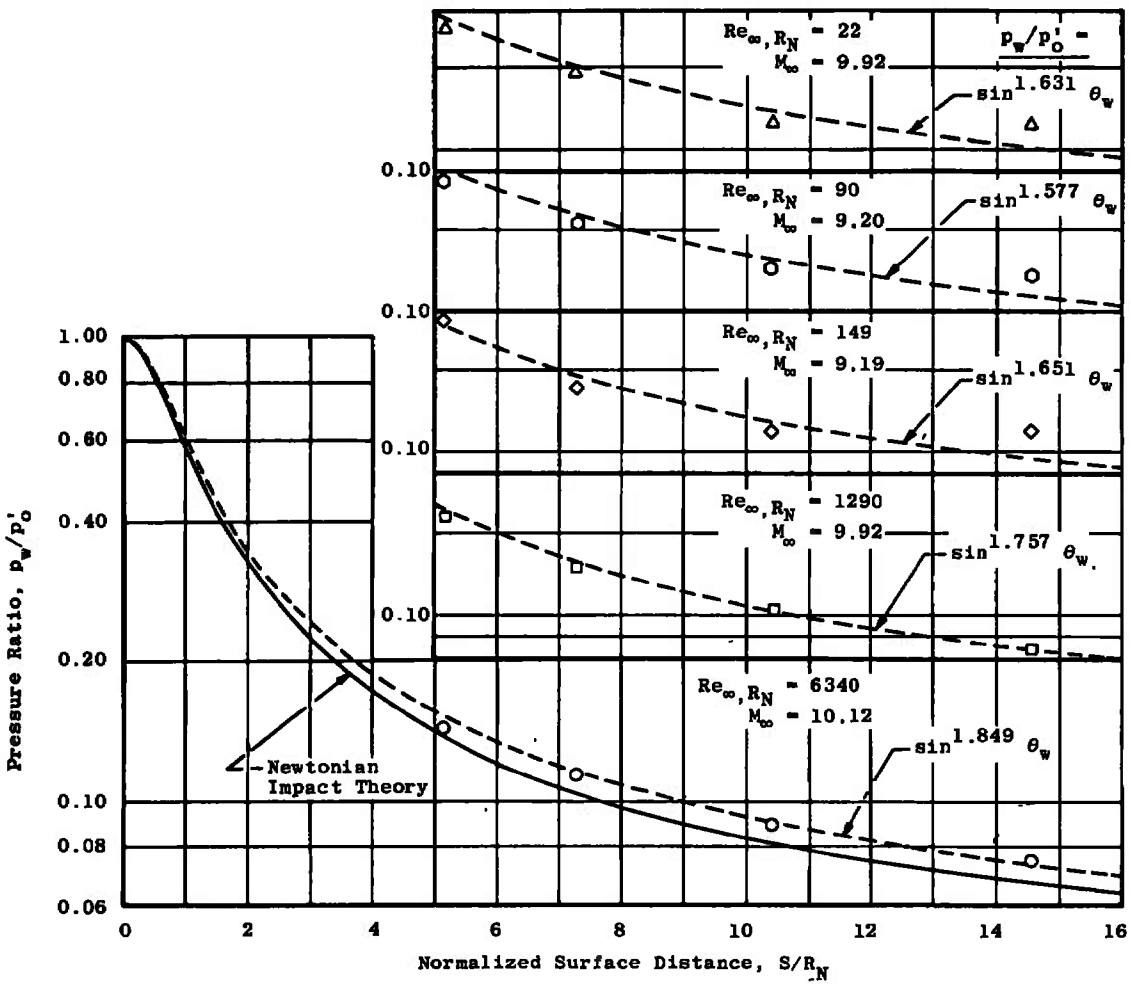

a: H/.05/10/.300

Fig. 25 Pressure Distributions on Hyperboloids and Paraboloids at Low Reynolds Numbers

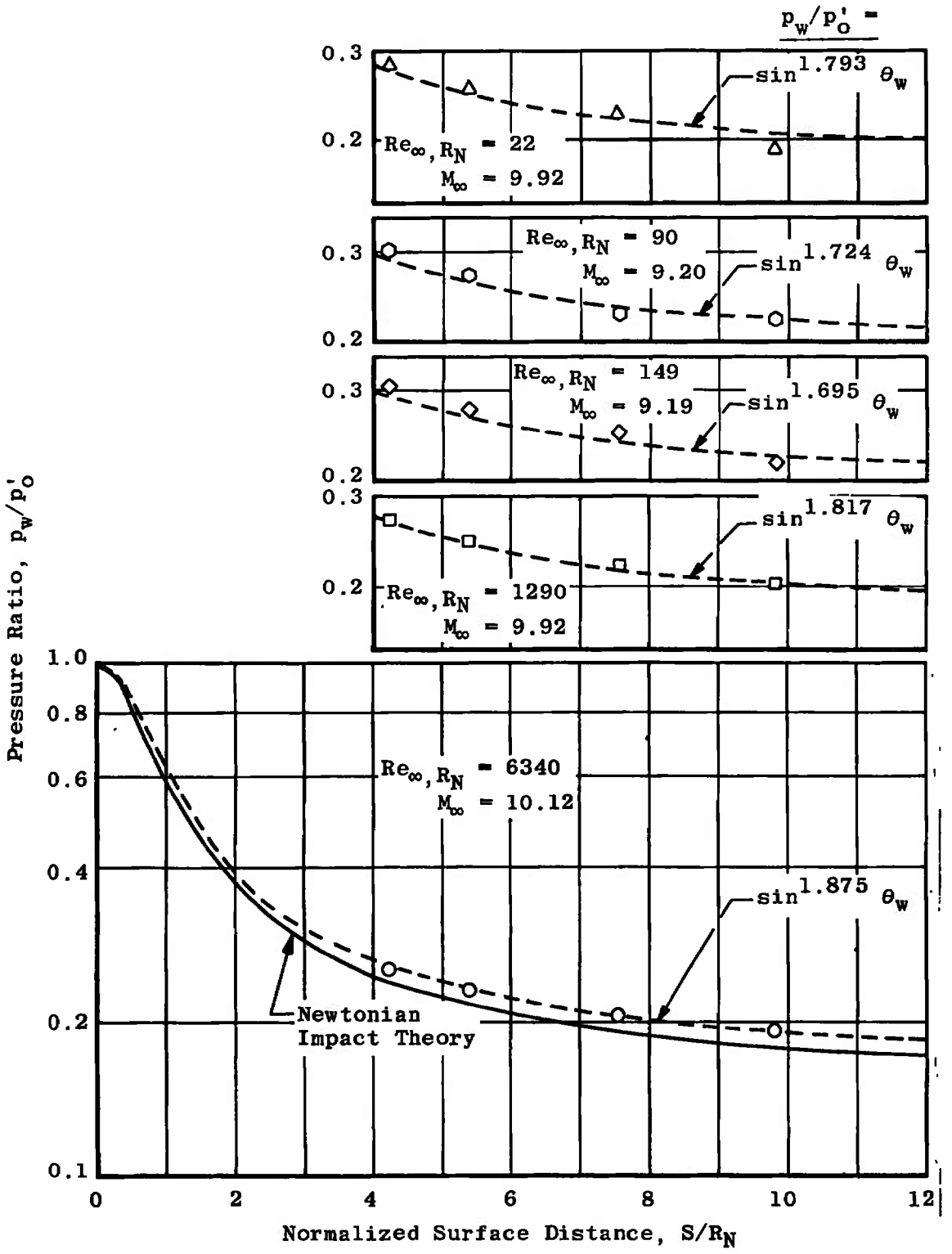

b. H/.05/22.5/.300

Fig. 25 Continued

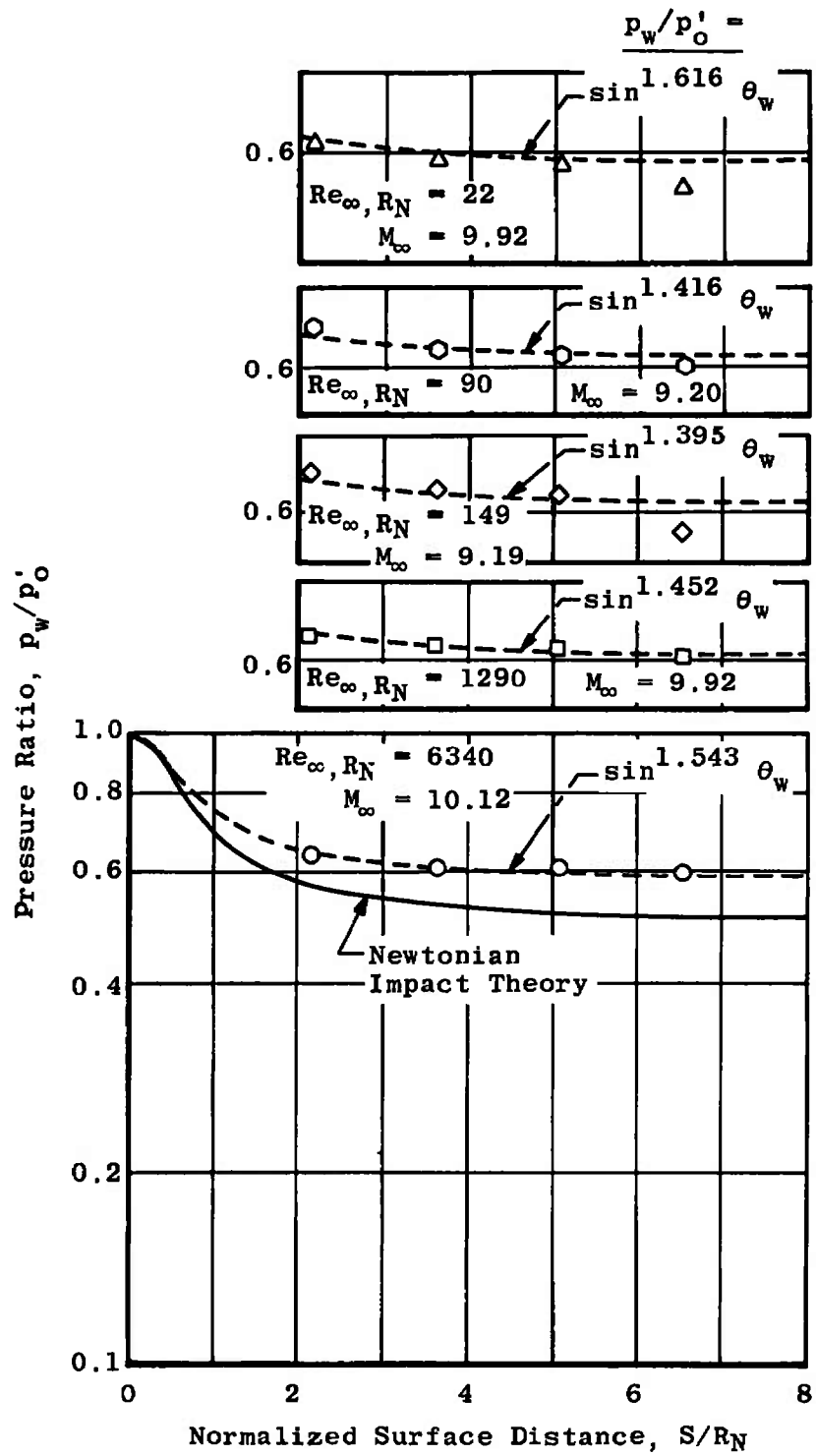

c. H/.05/45/.300

Fig. 25 Continued

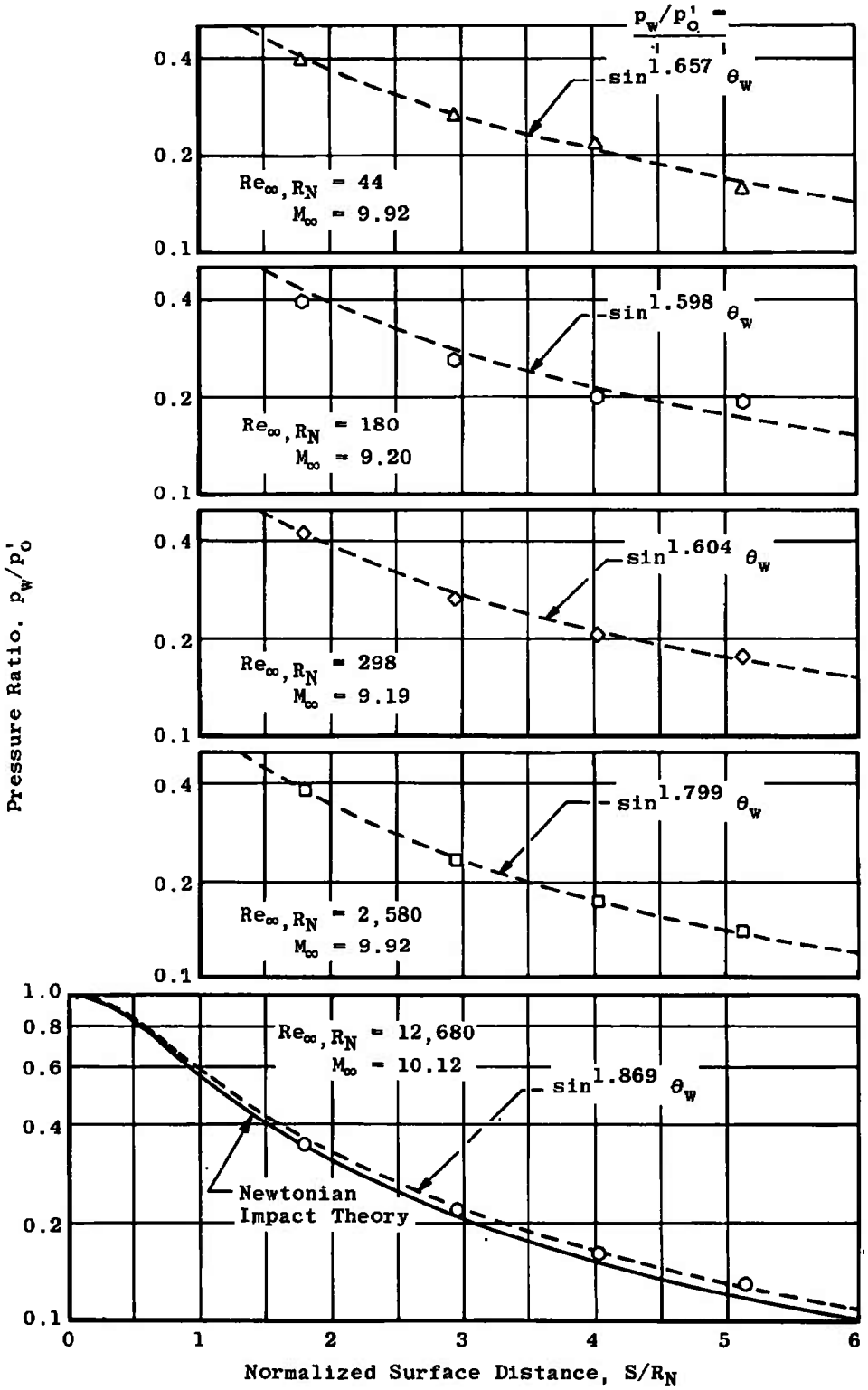

d. P/.10/.300

Fig. 25 Continued

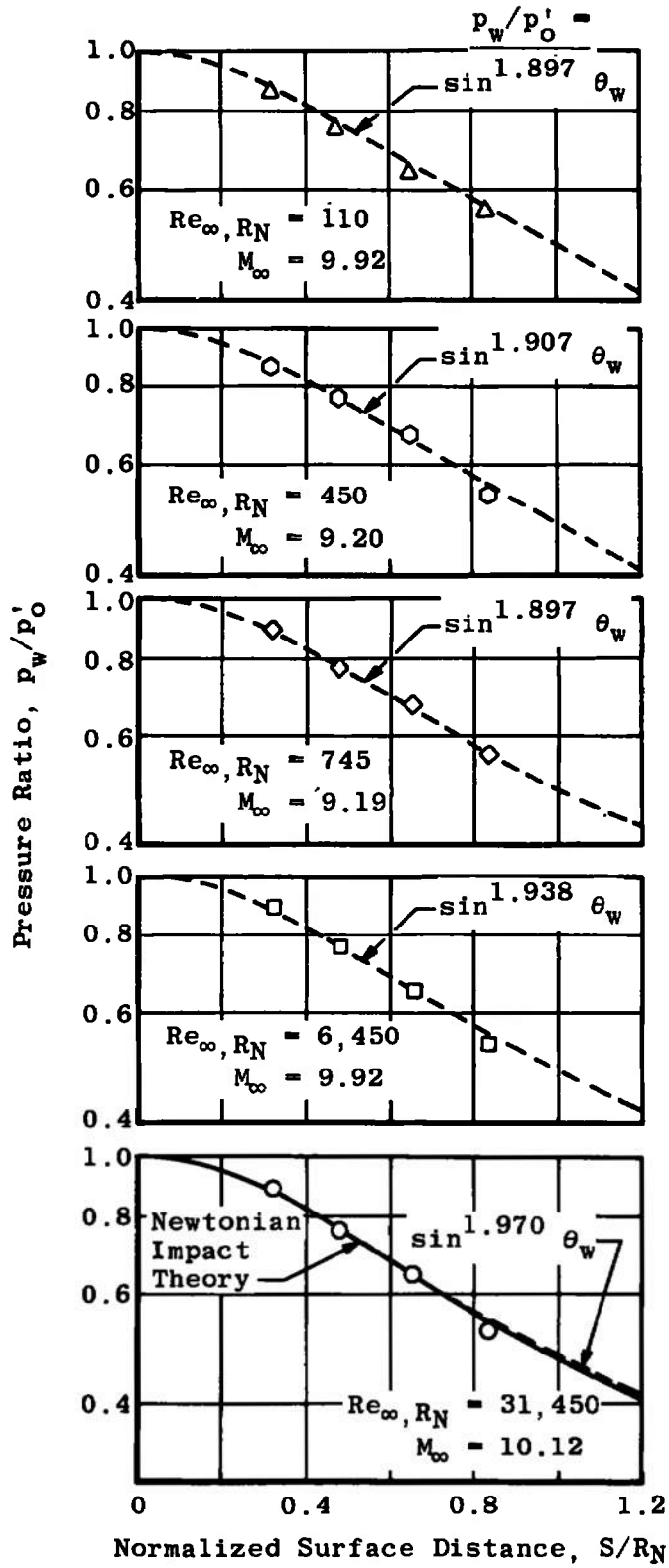

e. H/.25/10/.300

Fig. 25 Continued

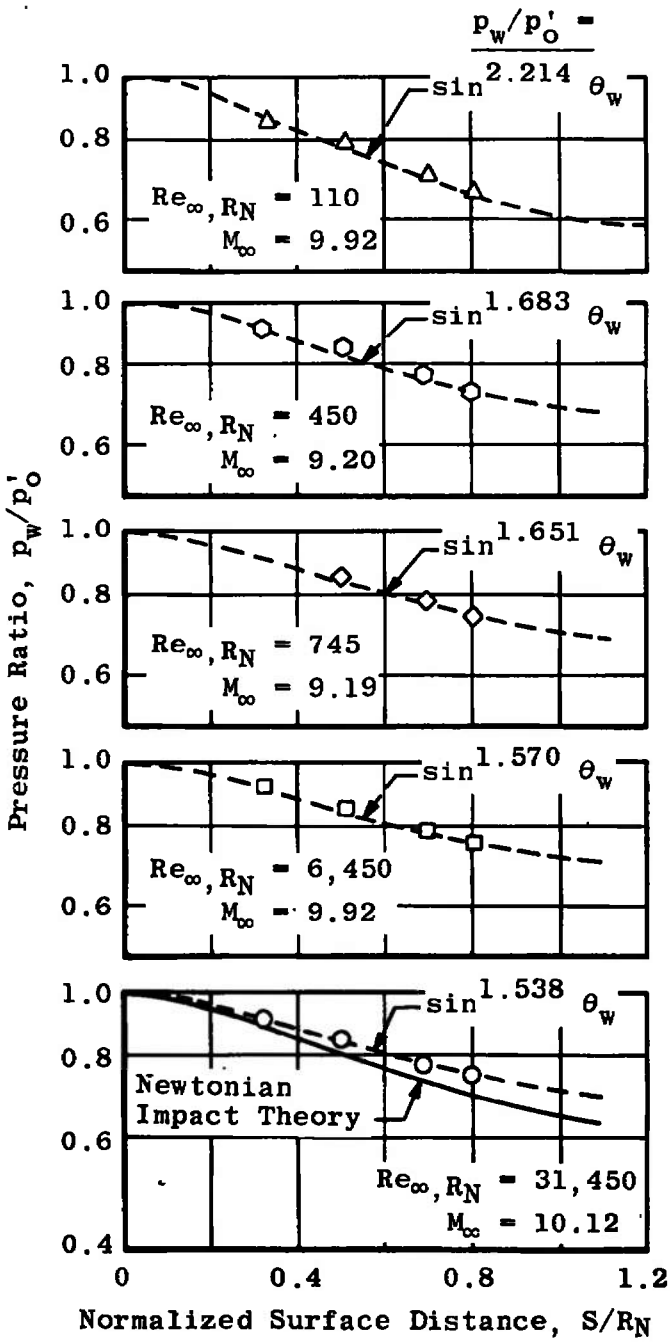

f. H/.25/.45/.300

Fig. 25 Continued

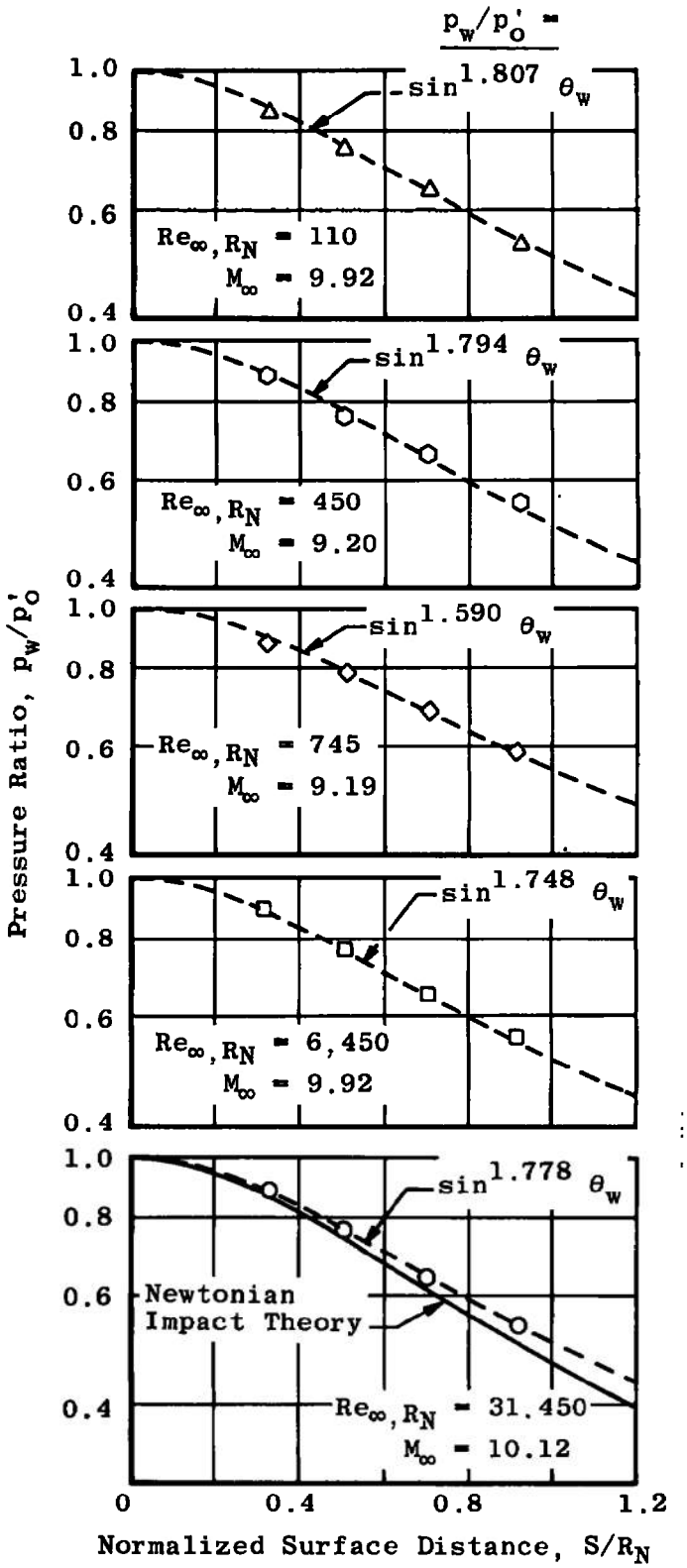

g. P/.25/.300

Fig. 25 Concluded

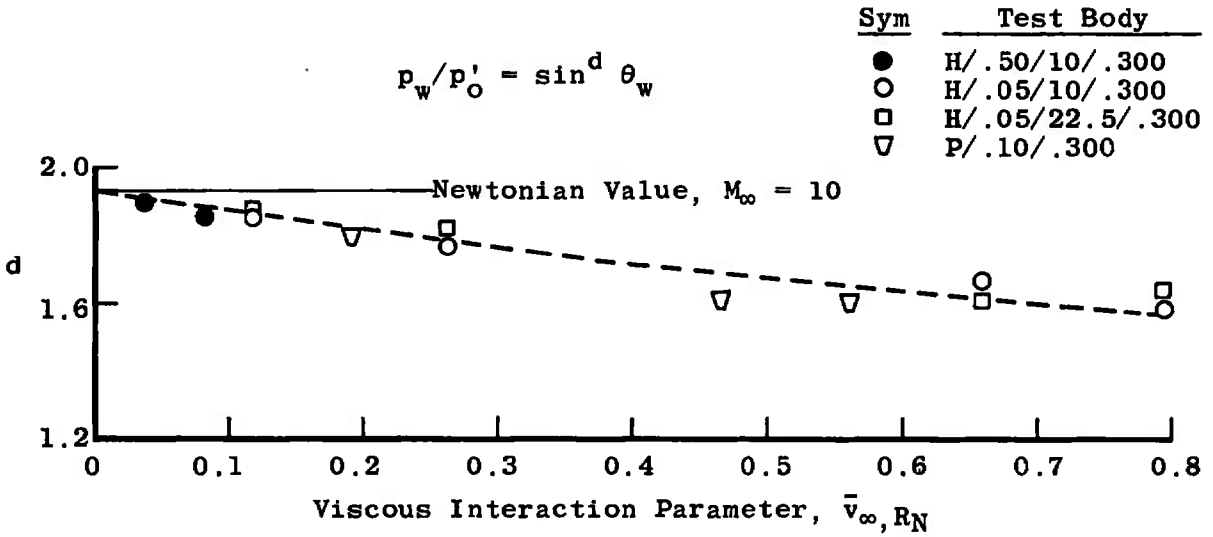

Fig. 26 Effects of Viscous Interaction on Analytic Body Pressure

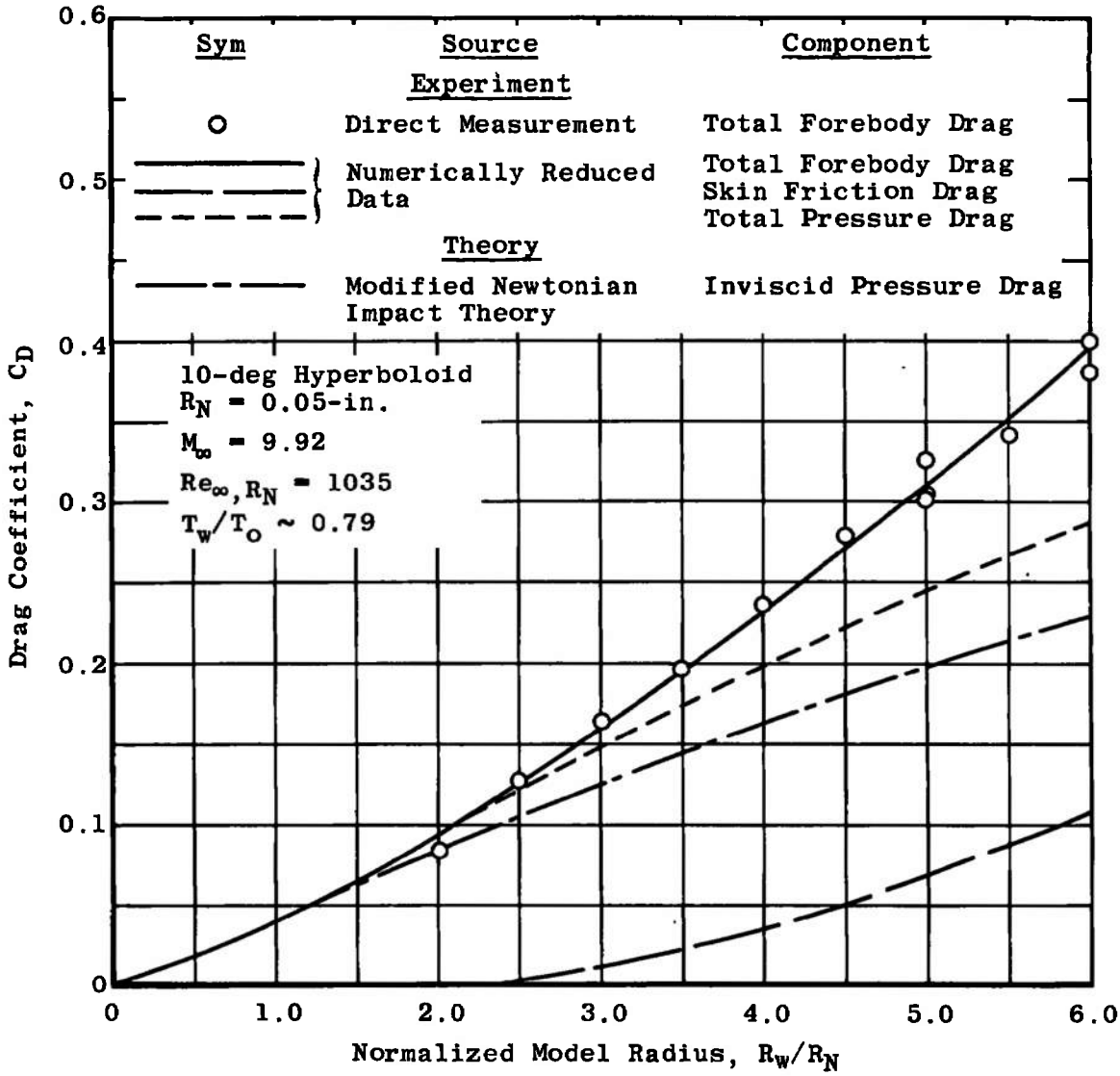

a. Re_{∞,R_N} = 1035

Fig. 27 Drag Distributions on H/.05/10/.300 Model

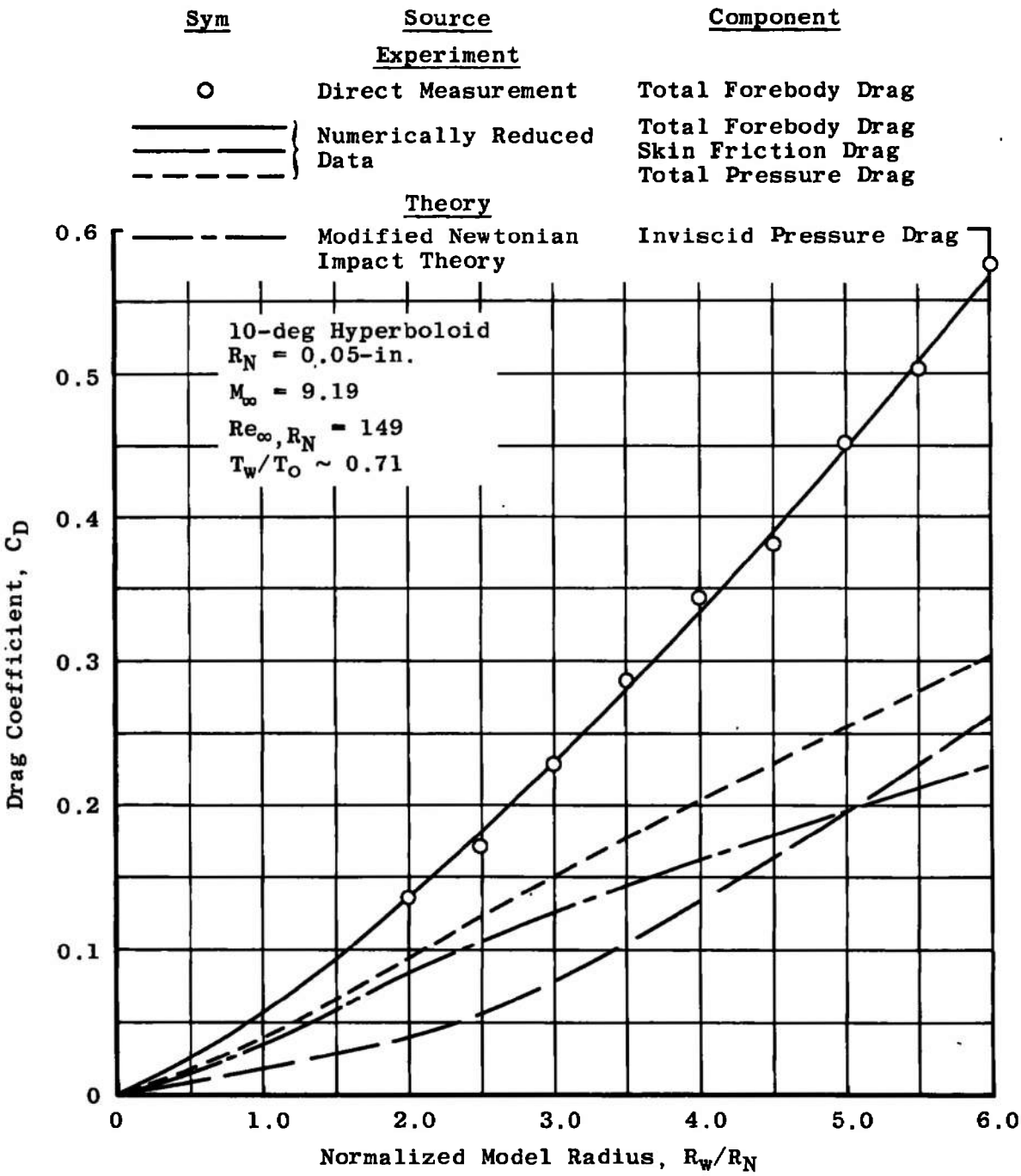

b. Re_{∞,R_N} = 149

Fig. 27 Continued

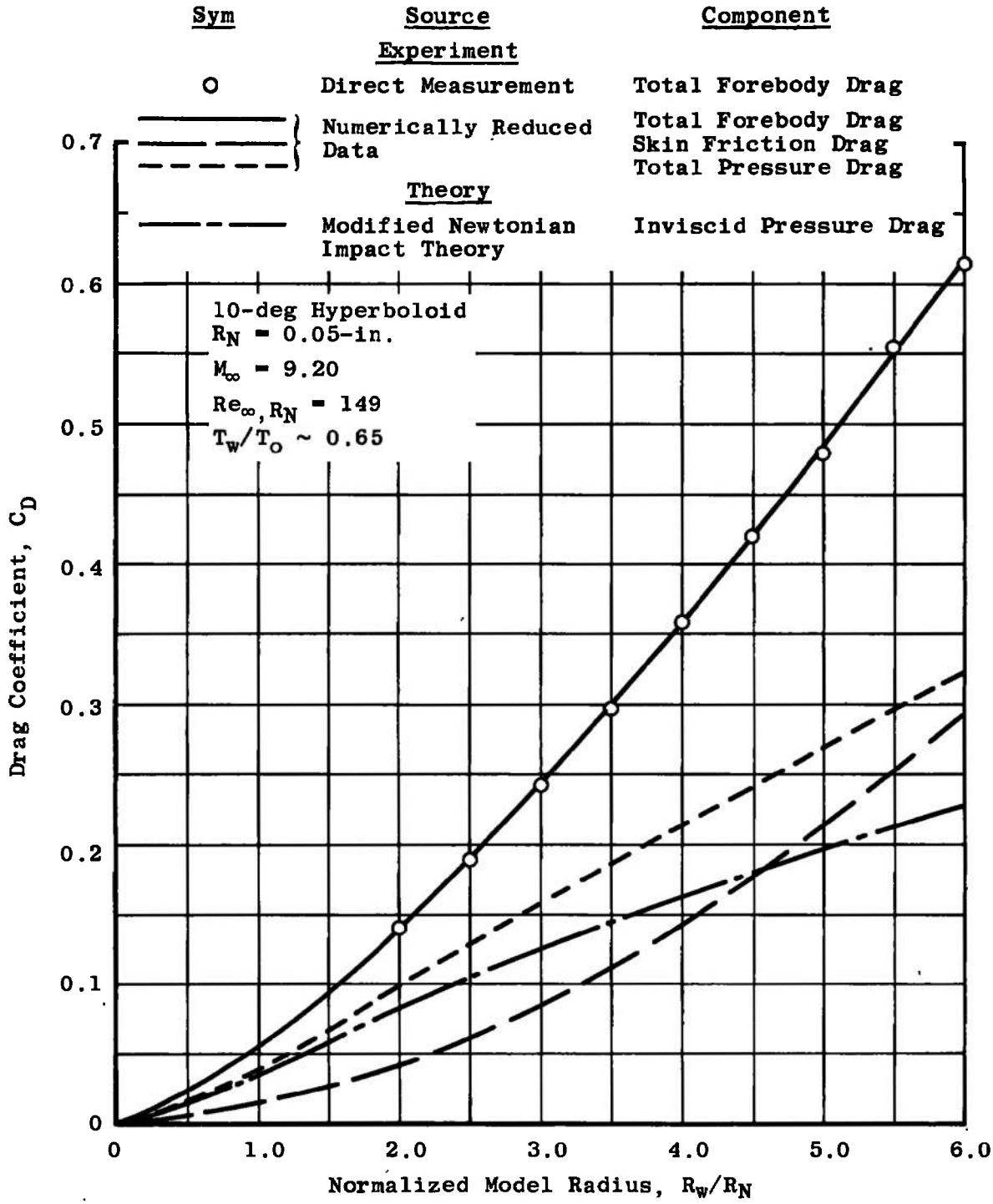

c. Re_{∞,R_N} = 90

Fig. 27 Continued

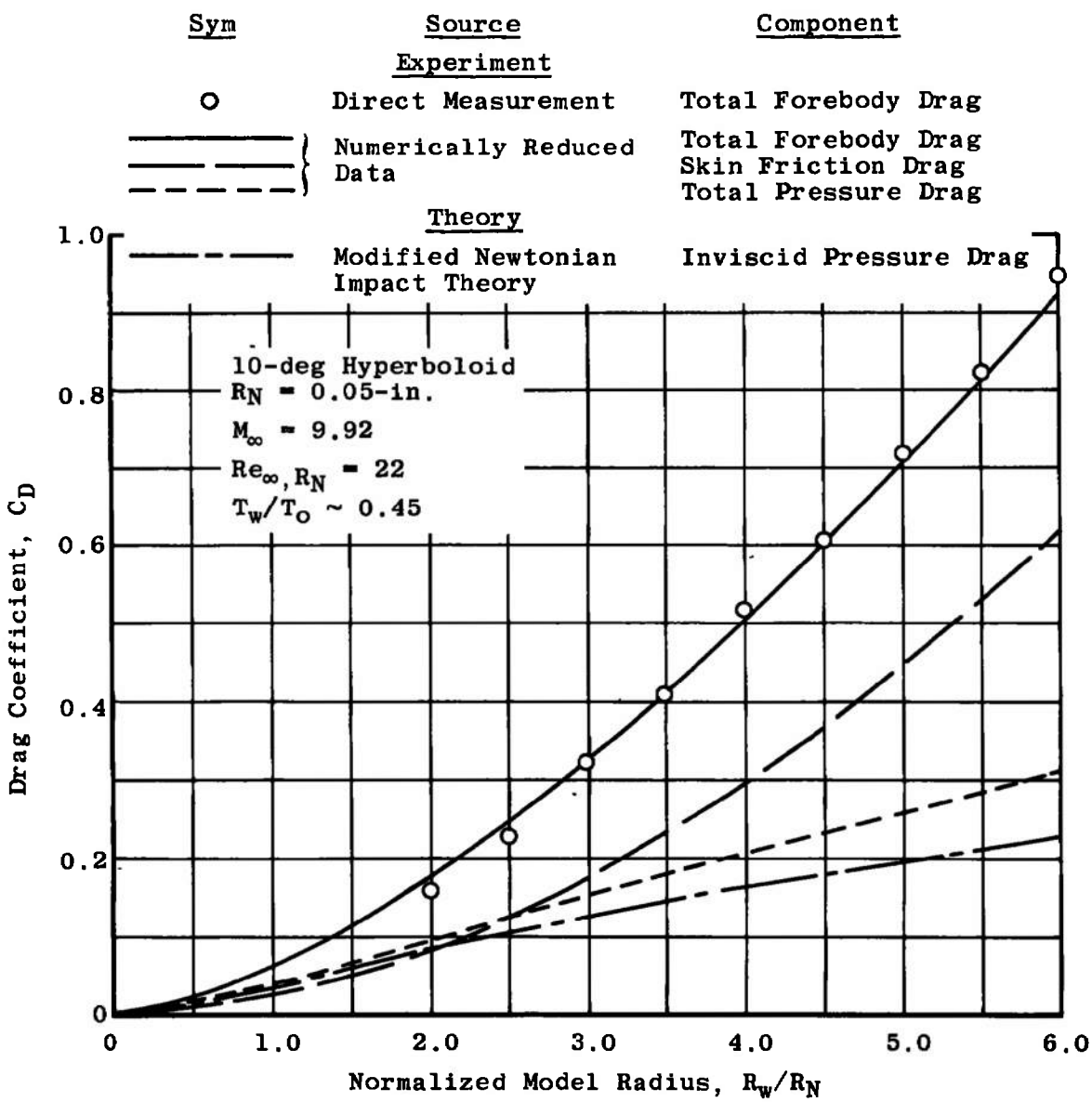

d. Re_{∞, R_N} = 22

Fig. 27 Concluded

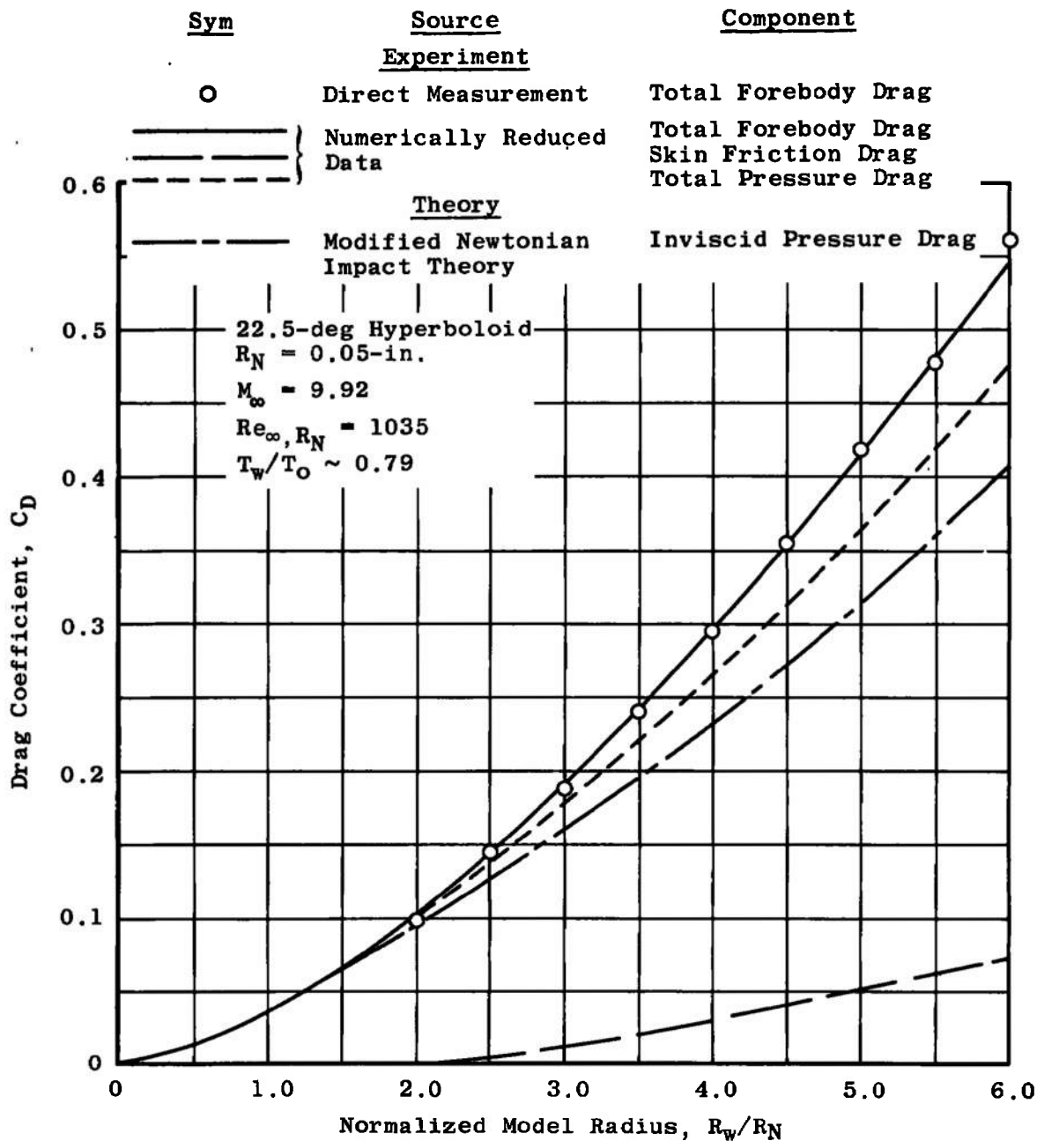

a. Re_{∞,R_N} = 1035

Fig. 28 Drag Distributions on H/.05/22.5/.300 Model

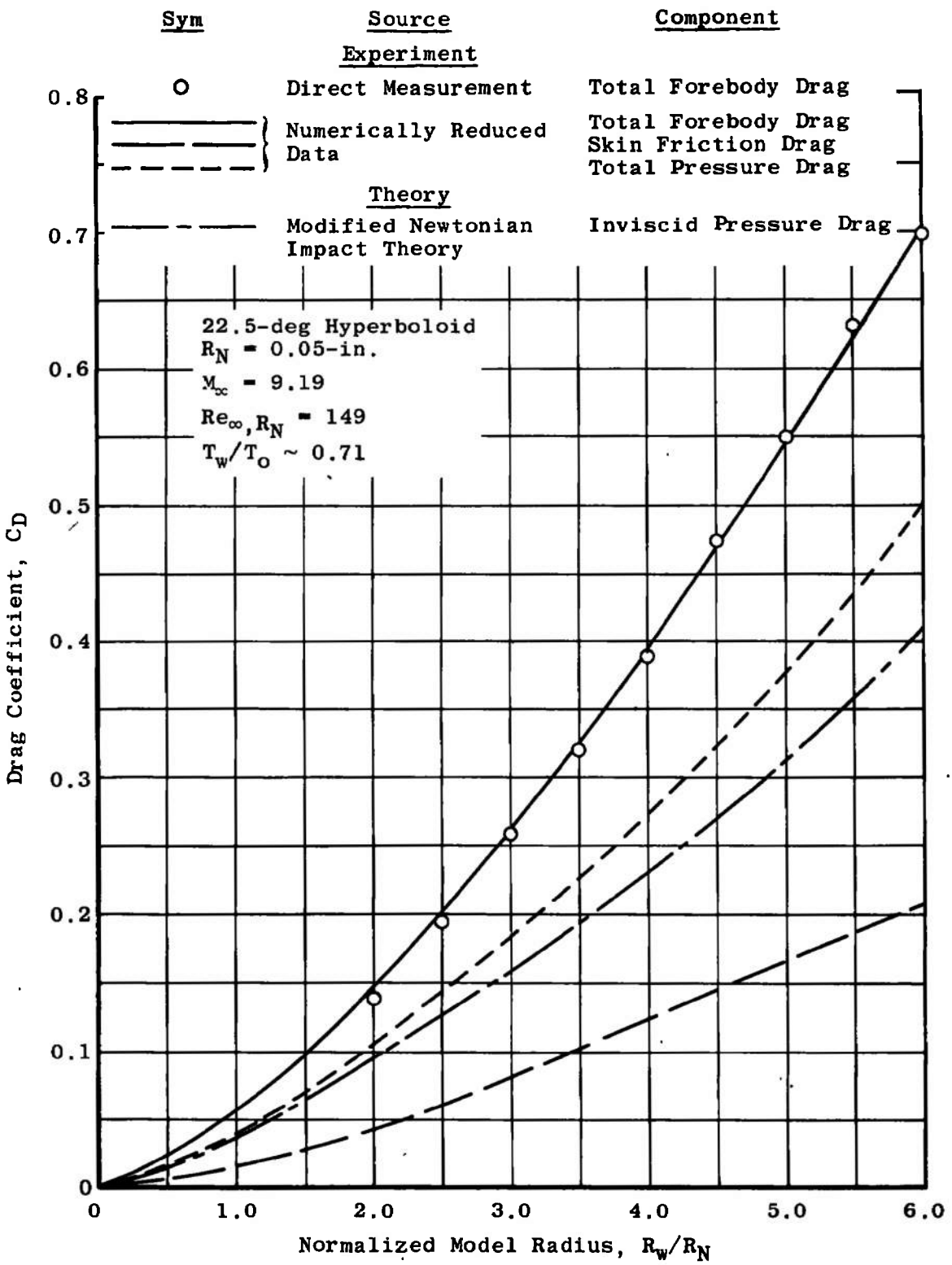

b. Re_{∞, R_N} = 149

Fig. 28 Continued

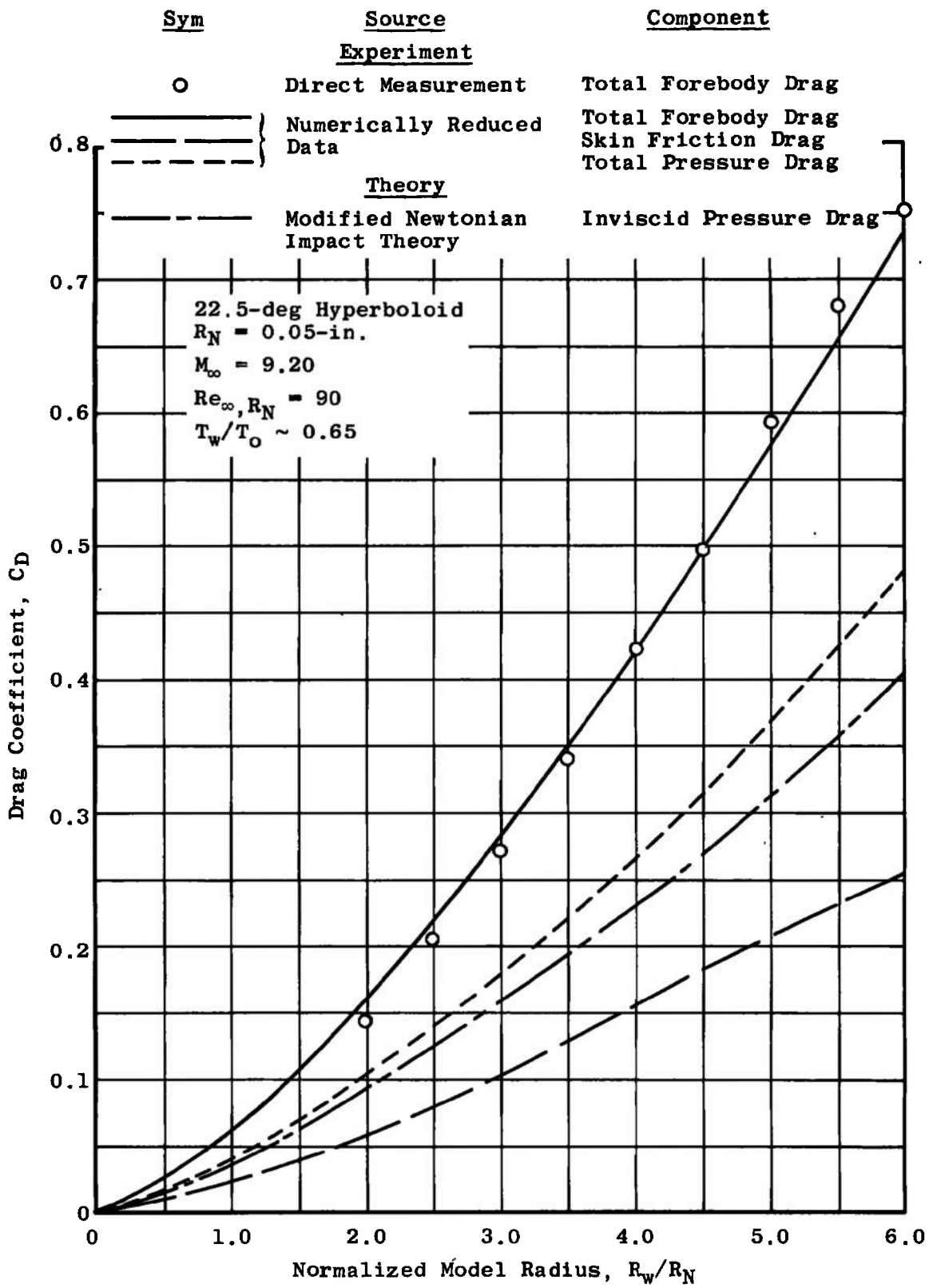

c. Re_{∞, R_N} = 90

Fig. 28 Continued

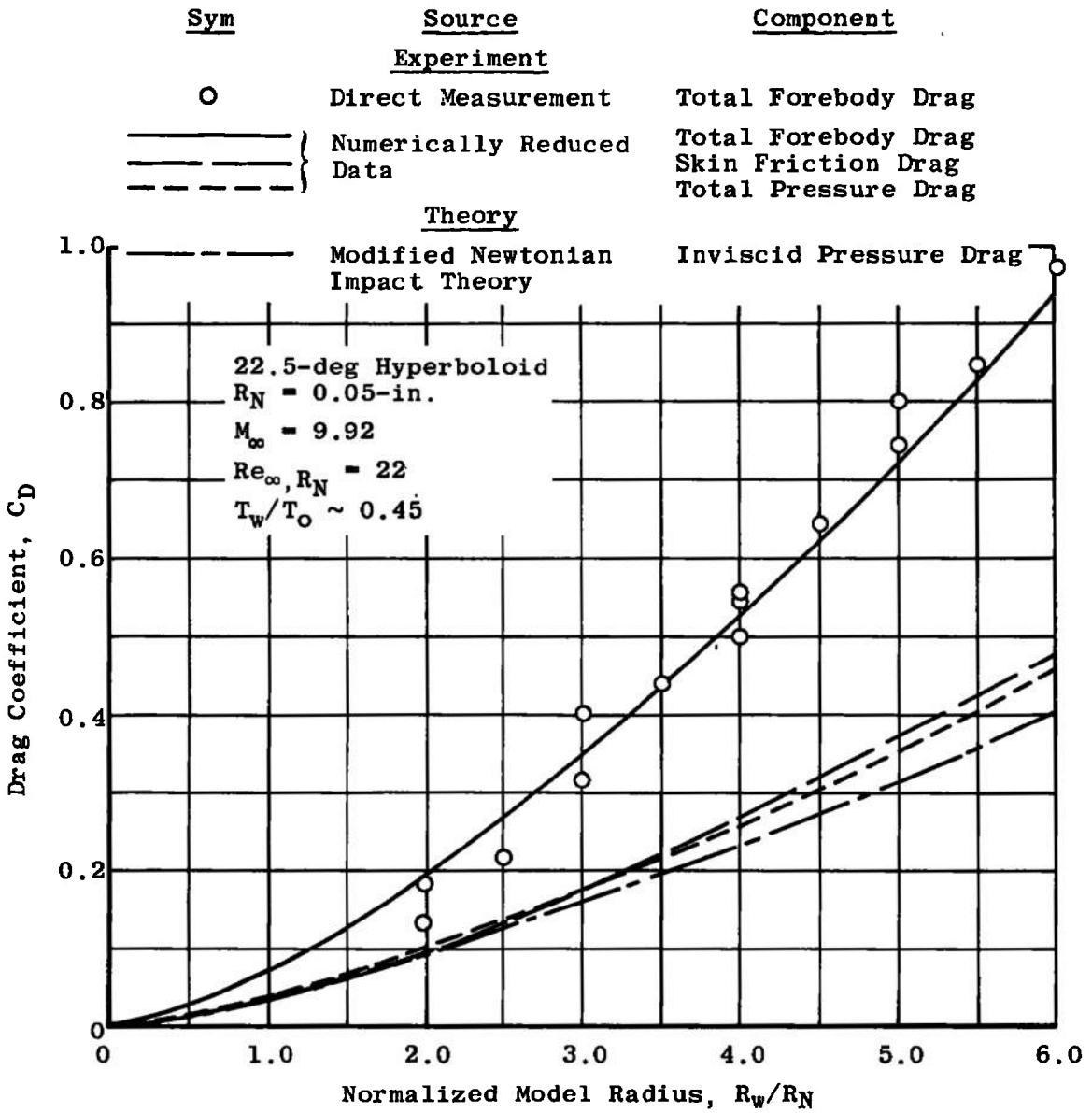

d. Re_{∞, R_N} = 22

Fig. 28 Concluded

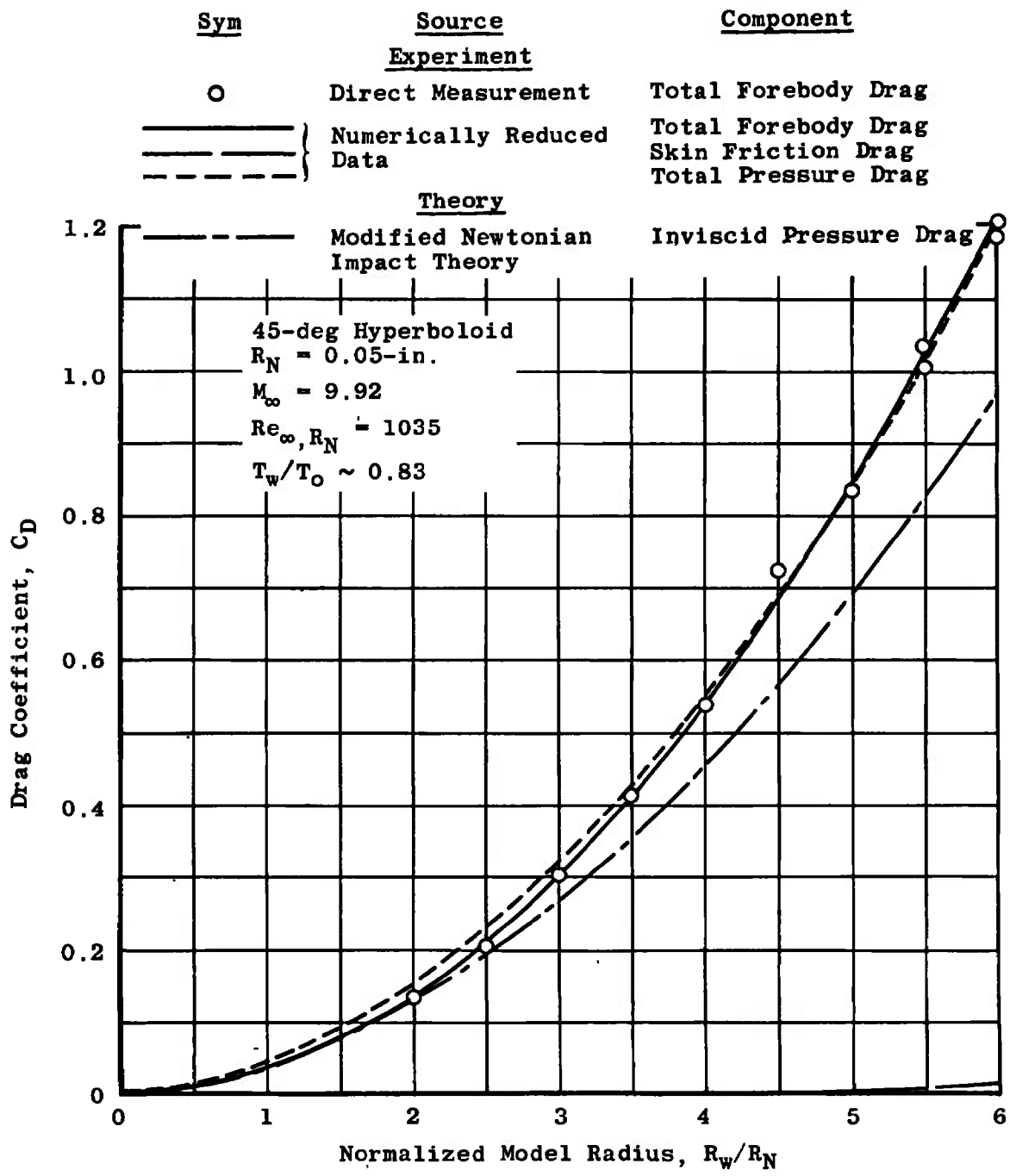

a. Re_{∞, R_N} = 1035

Fig. 29 Drag Distributions on H/.05/45/.300 Model

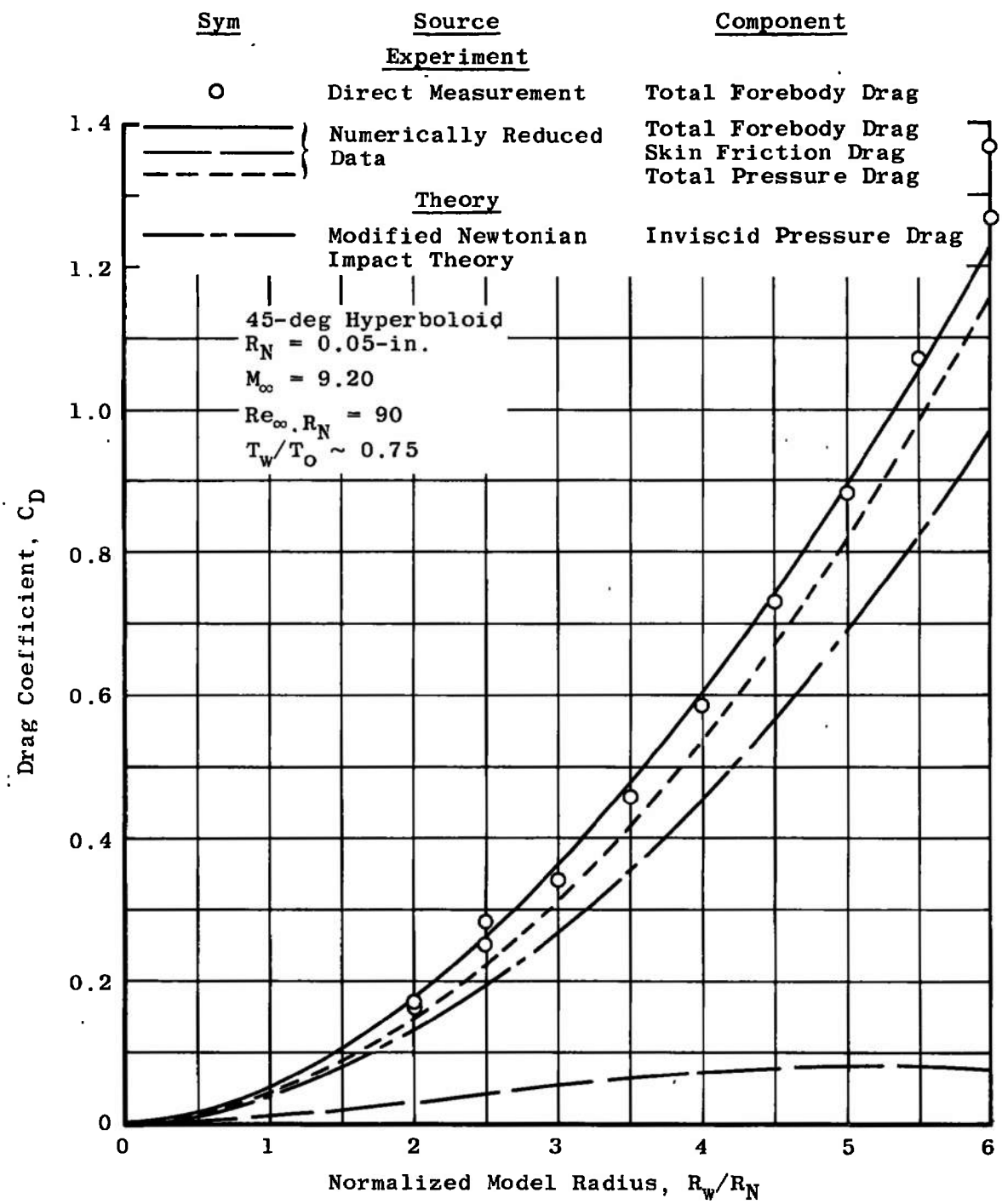

b. Re_{∞, R_N} = 90

Fig. 29 Continued

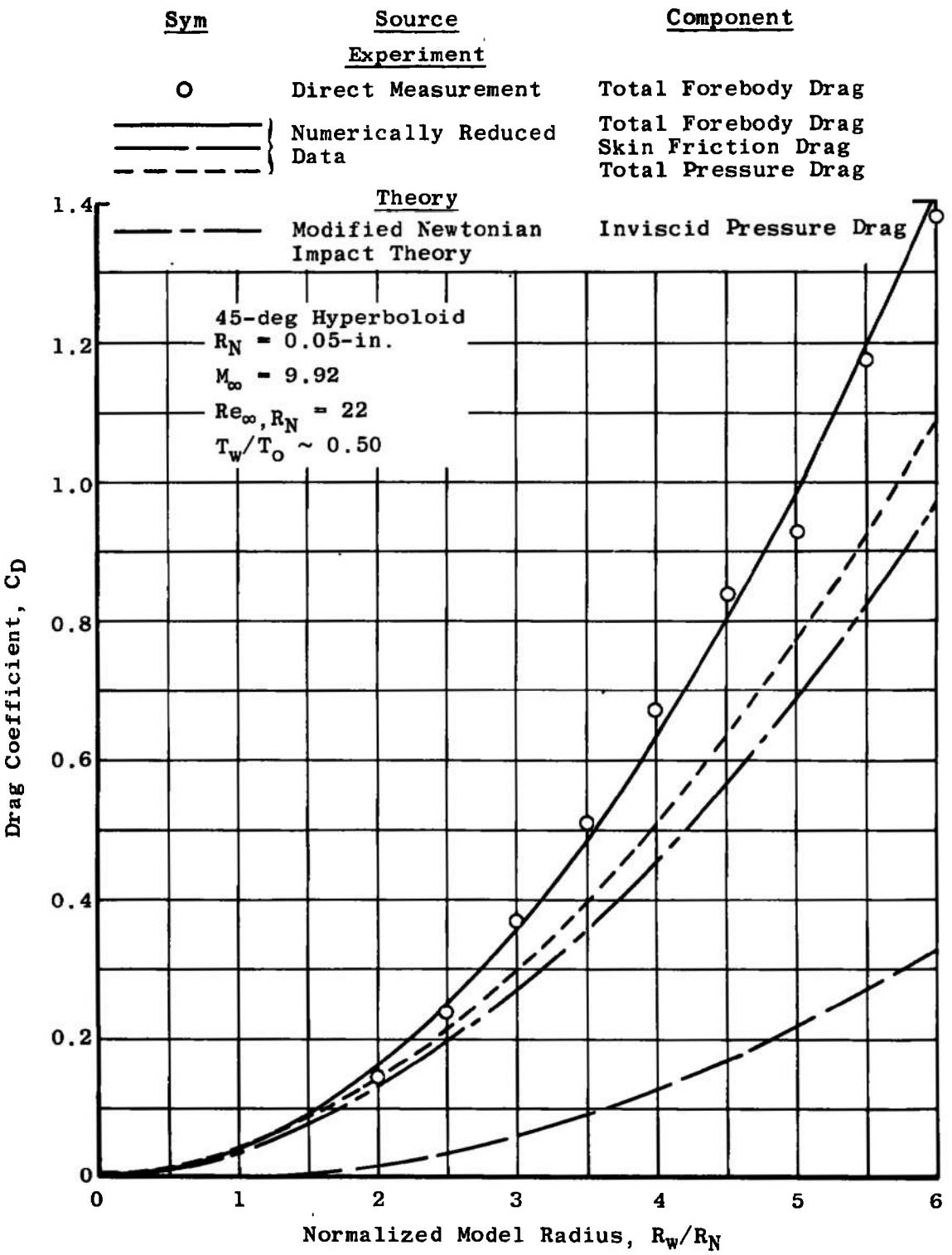

c. Re_{∞, R_N} = 22

Fig. 29 Concluded

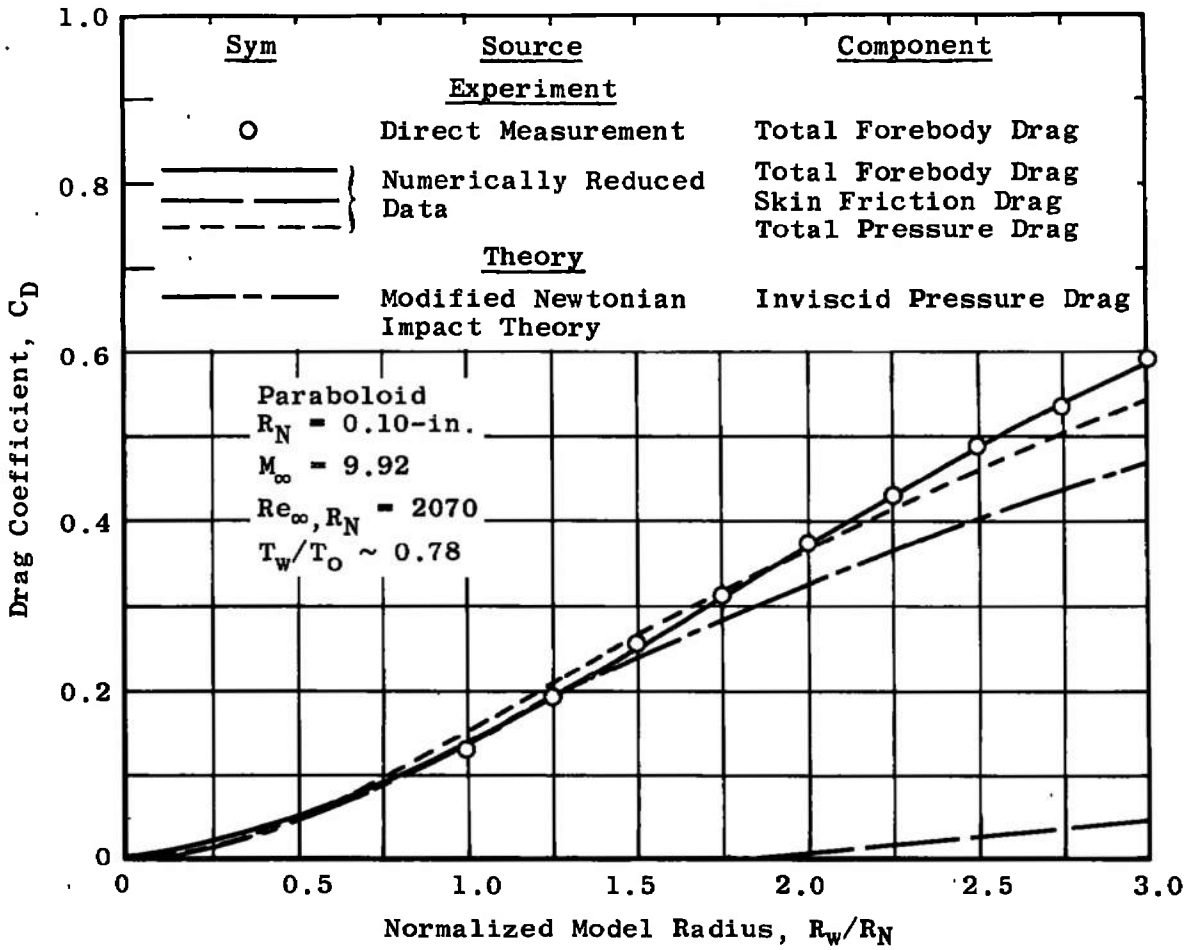

a. Re_{∞, R_N} = 2070

Fig. 30 Drag Distributions on P/.10/.300 Model

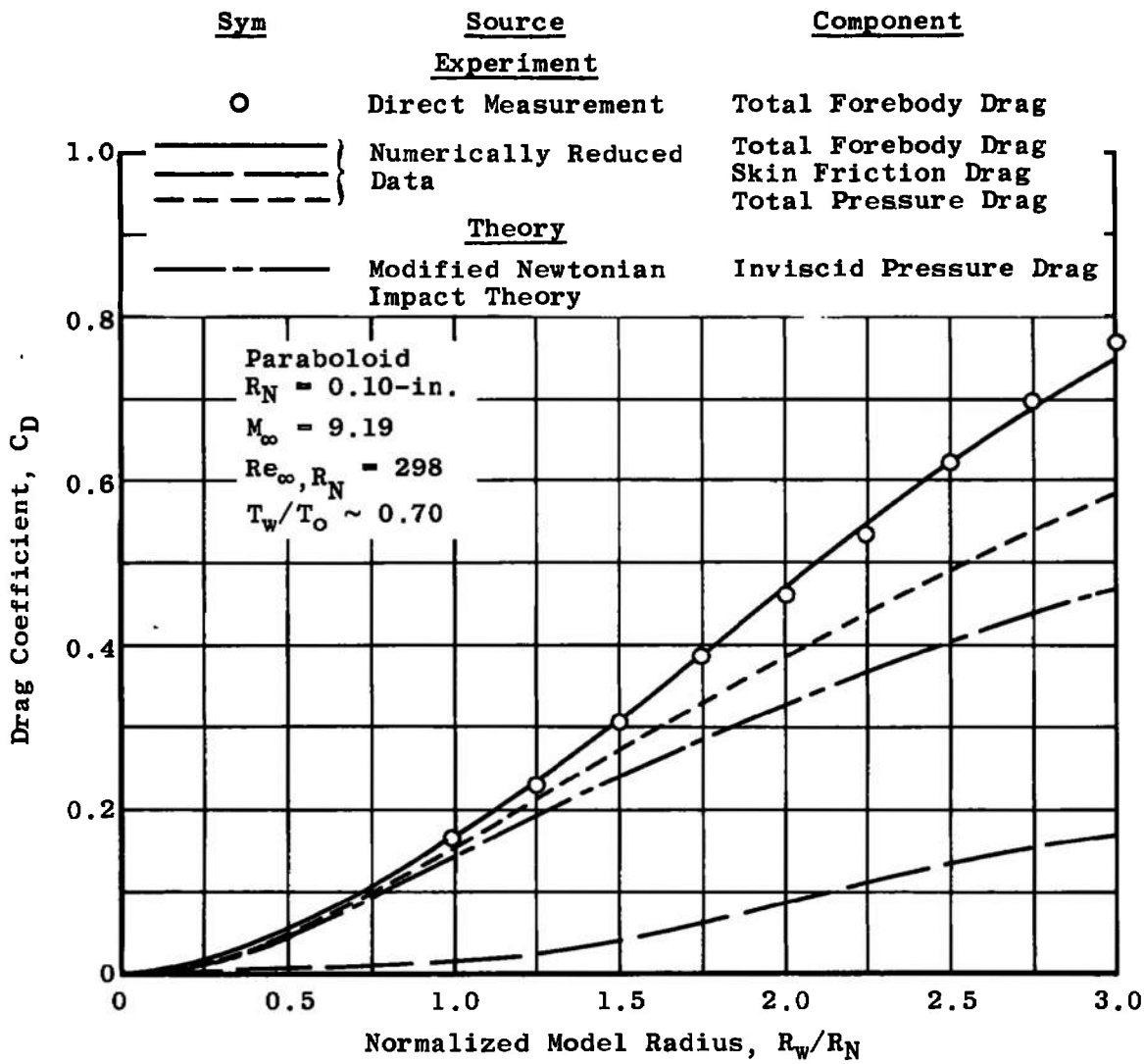

b. Re_{∞, R_N} = 298

Fig. 30 Continued

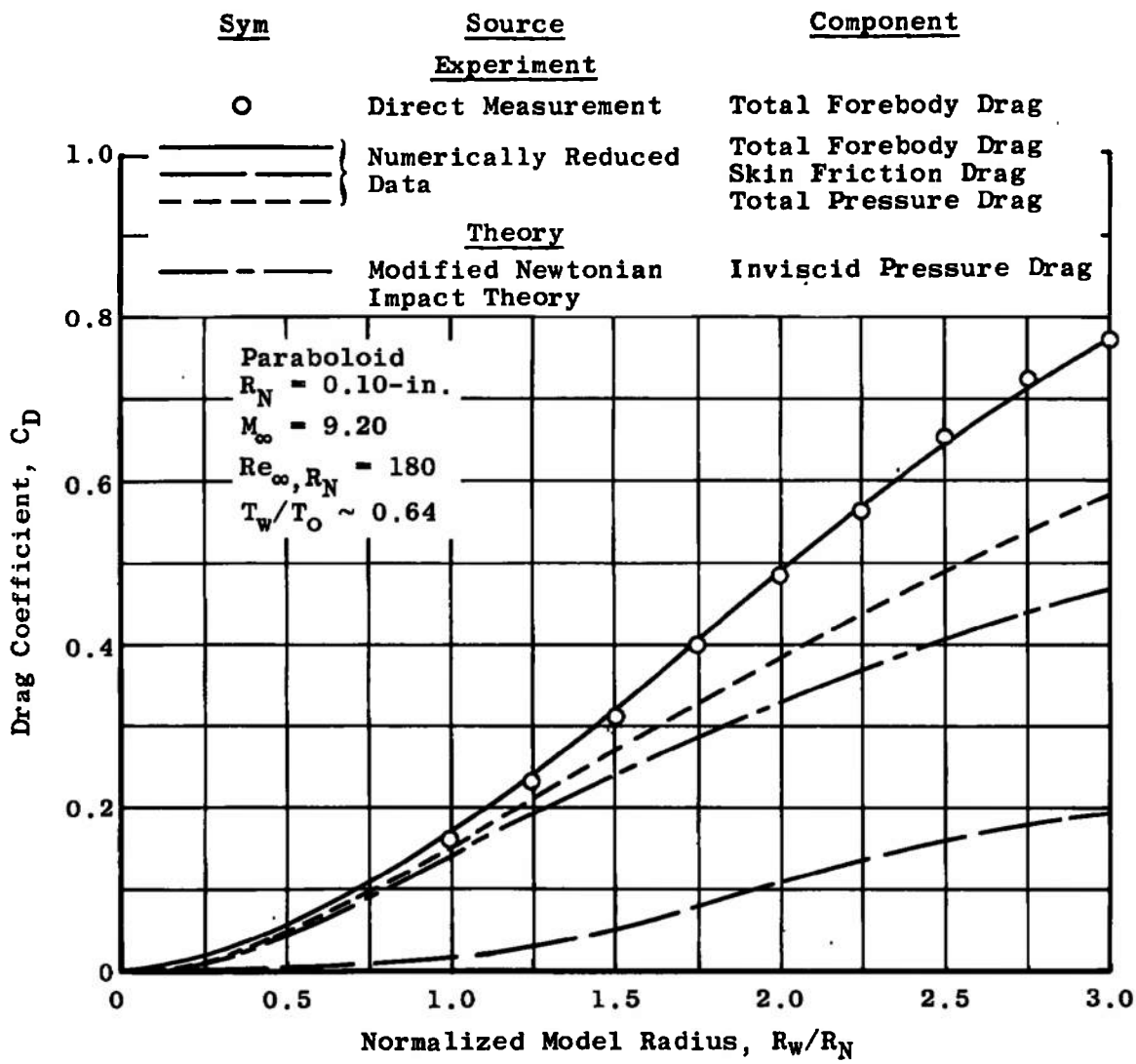

c. Re_{∞, R_N} = 180

Fig. 30 Continued

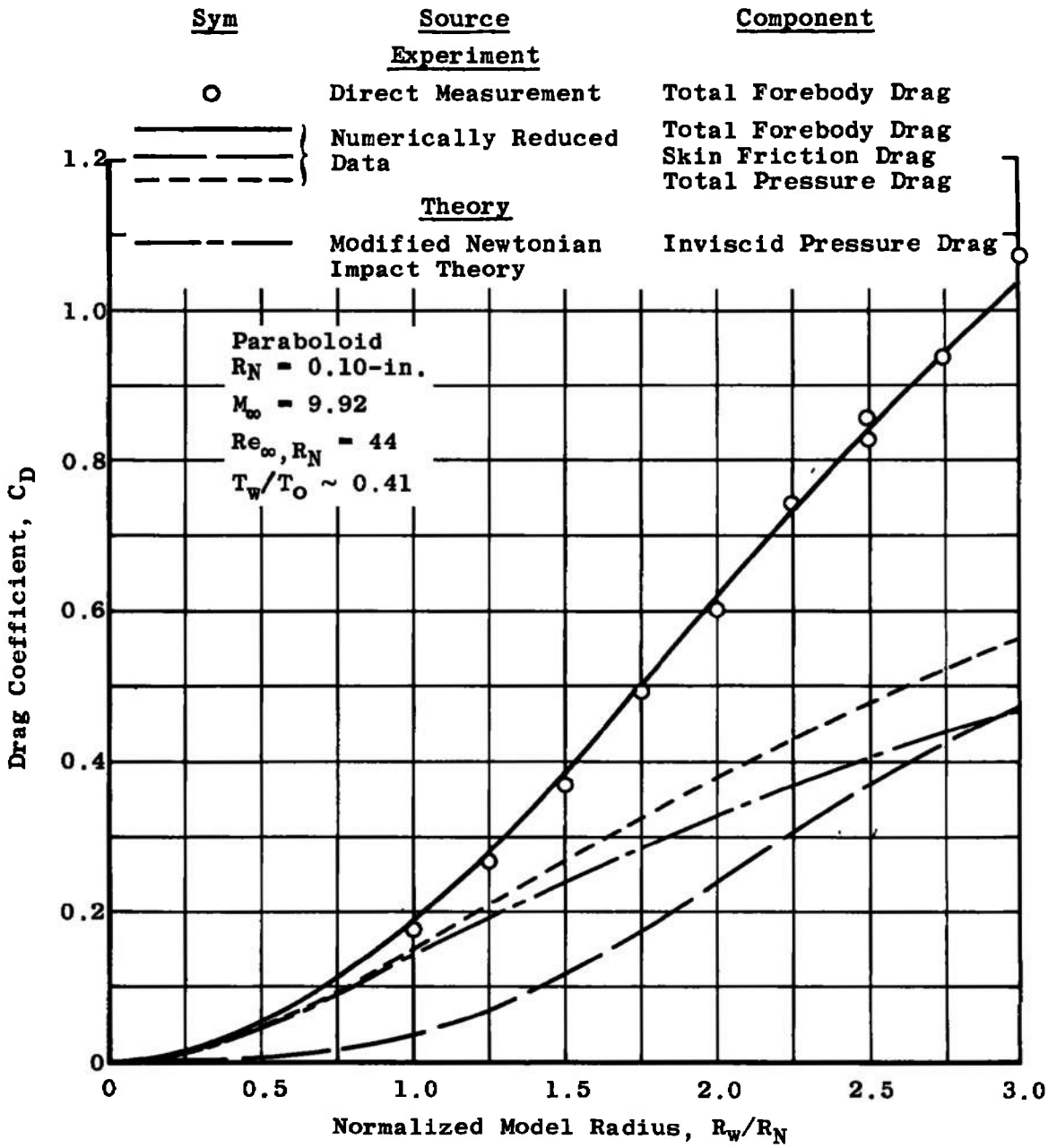

d. Re_{∞, R_N} = 44

Fig. 30 Concluded

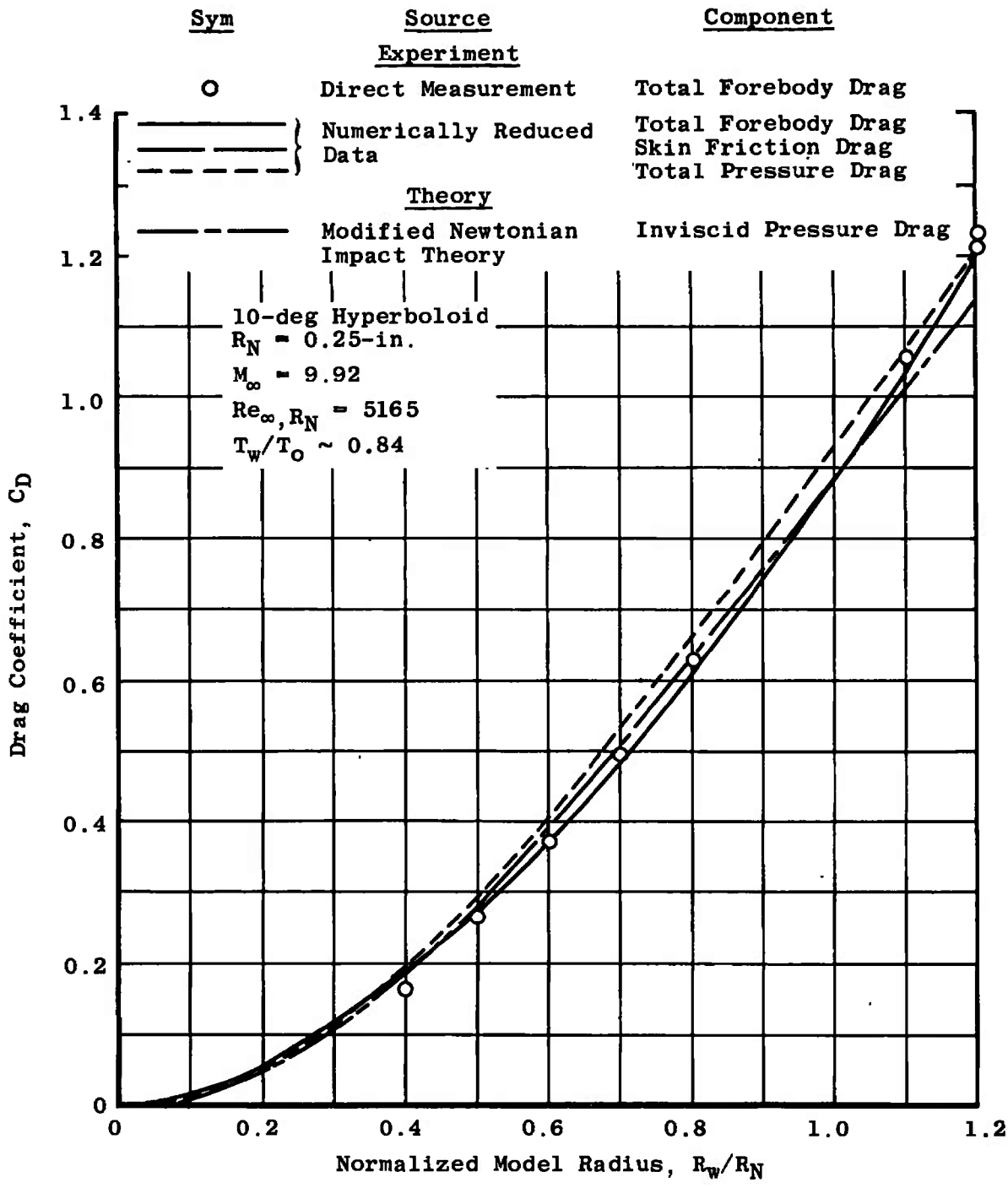

a. Re_{∞, R_N} = 5165

Fig. 31 Drag Distributions on H/.25/10/.300 Model

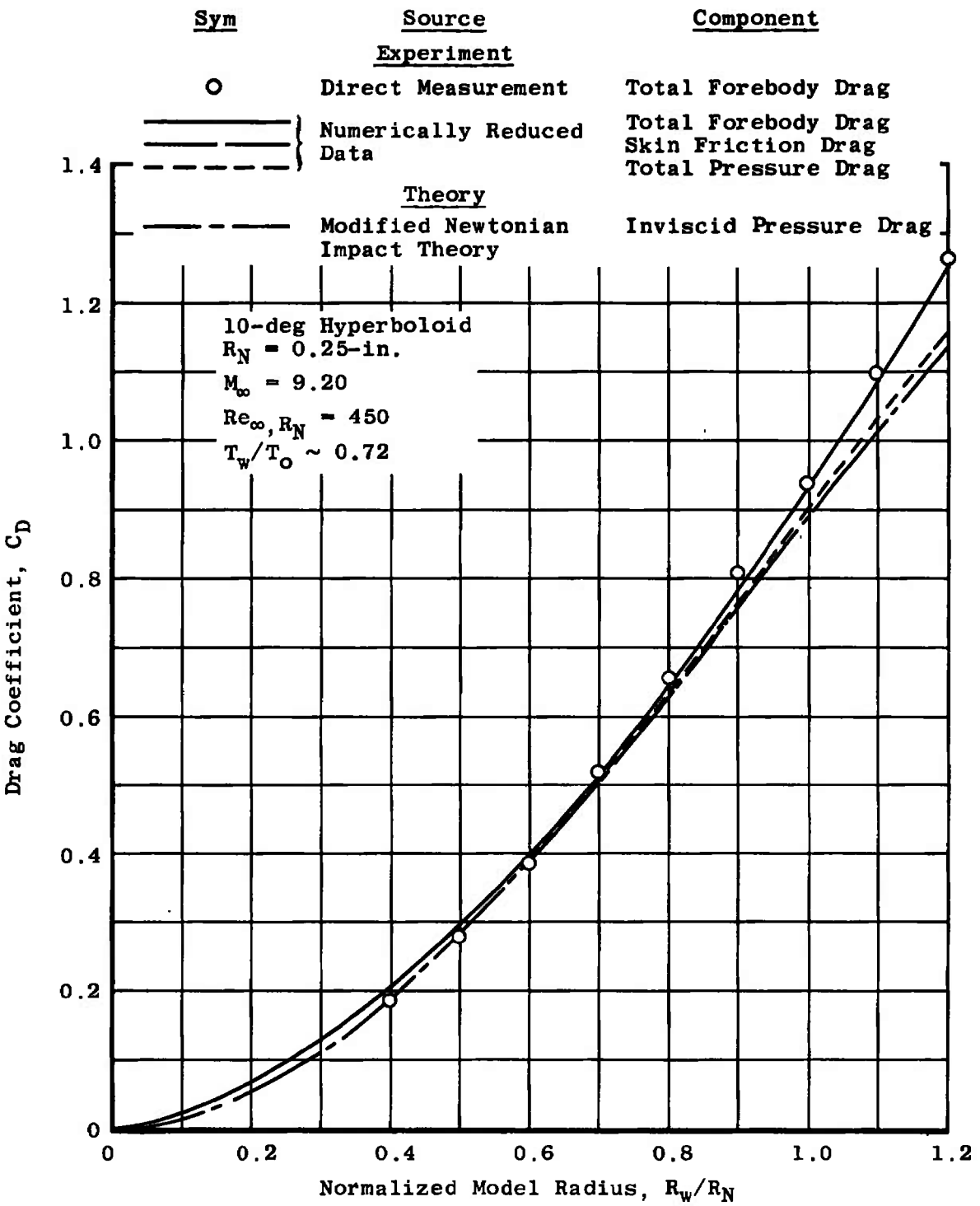

b. Re_{∞, R_N} = 450

Fig. 31 Continued

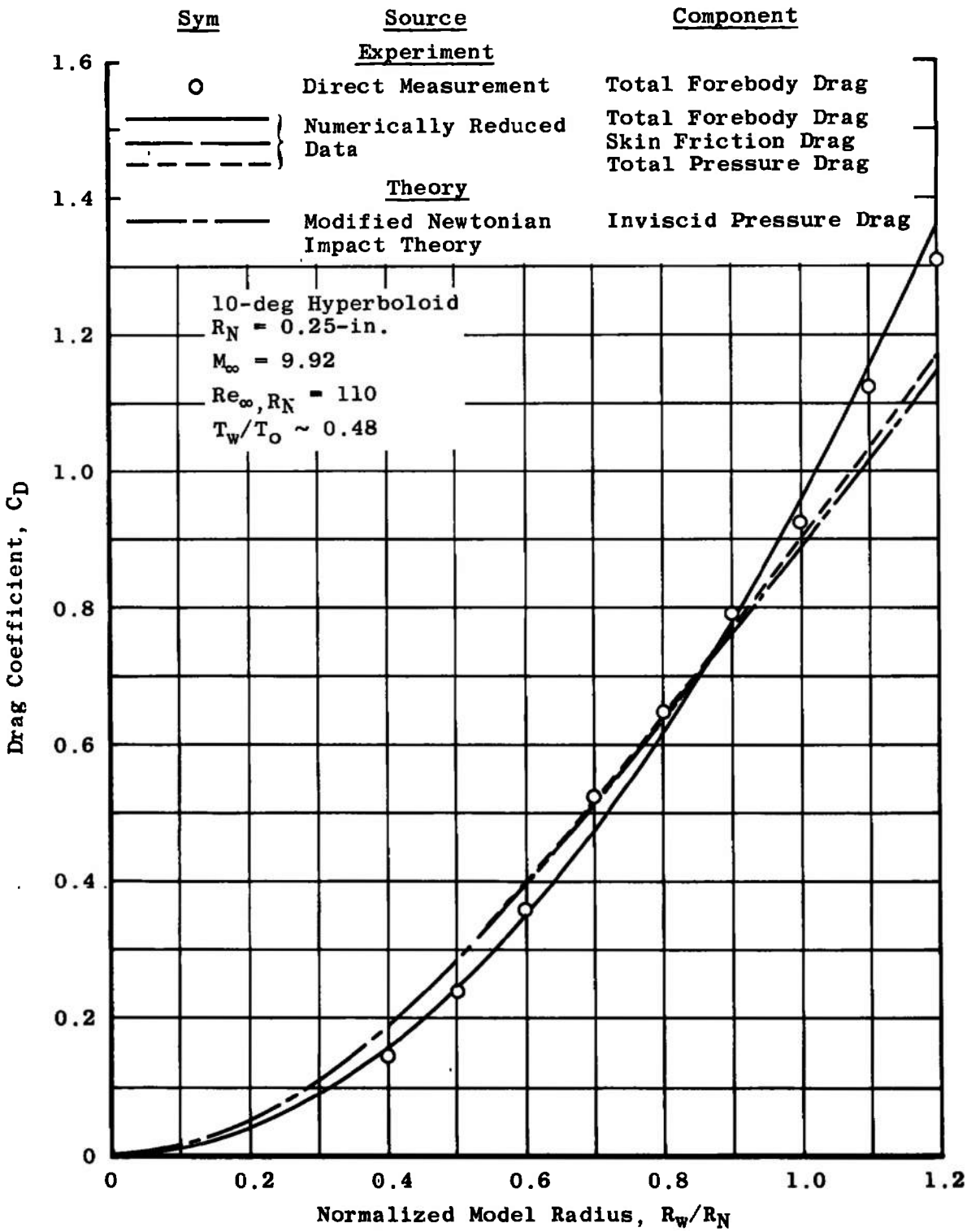

c. Re_{∞, R_N} = 110

Fig. 31 Concluded

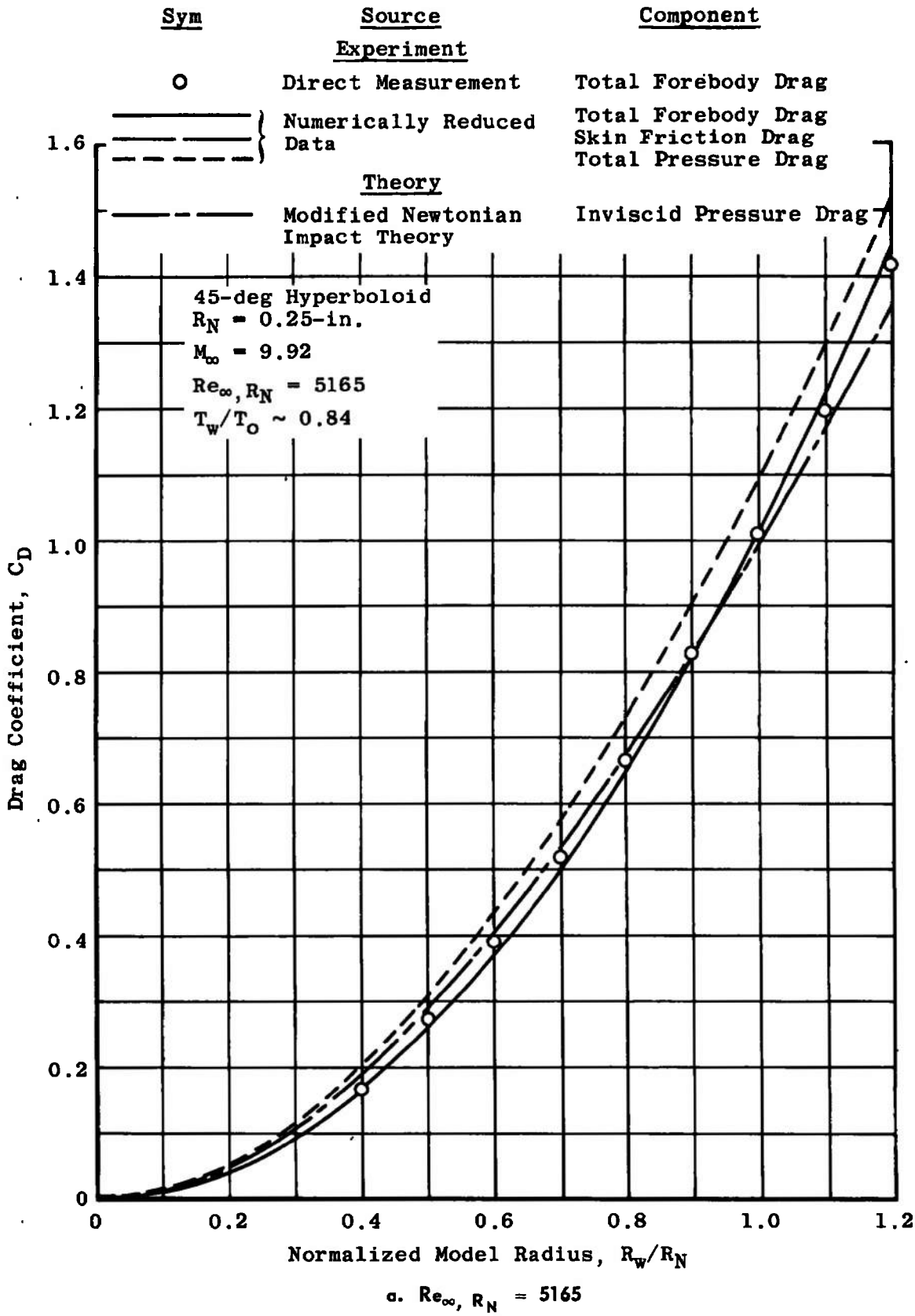

a. Re_{∞, R_N} = 5165

Fig. 32 Drag Distributions on H/.25/45/.300 Model

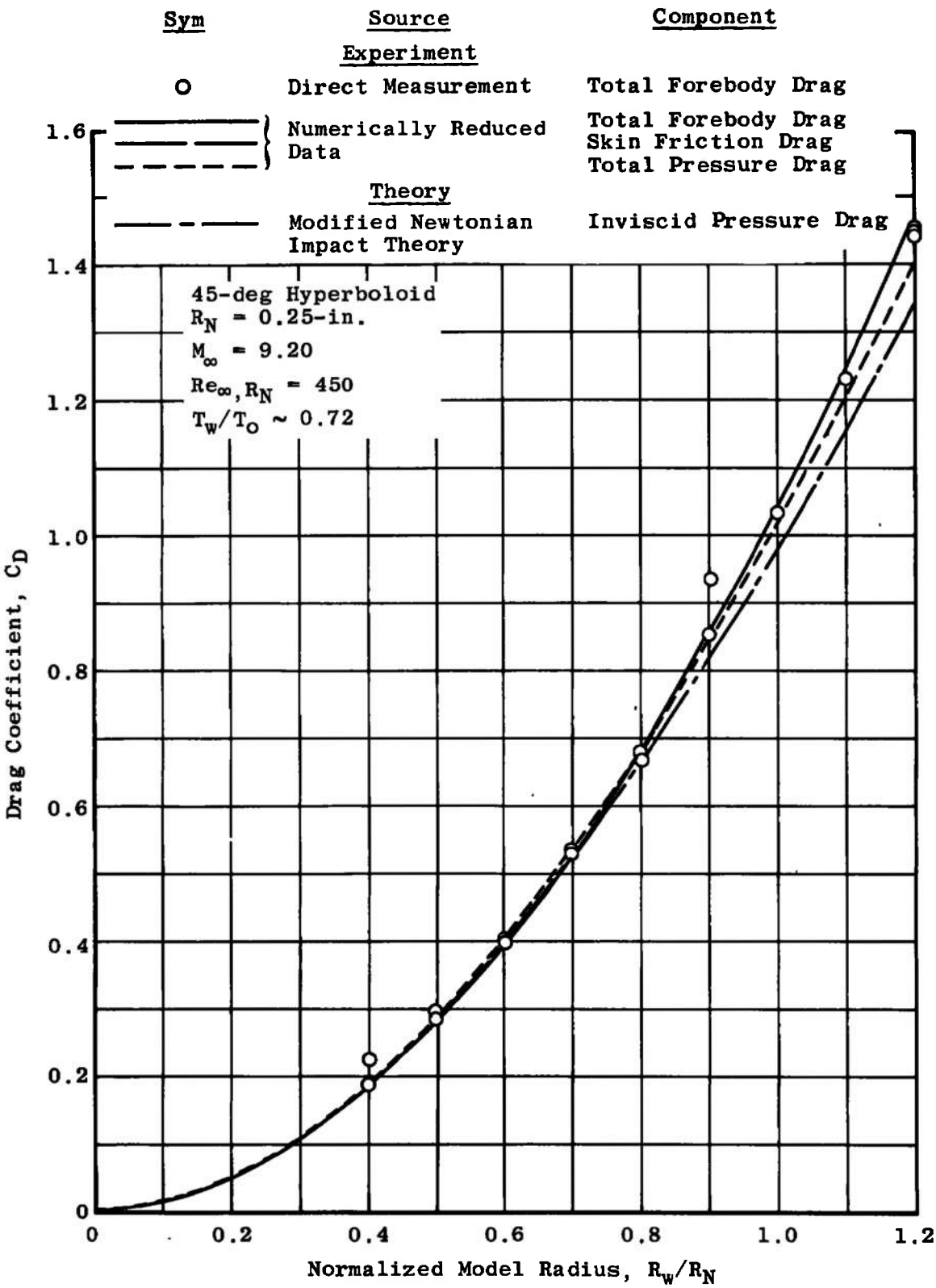

b. Re_{∞, R_N} = 450

Fig. 32 Continued

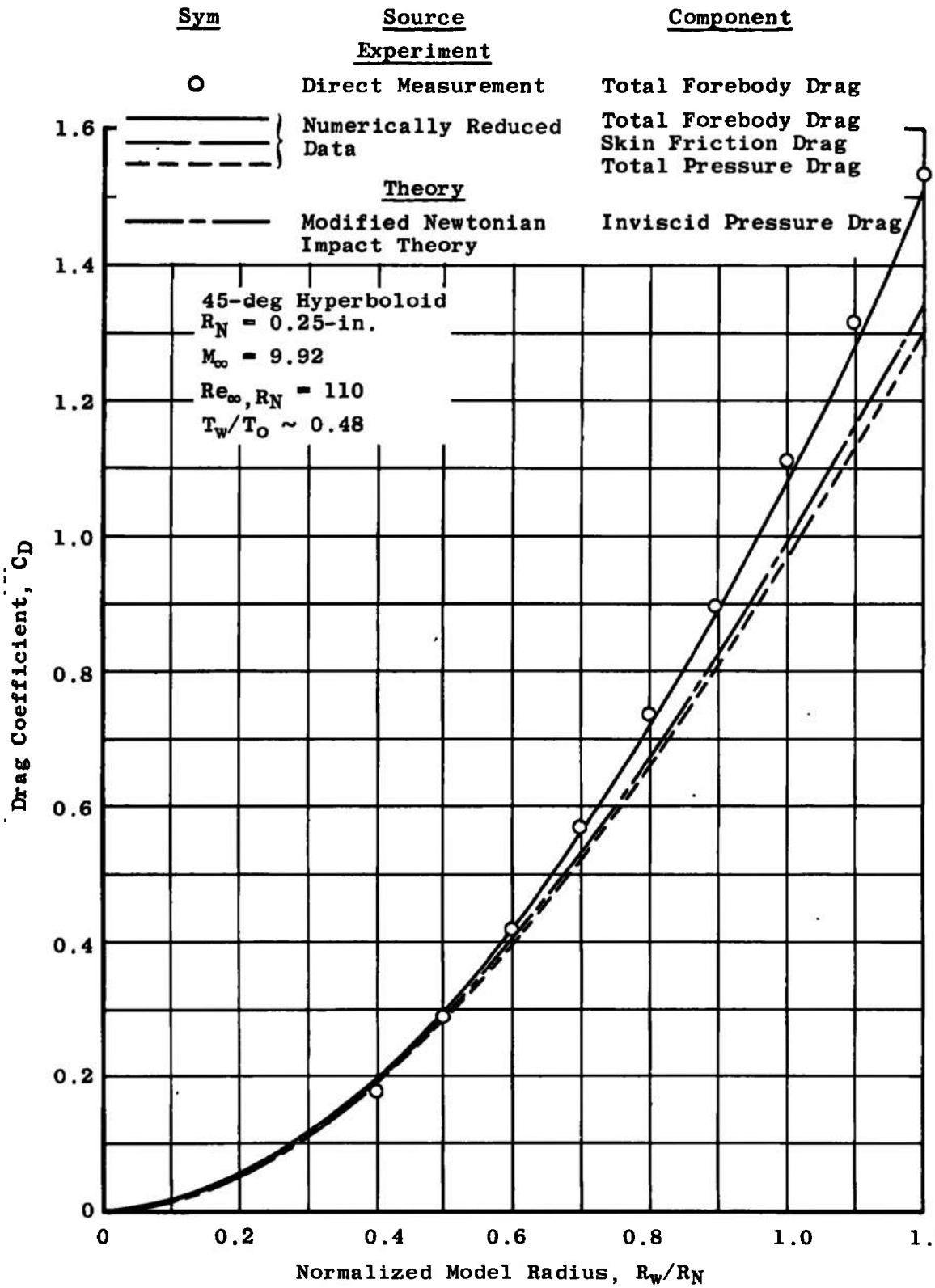

c. Re_{∞, R_N} = 110

Fig. 32 Concluded

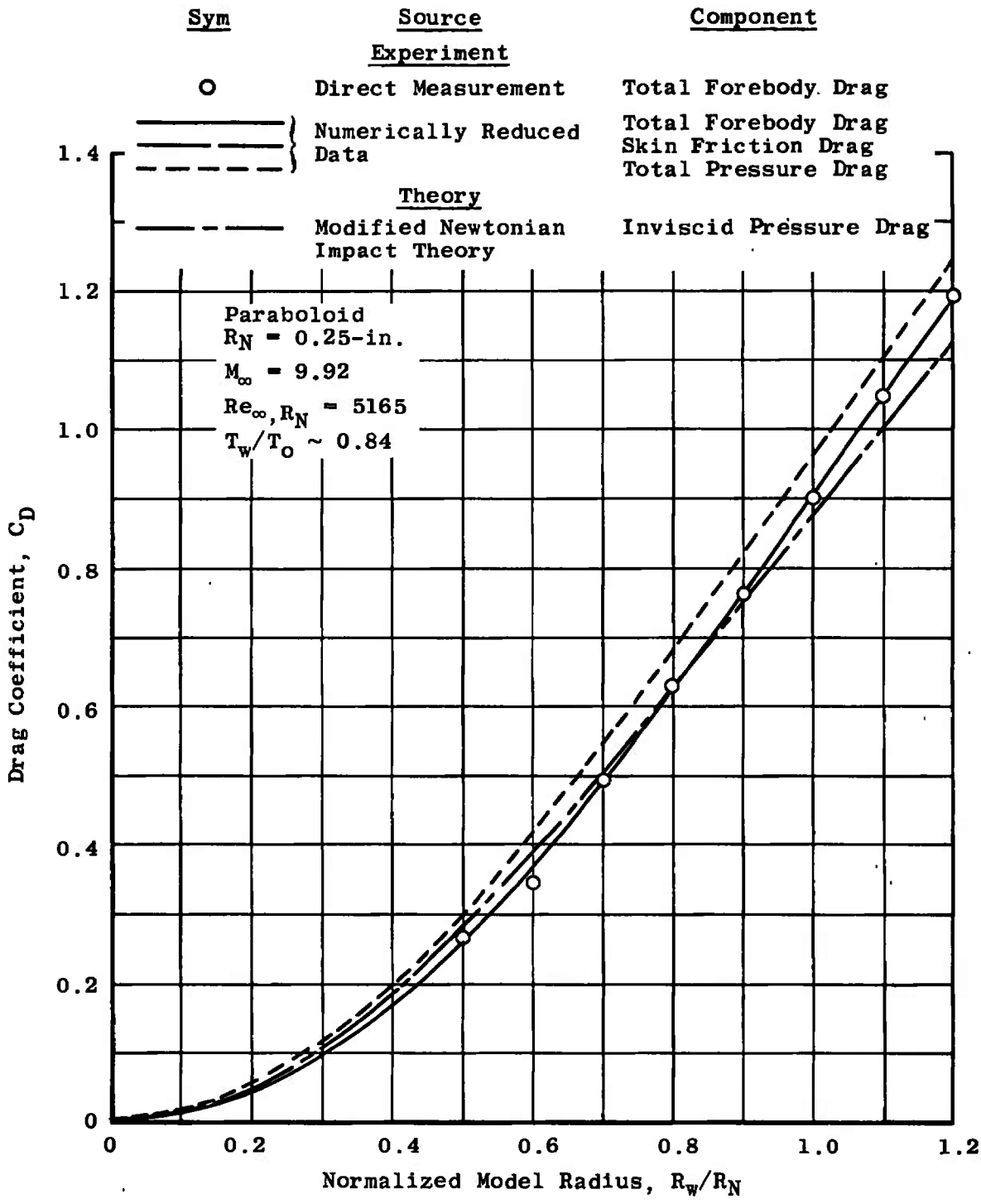

a. Re_{∞, R_N} = 5165

Fig. 33 Drag Distributions on P/.25/.300 Model

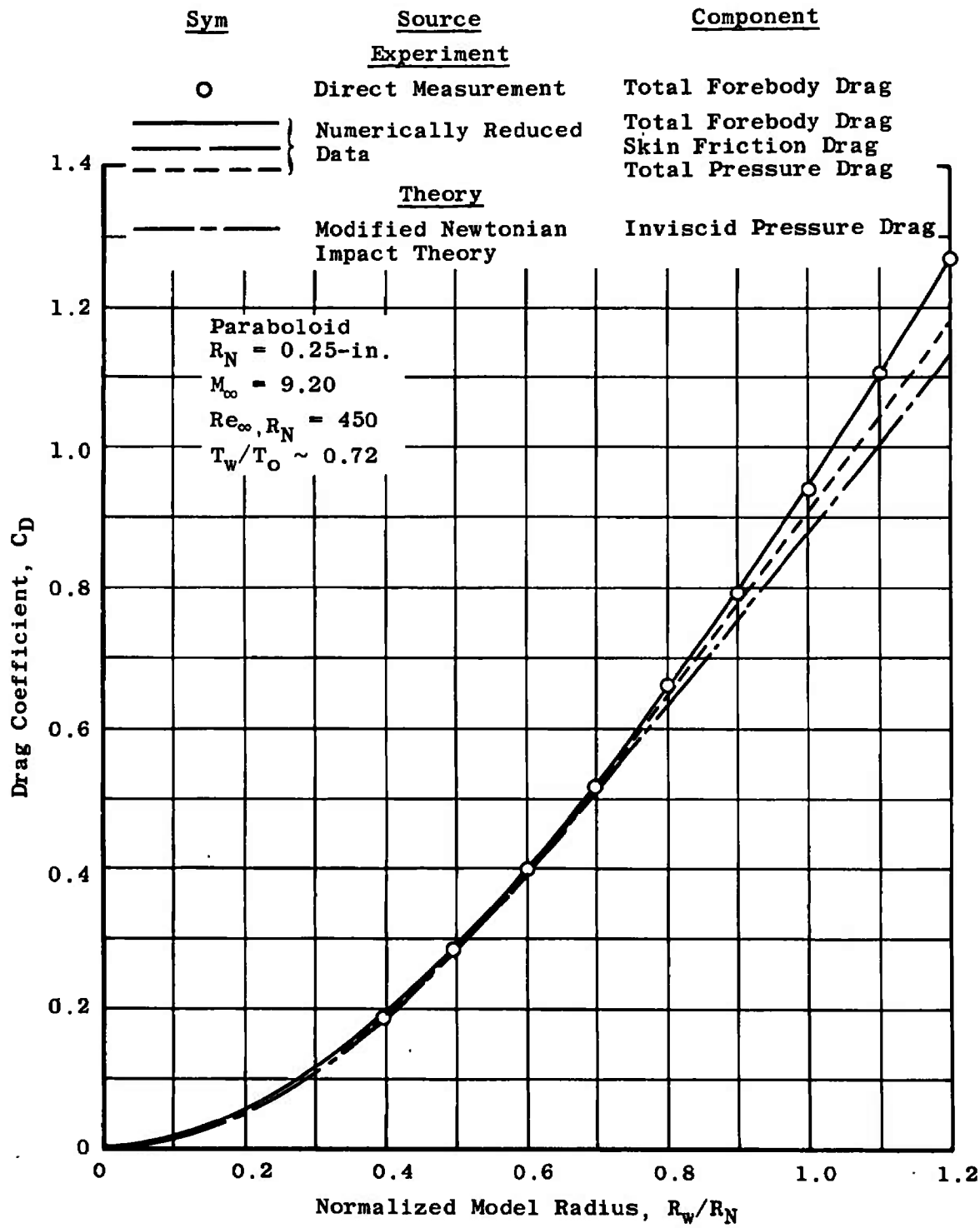

b. Re_{∞, R_N} = 450

Fig. 33 Continued

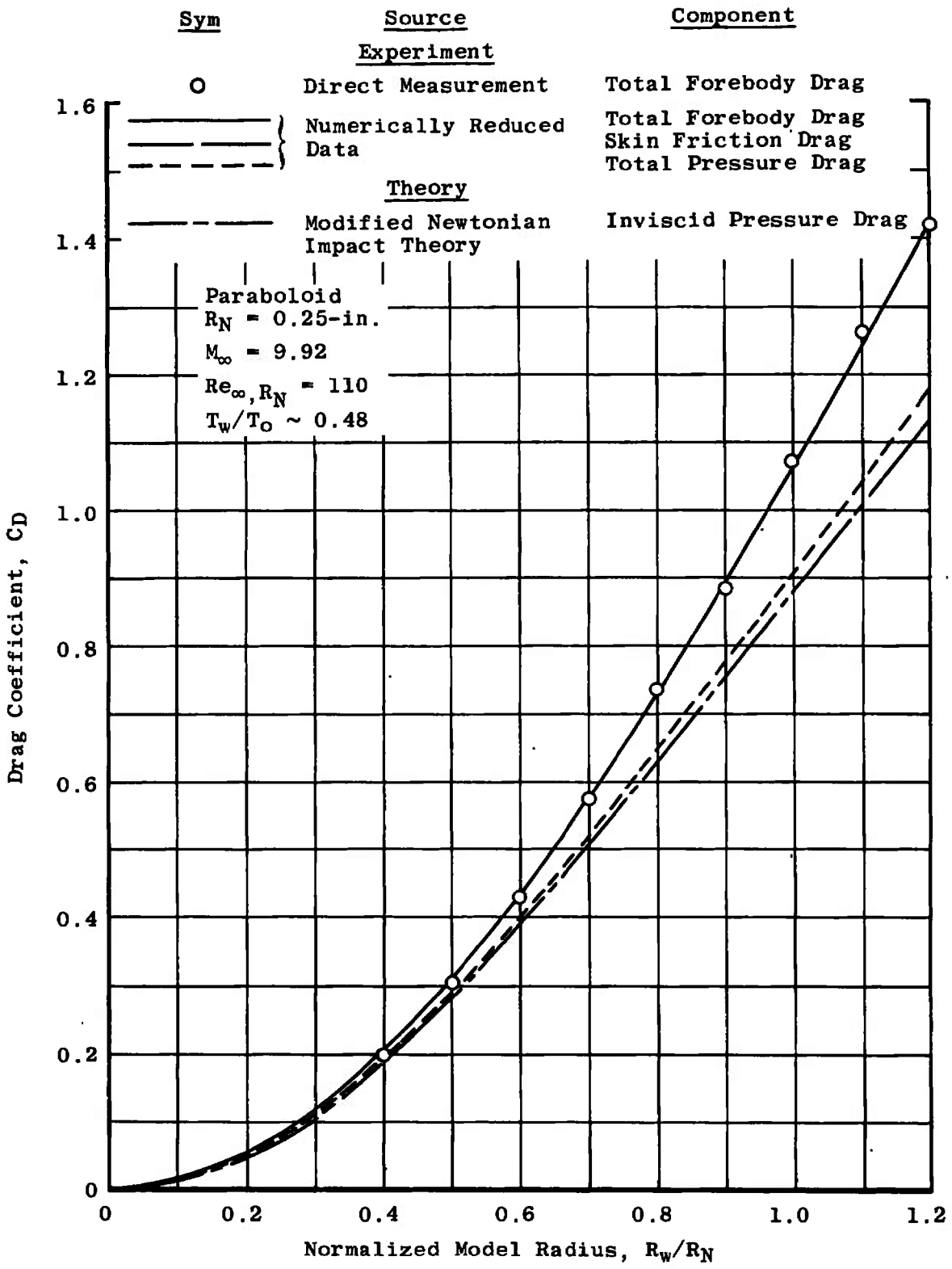

c. Re_{∞, R_N} = 110

Fig. 33 Concluded

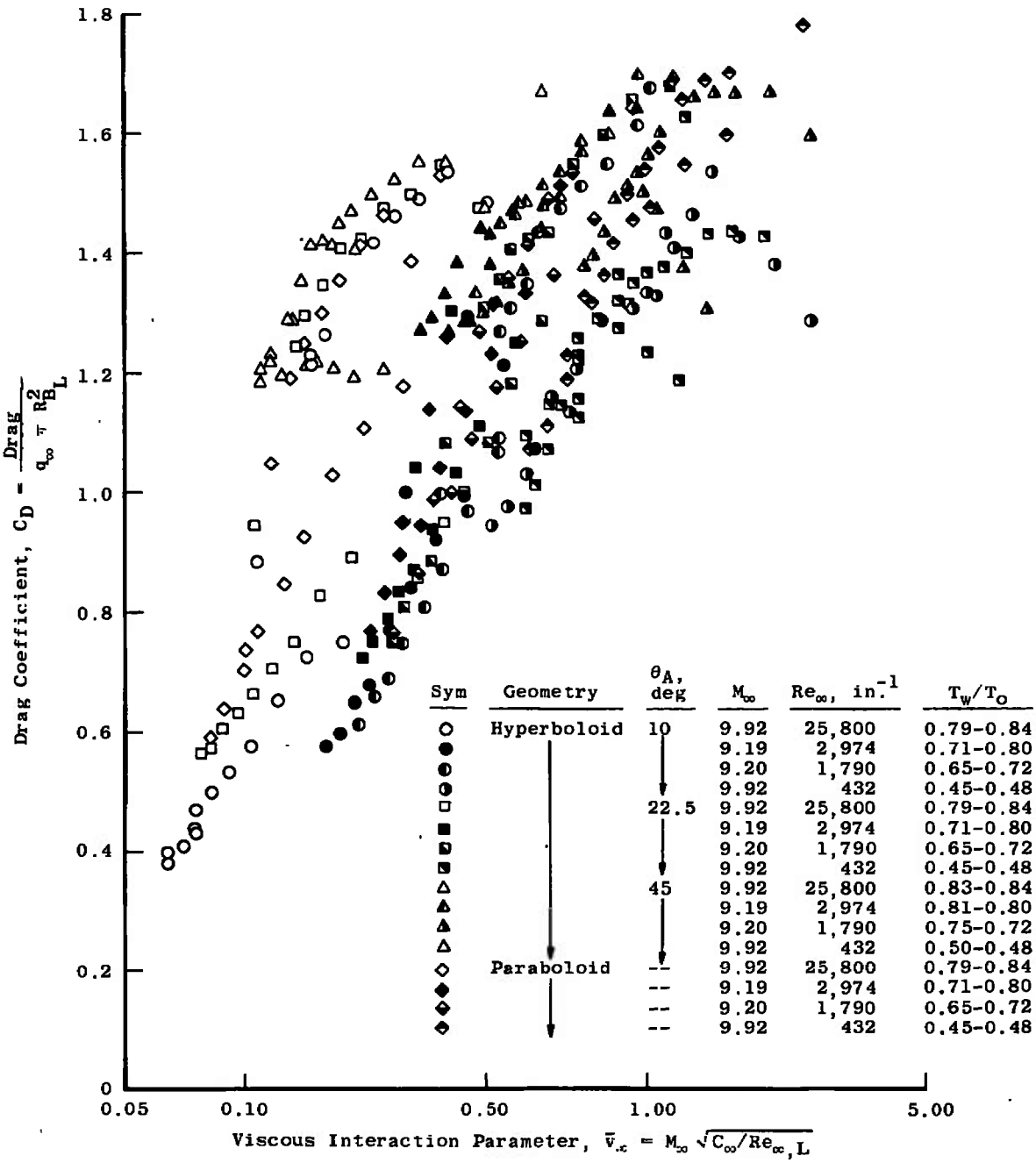

Fig. 34 Experimental Total Drag

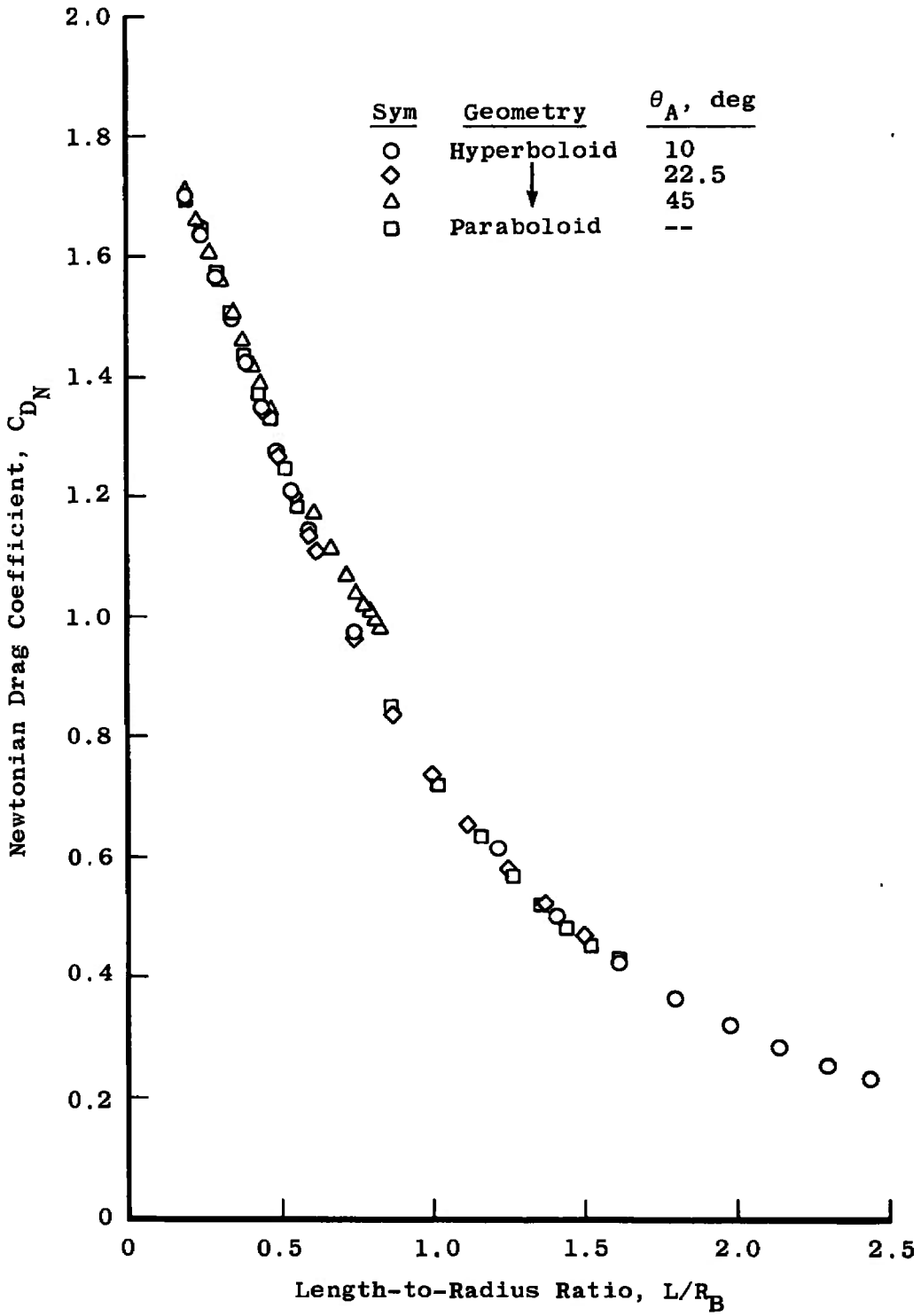

a. Drag of Analytic Bodies Calculated by Modified Newtonian Impact Theory

Fig. 35 Drag Data Summary

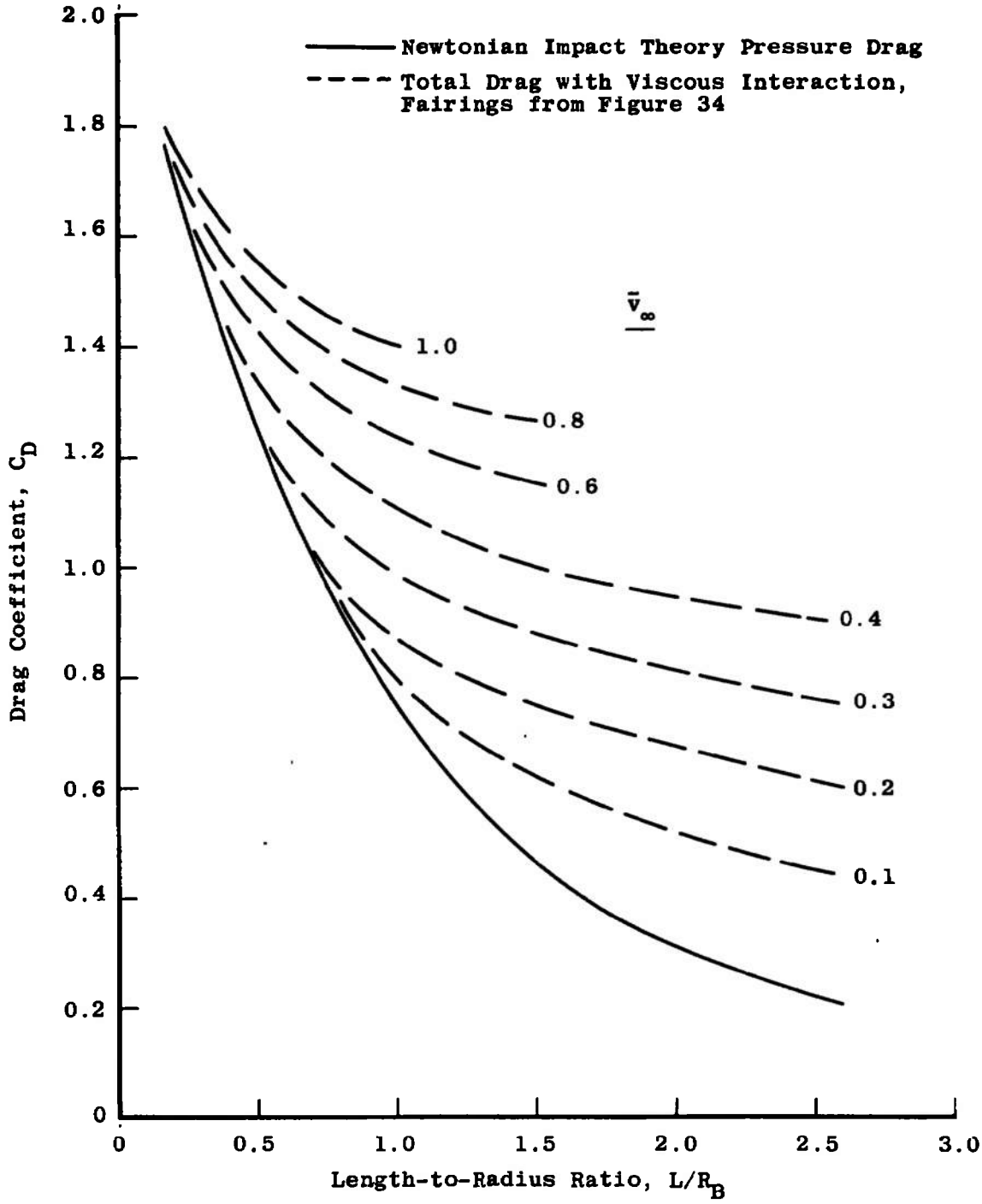

b. Effect of Viscous Interaction on Analytic Body Drag

Fig. 35 Concluded

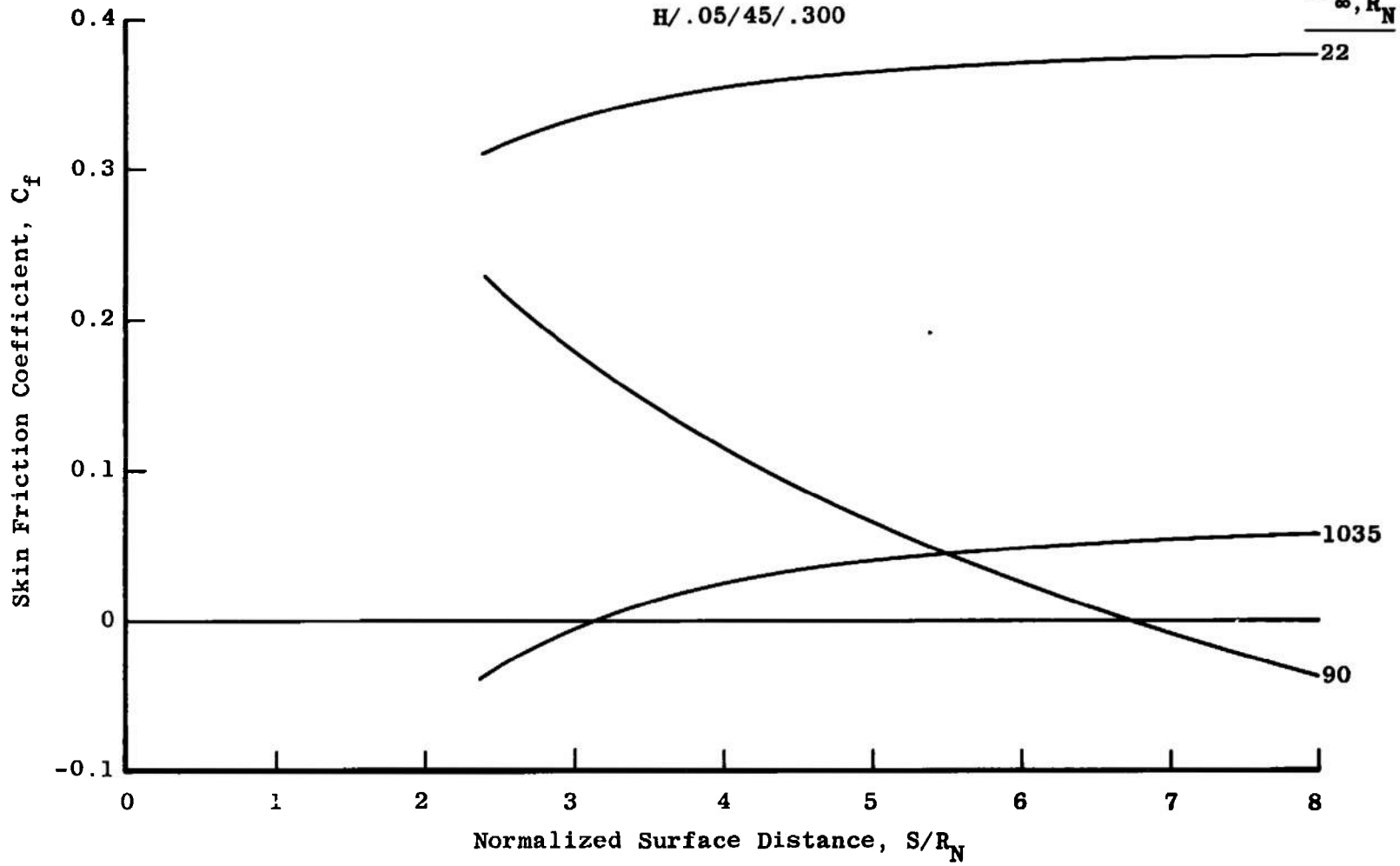

a. 45-deg Hyperboloid

Fig. 36 Skin Friction Results

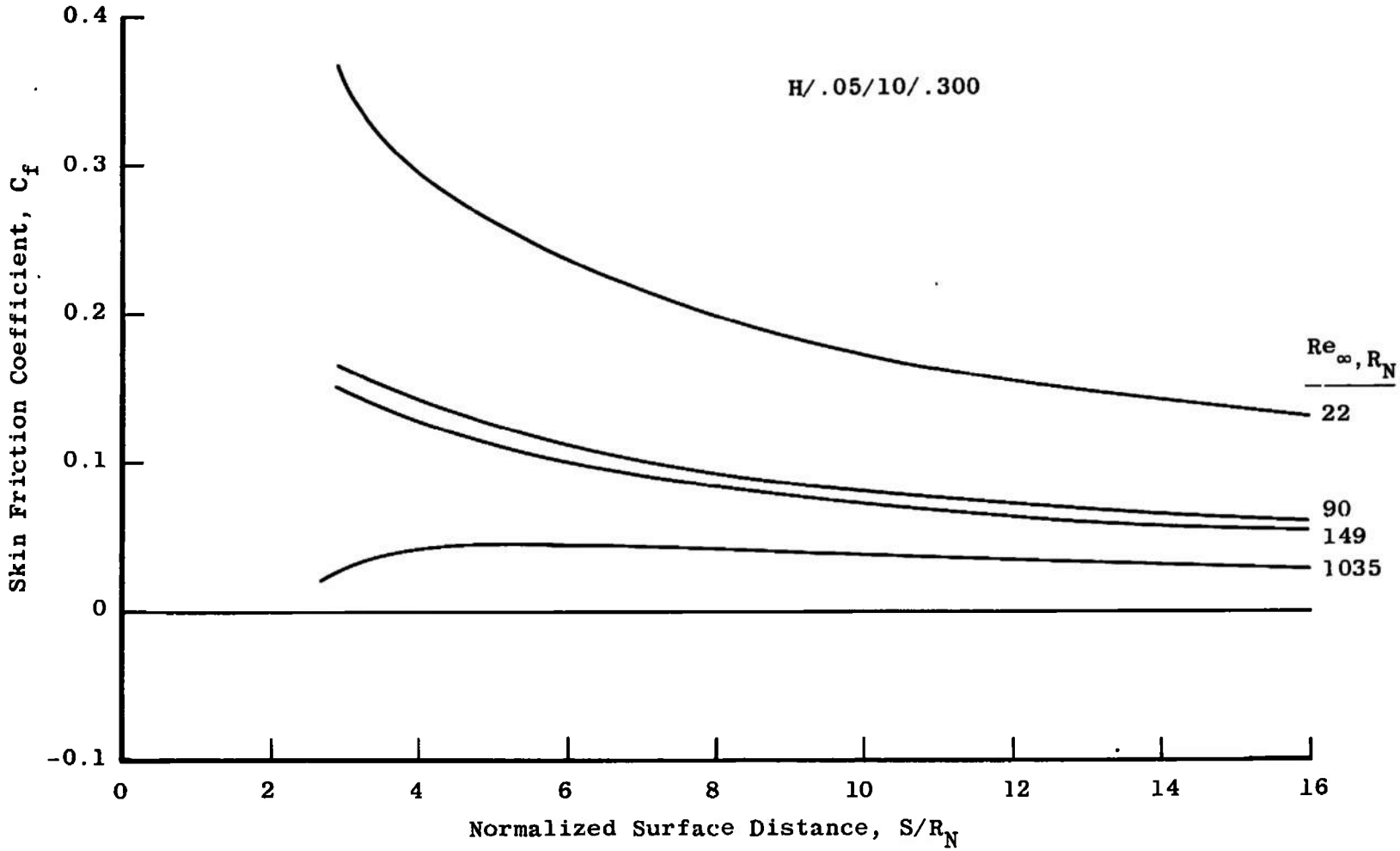

b. 10-deg Hyperboloid

Fig. 36 Continued

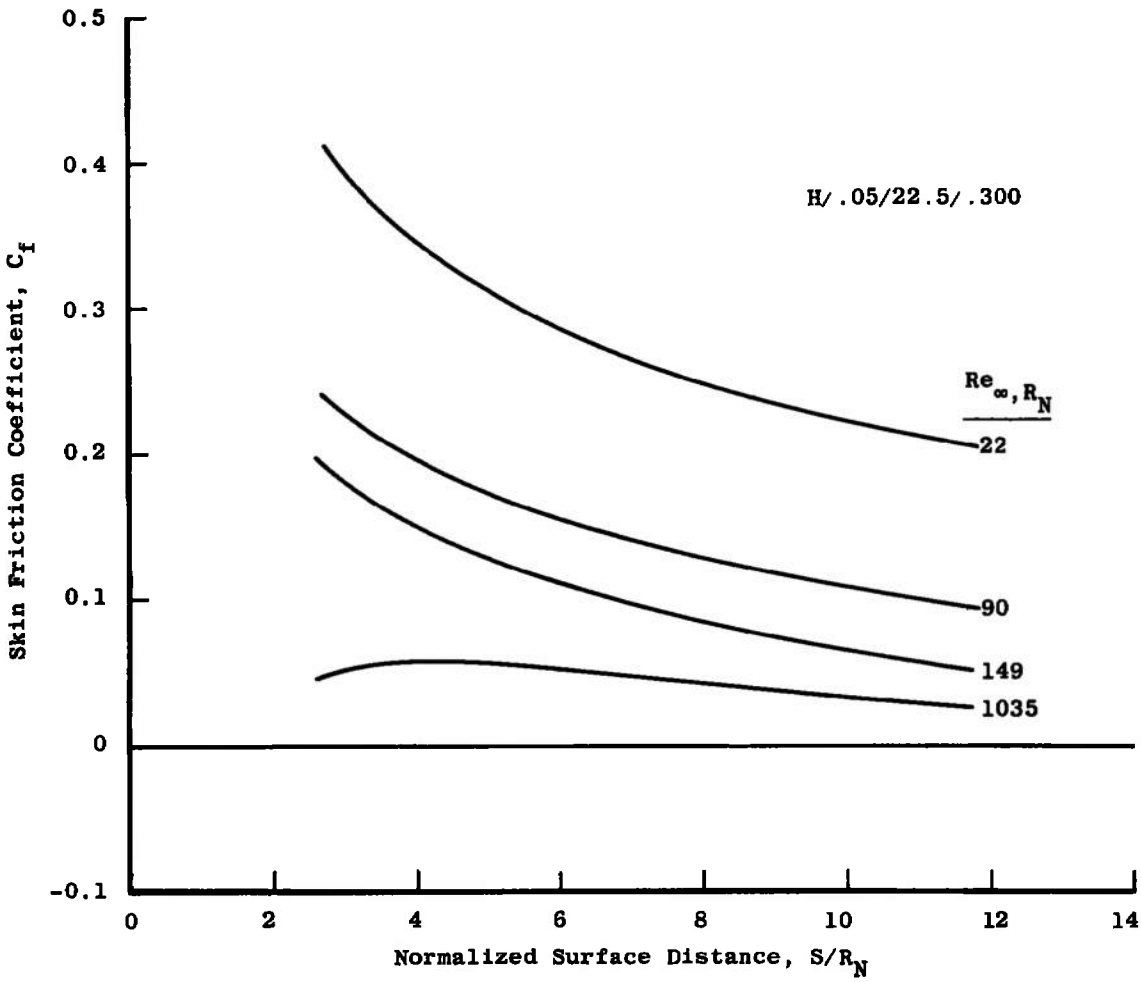

c. 22.5-deg Hyperboloid

Fig. 36 Continued

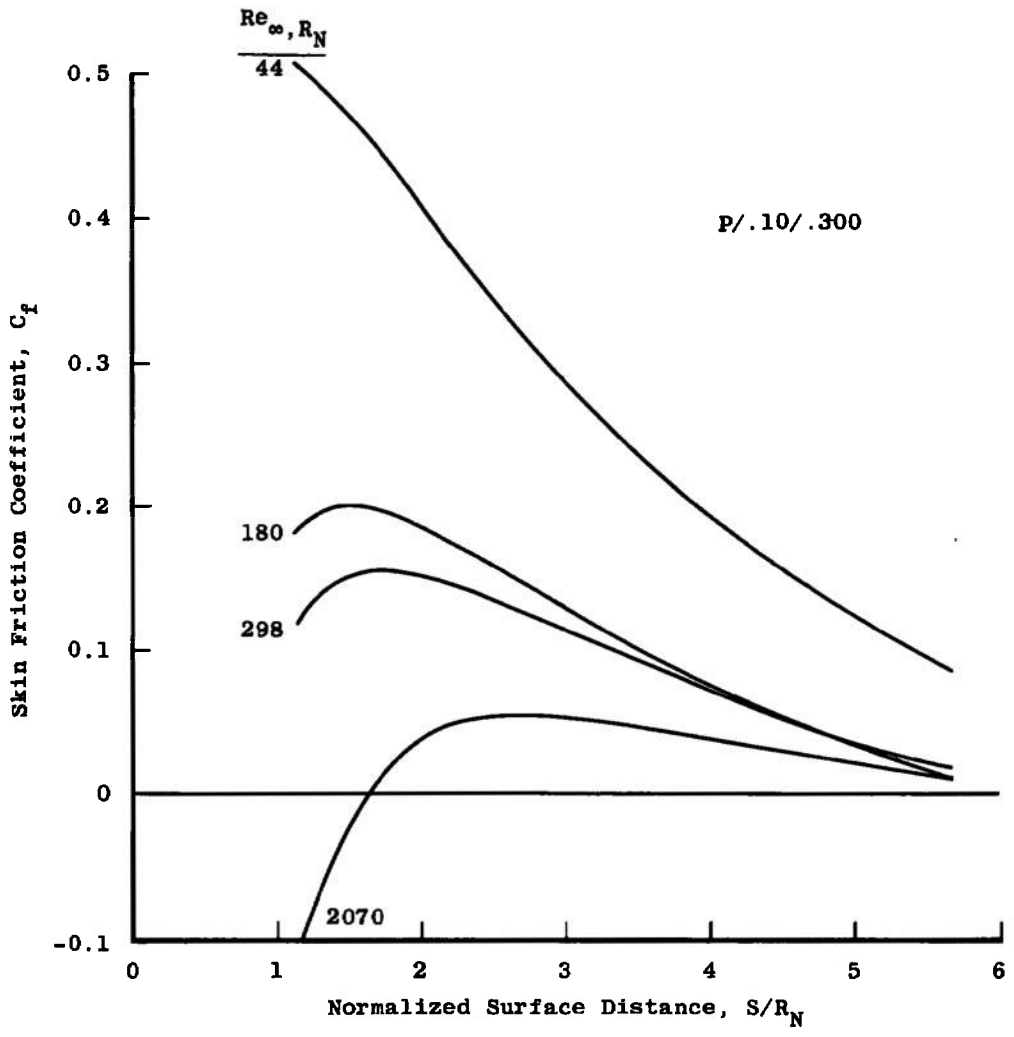

d. Paraboloid

Fig. 36 Concluded

Sym	Body	M_∞	$Re_{\infty,R_N} \times 10^{-6}$	
— —	Sphere	8.06	6.49	
— — — —	Ellipsoid	8.06	1.30	(29)
— - —	Ellipsoid	8.06	0.43	
.....	Spherical Segment	4.76	1.03	(28)
□	10-deg Hyperboloid	10.12	0.064	
○	10-deg Hyperboloid	10.12	0.064	

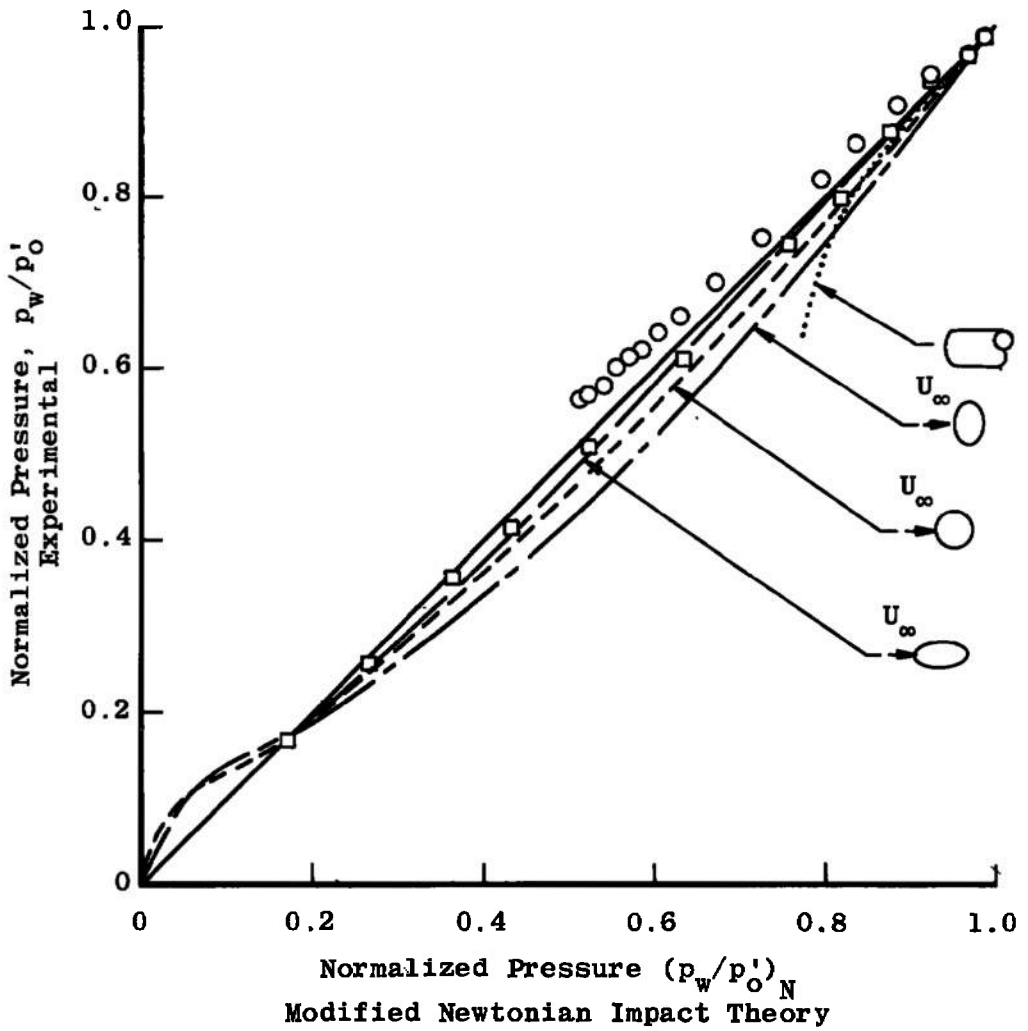

Fig. 37 Comparison of Analytic Body Pressure Data with Results of Modified Newtonian Impact Theory

Experimental

——— Fairing of Present Experimental Data

Numerical

ϵ = Van Dyke Expansion Parameter, Ref. 5

Sym	M_∞	Re_{∞,R_N}	T_w/T_o	ϵ	Source
○	10.0	400	0.20	0.438	First-Plus
●	10.0	400	0.60	0.365	Second-Order
△	10.0	400	0.20	0.438	Theory, Adams (5)
▲	10.0	400	0.60	0.365	
◇	10.03	1196	0.801	0.243	
□	10.0	400	0.20	0.438	Fully Viscous Shock Layer, Davis (6)
▽	21.744	431	0.0535	0.840	Adams (30)

Symbols Corresponding to Body Locations Given are Denoted by Flags, e.g. S/R_N = 5.15 No Flag
7.25 One Flag
10.81 Two Flags

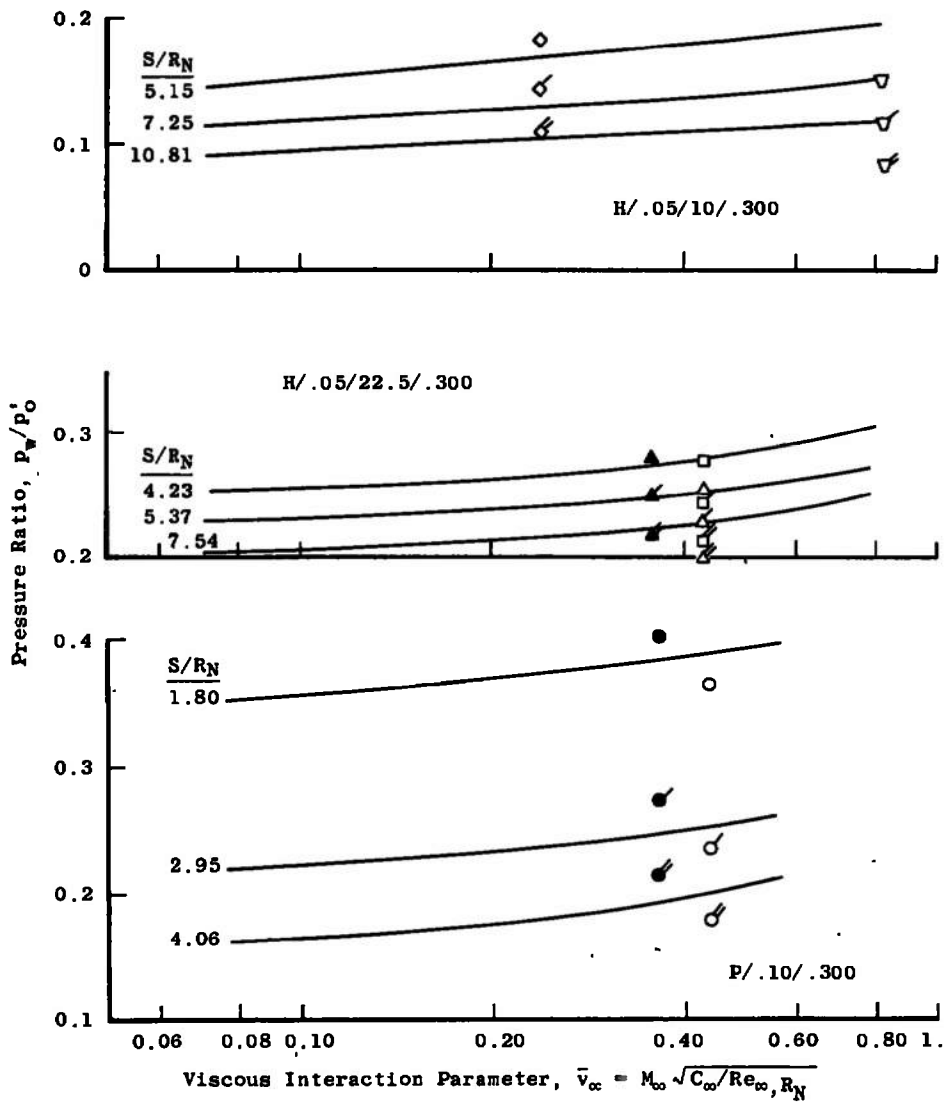

a. Pressure

Fig. 38 Comparison of Analytic Body Data with Numerical Viscous Interaction Results

Experimental

——— Fairing of Present Experimental Data

Numerical

Sym	M_∞	Re_{∞, R_N}	T_w/T_o	ϵ	Source
○	10.0	400	0.20	0.438	First-Plus
●	10.0	400	0.60	0.365	Second-Order
△	10.0	400	0.20	0.438	Theory, Adams (5)
▲	10.0	400	0.60	0.365	
◇	10.03	1196	0.801	0.243	
□	10.0	400	0.20	0.438	Fully Viscous Shock Layer, Davis (6)
▽	21.744	431	0.0535	0.840	Adams (30)

Flagged Symbols Indicate Different Body Locations (S/R_N), see Fig. 38a

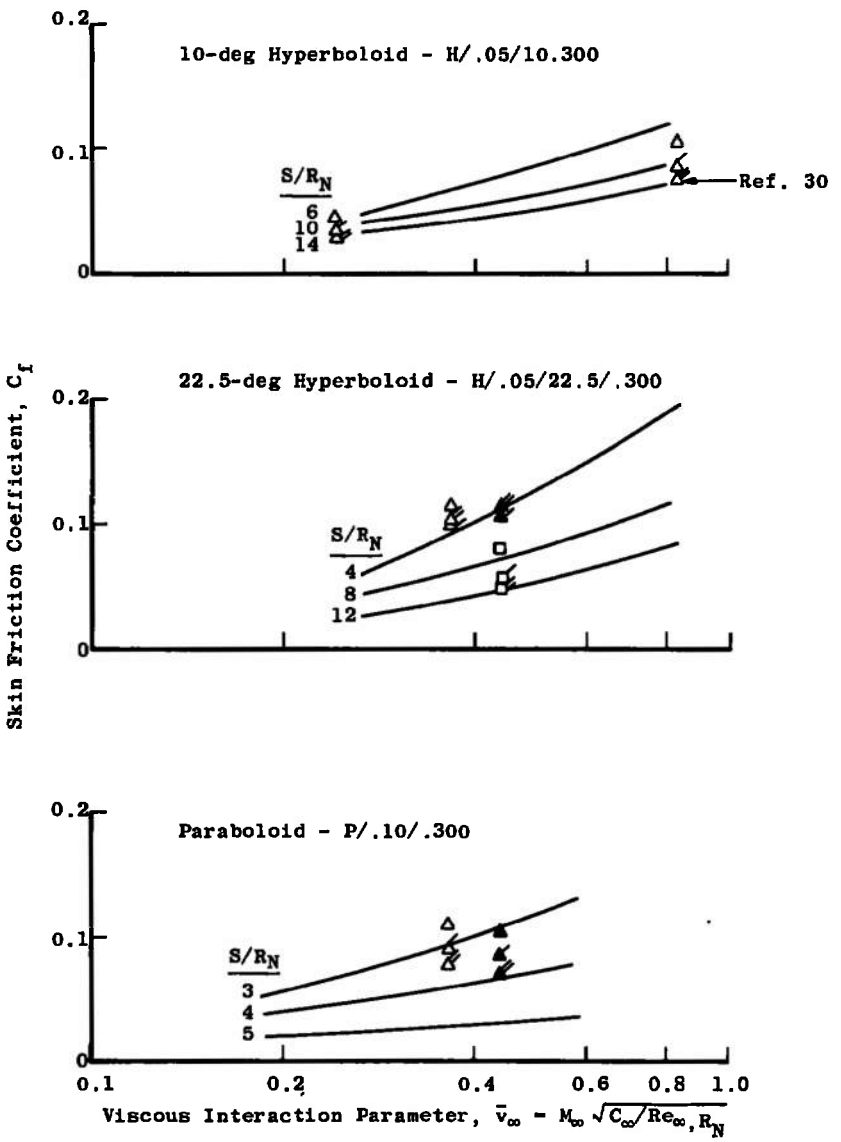

b. Skin Friction Coefficient

Fig. 38 Continued

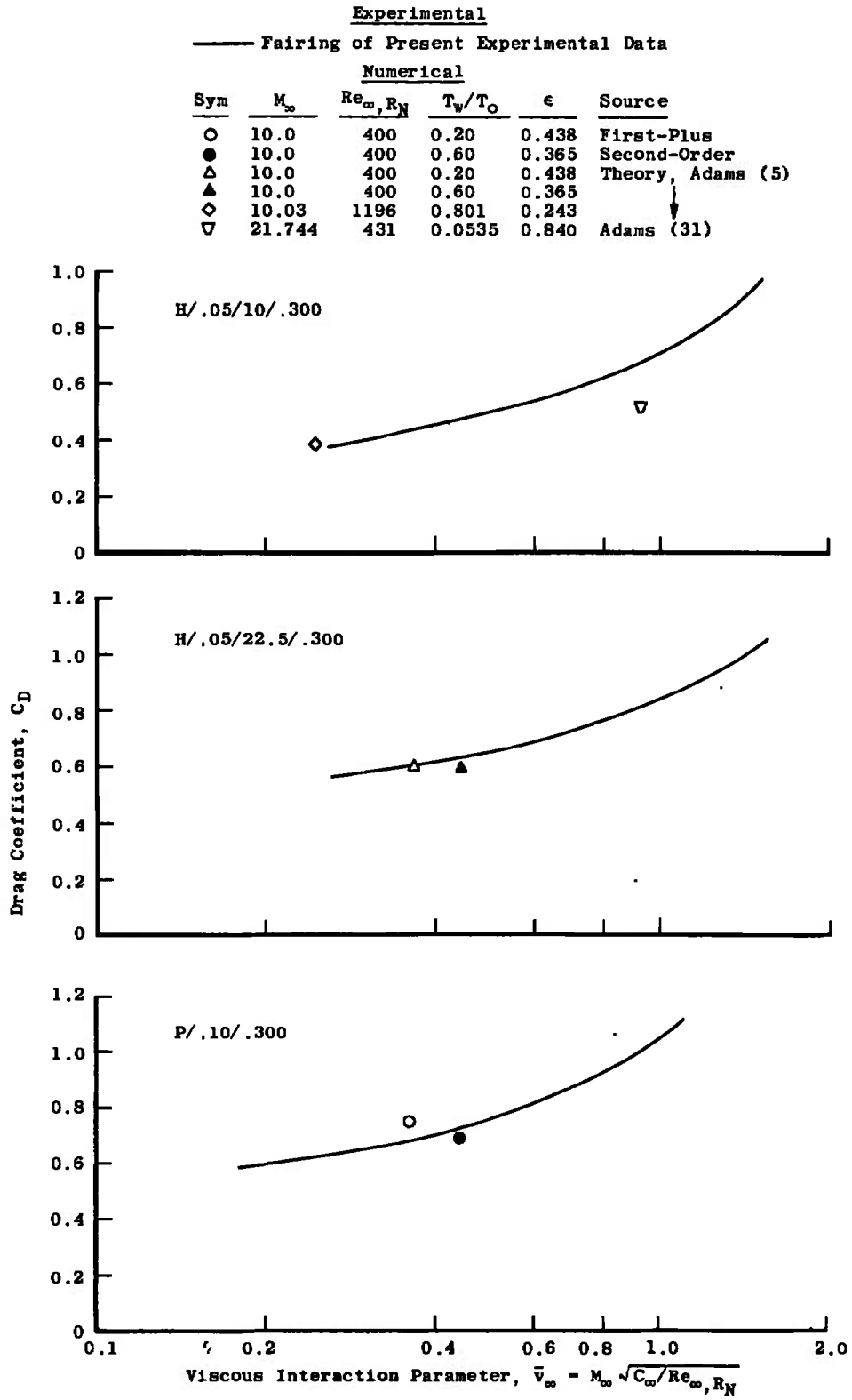

c. Drag

Fig. 38 Concluded

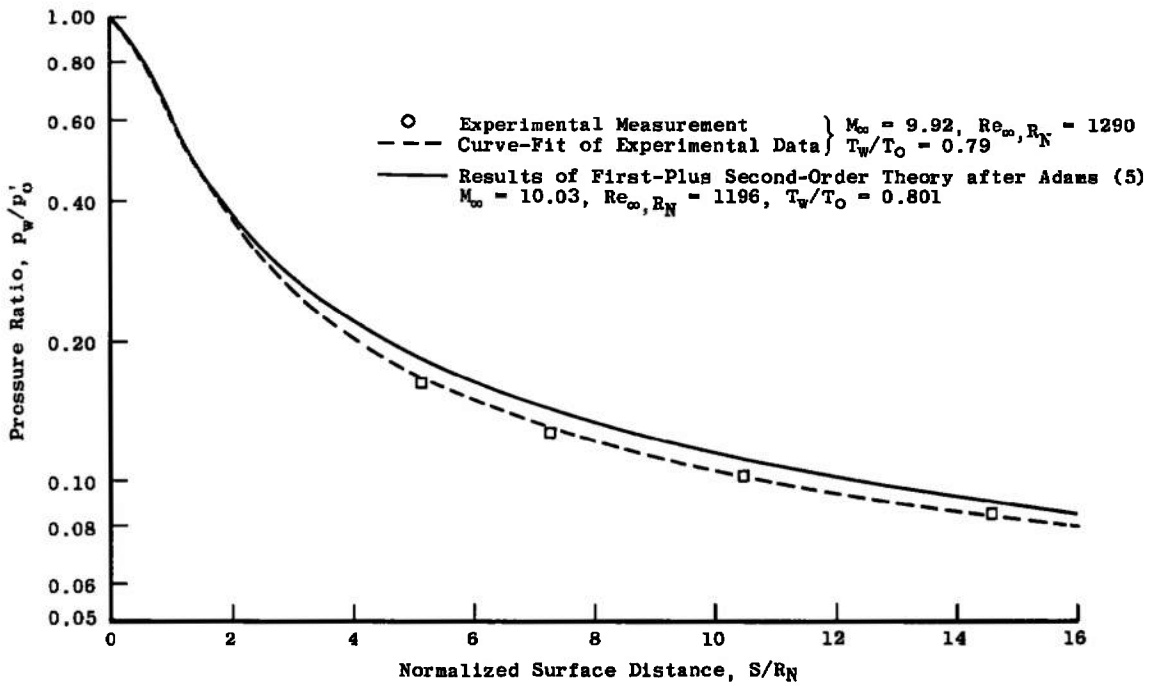

a. Pressure

Fig. 39 Comparison of 10-deg Hyperboloid Data with Second-Order Results

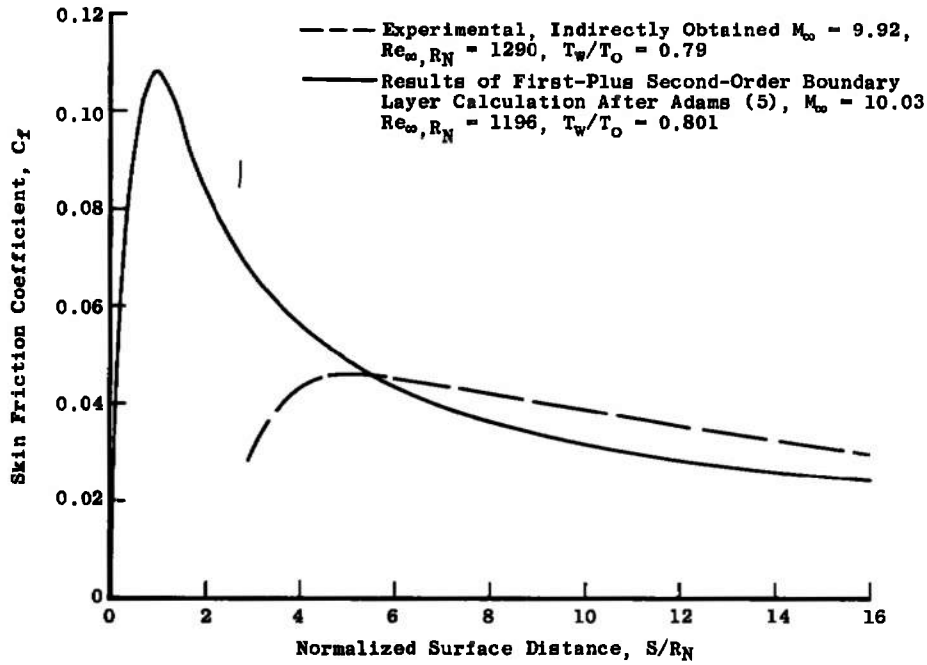

b. Skin Friction Coefficient

Fig. 39 Continued

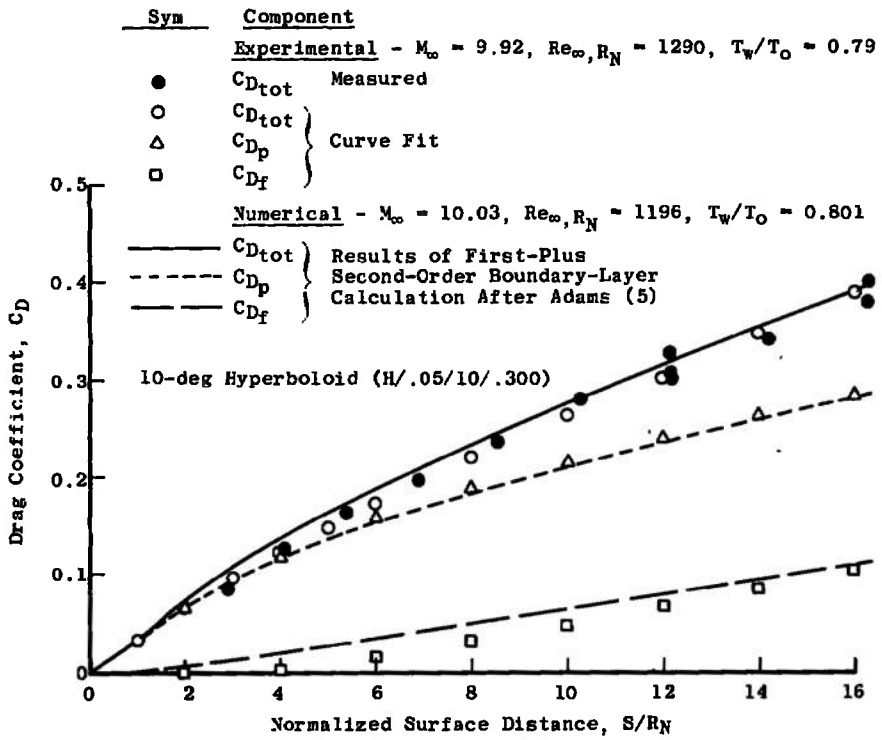

c. Drag

Fig. 39 Concluded

APPENDIX II

The model geometry variations and the type of data taken on each in the present experimental work are presented in Table I. The flow conditions of the wind tunnel tests are presented in Table II, where the parameters are calculated as outlined in Section III. The viscosity data used in the Reynolds numbers were as shown in Fig. 10. Experimental data, Tables III to XIII, are given in the order of presentation in the text. All data are in normalized or coefficient form; conversion to dimensional quantities may be accomplished using the flow conditions of Table II. For the drag and pressure results, both corrected and uncorrected data are shown.

TABLE I
MODEL GEOMETRIES

	θ_A	R_N	Z_B	R_B	S_B/R_N	
Hyperboloid	10	0.050	0.0970	0.100	2.91	Drag
			0.149	0.125	4.07	
			0.211	0.150	5.40	
			0.282	0.175	6.90	
			0.360	0.200	8.54	
			0.445	0.225	10.31	
			0.536	0.250	12.20	
			0.632	0.275	14.19	
			0.733	0.300	16.27	Pressure Temp.
		0.150	0.291	0.300	2.19	
		0.250	0.0200	0.100	0.410	
			0.0312	0.125	0.520	
			0.0449	0.150	0.634	
			0.0610	0.175	0.753	
			0.0796	0.200	0.878	
			0.101	0.225	1.01	
			0.124	0.250	1.15	
			0.150	0.275	1.29	
			0.178	0.300	1.44	Pressure
		0.500	7.33	3.00	16.27	Pressure Temp.

TABLE I (Continued)

	θ_A	R_N	Z_B	R_B	S_B/R_N		
Hyperboloid	22.5	0.050	0.4893	0.100	2.75	Drag	
			0.4337	0.125	3.71		
			0.3788	0.150	4.75		
			0.3250	0.175	5.84		
			0.2726	0.200	6.97		
			0.2218	0.225	8.13		
			0.1734	0.250	9.32		
			0.1281	0.275	10.52		
			0.0870	0.300	11.74		Pressure
		0.150	0.2611	0.300	2.75		
		0.250	0.1701	0.100	0.410		
			0.1441	0.125	0.520		
			0.1200	0.150	0.633		
			0.0979	0.175	0.751		
			0.0779	0.200	0.874		
			0.0600	0.225	1.000		
			0.0443	0.250	1.14		
			0.0309	0.275	1.27		
			0.0199	0.300	1.47		
	45	0.050	0.0618	0.100	2.39	Drag	
			0.0846	0.124	3.07		
			0.1081	0.150	3.75		
			0.1320	0.775	4.45		
			0.1562	0.200	5.14		
			0.1805	0.225	5.84		
			0.2050	0.250	6.54		
			0.2295	0.275	7.24		
			0.2541	0.300	7.94	Drag	Pressure Temp.
		0.100	0.2162	0.300	3.75		
		0.150	0.0843	0.180	1.35		
			0.1854	0.300	2.39		
		0.200	0.1124	0.240	1.35		
			0.1606	0.300	1.73		

TABLE I (Concluded)

	θ_A	R_N	Z_B	R_B	S_B/R_N		
		0.250	0.0193	0.100	0.410	Drag	
			0.0295	0.125	0.518		
			0.0416	0.150	0.629		
			0.0552	0.175	0.743		
			0.0702	0.200	0.859		
			0.0863	0.225	0.978		
			0.1036	0.250	1.10		
			0.1217	0.275	1.22		
			0.1405	0.300	1.35		Pressure Temp.
		0.500	2.541	3.000	7.94		Pressure Temp.
Paraboloid		0.100	0.0500	0.100	1.15	Drag	
			0.0781	0.125	1.52		
			0.113	0.150	1.95		
			0.153	0.175	2.43		
			0.200	0.200	2.96		
			0.253	0.225	3.55		
			0.313	0.250	4.19		
			0.378	0.275	4.89		
			0.450	0.300	5.65		Pressure
		0.150	0.300	0.300	2.96		
		0.200	0.225	0.300	1.95		
		0.250	0.0200	0.100	0.410		
			0.0313	0.125	0.520		
			0.0450	0.150	0.634		
			0.0613	0.175	0.754		
			0.0800	0.200	0.879		
			0.101	0.225	1.01		
			0.125	0.250	1.15		
			0.151	0.275	1.29		
			0.180	0.300	1.45		Pressure

TABLE II
TEST CONDITIONS

M_∞	Re_∞ 1/in.	p_0 lbf/in	T_0 °K	H_0 BTU/lbm	p'_{0_2} lbf/in^2	q_∞ lbf/in^2	p_∞ lbf/in^2	ρ_∞ lbm/ft^3	U_∞ ft/sec	T_∞ °K	Test Gas
10.12	126,700	1200	1030	465	3.36	1.80	2.510×10^{-2}	7.52×10^{-4}	4720	50.2	Air
9.92	25,800	200	920	410	0.630	0.326	4.800×10^{-3}	1.50×10^{-4}	4431	46.1	Air
9.19	2,974	19	1040	483	0.0896	0.0482	8.157×10^{-4}	1.99×10^{-5}	4740	59.5	N_2
9.20	1,790	25	1670	812	0.115	0.0623	1.052×10^{-3}	1.58×10^{-5}	6051	96.7	N_2
9.92	432	18	3005	1557	0.0588	0.0318	4.621×10^{-4}	4.40×10^{-6}	8187	152.2	N_2

TABLE III
SURFACE DATA ON A 6.0-IN. BASE DIAM, 10-DEG HYPERBOLOID

			Re_∞/R_N	63,800	12,900	63,800	12,900
Orifice Number	r_w/R_N	z/R_N	S/R_N	P_w/P'_{0_2}	P_w/P'_{0_2}	T_w/T_0	T_w/T_0
1	0.1	0.005	0.100	0.990	0.990	0.900	0.822
2	0.2	0.020	0.201	0.970	0.970		
3	0.3	0.045	0.305	0.938	0.914		
4	0.4	0.080	0.411	0.876	0.866		
5	0.5	0.125	0.520	0.801	0.810		
6	0.6	0.180	0.635	0.746	0.741		
7	0.8	0.320	0.880	0.611	0.618		
8	1.0	0.499	1.15	0.510	0.520		
9	1.2	0.712	1.44	0.419	0.433		
10	1.4	0.963	1.76	0.360	0.365	0.878	0.803
11	1.6	1.26	2.12	---	0.310		
12	1.8	1.58	2.50	0.259	0.268	0.869	0.793
13	2.0	1.94	2.91	0.225	0.238		
14	2.5	2.99	4.07	0.170	0.179	0.841	0.768
15	3.0	4.22	5.40	0.131	0.142		
16	3.5	5.63	6.90	0.111	0.120		
17	4.0	7.20	8.54	0.0949	0.101	0.792	0.721
18	4.5	8.89	10.31	0.0832	0.0903		
19	5.0	10.72	12.70	0.0768	0.0809		
20	5.5	12.64	14.19	0.0699	0.0750	0.738	0.677

TABLE IV
SURFACE DATA ON A 6.0-IN. BASE DIAM, 45-DEG HYPERBOLOID

Orifice Number	r_w/R_N	z/R_N	Re_∞, R_N S/R_N	63,800 P_w/P_o'	12,900 P_w/P_o'	63,800 T_w/T_o	12,900 T_w/T_o
1	0.1	0.005	0.1	0.990	0.990		
2	0.2	0.020	0.2	0.976	0.977	0.939	0.870
3	0.3	0.043	0.3	0.940	0.929		
4	0.4	0.077	0.41	0.912	0.901	0.938	0.869
5	0.5	0.119	0.52	0.865	0.858		
6	0.6	0.167	0.63	0.822	0.820	0.938	0.867
7	0.8	0.281	0.86	0.754	0.740		
8	1.0	0.414	1.10	0.704	0.702	0.930	0.864
9	1.2	0.563	1.35	0.662	0.666		
10	1.4	0.720	1.61	0.645	0.649		
11	1.6	0.888	1.87	0.623	0.633		
12	1.8	1.06	2.13	0.614	0.627	0.917	0.852
13	2.0	1.24	2.40	0.601	0.603		
14	2.5	1.69	3.07	0.581	0.590	0.905	0.837
15	3.0	2.16	3.76	0.584			
16	3.5	2.64	4.45	0.574	0.591		
17	4.0	3.12	5.14	0.575	0.580	0.872	0.803
18	4.5	3.60	5.84	0.576	0.583		
19	5.0	4.10	6.54	0.569	0.576		
20	5.5	4.58	7.24	0.569	0.571	0.847	0.781

TABLE V
SHOCK-LAYER PITOT SURVEY DATA ON A 6.0-IN. BASE DIAM, 10-DEG HYPERBOLOID

S/R_N = 2.10					
Re_∞, R_N	Y/R_N	P_w/P_o'	Re_∞, R_N	Y/R_N	P_w/P_o'
12,900	0.0330	0.154	63,800	0.0350	0.255
	0.0530	0.175		0.0590	0.317
	0.0710	0.245		0.0790	0.489
	0.0930	0.303		0.0910	0.666
	0.109	0.449		0.115	0.922
	0.131	0.607		0.133	1.02
	0.153	0.770		0.157	1.06
	0.173	0.867		0.177	1.11
	0.193	0.985		0.197	1.16
	0.217	1.08		0.213	1.21
	0.235	1.15		0.233	1.26
	0.253	1.20		0.255	1.33
	0.273	1.26		0.279	1.39
	0.295	1.31		0.293	1.45
	0.311	1.36		0.319	1.53
	0.335	1.43		0.337	1.58
	0.355	1.49		0.357	1.64
	0.371	1.53		0.377	1.70
	0.393	1.61		0.397	1.76
	0.417	1.67		0.417	1.82
	0.429	1.72		0.433	1.87
	0.451	1.79		0.455	1.94
	0.475	1.86		0.475	2.02
	0.491	1.92		0.491	2.07
	0.515	2.00		0.513	2.15
	0.531	2.07		0.539	2.23
	0.553	2.16		0.557	2.29
	0.575	2.21		0.575	2.35
	0.593	2.28		0.601	2.44
	0.611	2.35		0.617	2.50
	0.629	2.41		0.637	2.56
	0.651	2.50		0.655	2.63
	0.669	2.56		0.673	2.71
	0.691	2.63		0.697	2.80
	0.715	2.72		0.713	2.88
	0.739	2.79		0.733	2.98
	0.755	2.86		0.757	3.05

TABLE V (Continued)

$S/R_N = 2.10$					
Re_∞, R_N	Y/R_N	P_w/P_o'	Re_∞, R_N	Y/R_N	P_w/P_o'
12,900	0.775	2.94	63,800	0.771	3.14
	0.797	3.00		0.801	3.24
	0.811	3.06		0.811	3.31
	0.831	3.11		0.839	3.40
	0.855	3.20		0.857	3.47
	0.869	3.26		0.875	3.56
	0.897	3.34		0.891	3.59
	0.915	3.41		0.913	3.22
	0.933	3.40		0.935	2.13
	0.953	3.12		0.977	0.867
	0.985	2.03		1.01	0.798
	1.03	0.844		1.01	0.798
	1.08	0.802		1.08	0.797

TABLE V (Continued)

S/R_N = 12.20					
Re_{∞,R_N}	Y/R_N	P_w/P_o'	Re_{∞,R_N}	Y/R_N	P_w/P_o'
12,900	0.0330	0.0510	63,800	0.0370	0.104
	0.0470	0.0659		0.0590	0.107
	0.0690	0.0750		0.0770	0.140
	0.0890	0.0874		0.0990	0.196
	0.113	0.106		0.117	0.272
	0.131	0.131		0.141	0.411
	0.151	0.146		0.157	0.552
	0.173	0.210		0.179	0.679
	0.195	0.271		0.197	0.766
	0.209	0.318		0.215	0.822
	0.229	0.385		0.233	0.869
	0.251	0.464		0.255	0.914
	0.267	0.526		0.279	0.957
	0.293	0.619		0.299	0.998
	0.309	0.684		0.319	1.03
	0.329	0.758		0.337	1.07
	0.347	0.826		0.361	1.12
	0.377	0.892		0.377	1.16
	0.387	0.941		0.393	1.20
	0.415	0.984		0.419	1.25
	0.427	1.03		0.437	1.29
	0.455	1.07		0.455	1.32
	0.469	1.08		0.477	1.37
	0.487	1.13		0.497	1.41
	0.509	1.18		0.517	1.45
	0.527	1.23		0.539	1.49
	0.551	1.28		0.555	1.53
	0.571	1.34		0.575	1.57
	0.591	1.37		0.599	1.61
	0.611	1.43		0.617	1.63
	0.627	1.45		0.633	1.67
	0.653	1.50		0.659	1.71
	0.671	1.54		0.675	1.74
	0.685	1.58		0.697	1.78
	0.711	1.62		0.713	1.80
	0.725	1.66		0.733	1.84
	0.753	1.69		0.757	1.89
	0.773	1.73		0.775	1.92
	0.793	1.77		0.797	1.96
	0.811	1.80		0.813	1.99

TABLE V (Continued)

S/R_N = 12.20					
Re_∞, R_N	Y/R_N	P_w/P_0'	Re_∞, R_N	Y/R_N	P_w/P_0'
12,900	0.831	1.83	63,800	0.837	2.02
	0.847	1.86		0.857	2.06
	0.865	1.89		0.879	2.10
	0.887	1.94		0.899	2.13
	0.909	1.98		0.921	2.18
	0.925	2.01		0.937	2.21
	0.925	2.01		0.955	2.24
	0.943	2.05		0.975	2.28
	0.969	2.09		0.997	2.33
	0.917	2.00		0.969	2.27
	0.941	2.04		0.989	2.30
	0.957	2.08		1.00	2.34
	0.987	2.12		1.02	2.38
	0.993	2.16		1.04	2.43
	1.02	2.19		1.07	2.46
	1.04	2.22		1.08	2.49
	1.05	2.25		1.11	2.53
	1.08	2.28		1.13	2.57
	1.09	2.32		1.14	2.60
	1.11	2.35		1.17	2.62
	1.14	2.38		1.19	2.66
	1.16	2.42		1.20	2.69
	1.18	2.45		1.22	2.72
	1.19	2.48		1.24	2.76
	1.21	2.50		1.26	2.79
	1.24	2.54		1.28	2.83
	1.26	2.57		1.30	2.86
	1.28	2.60		1.32	2.90
	1.30	2.63		1.35	2.93
	1.32	2.66		1.37	2.97
	1.34	2.69		1.39	3.01
	1.36	2.72		1.40	3.04
	1.38	2.74		1.43	3.07
	1.40	2.76		1.44	3.11
	1.41	2.79		1.47	3.15
	1.44	2.82		1.48	3.18
	1.45	2.85		1.51	3.22
	1.47	2.89		1.53	3.25
	1.50	2.92		1.55	3.30
	1.52	2.94		1.57	3.34

TABLE V (Concluded)

S/R_N = 12.20					
Re_{∞,R_N}	Y/R_N	P_w/P_0'	Re_{∞,R_N}	Y/R_N	P_w/P_0'
12,900	1.54	2.97	63,800	1.59	3.37
↓	1.55	3.01	↓	1.60	3.40
	1.58	3.04		1.62	3.44
	1.60	3.06		1.65	3.47
	1.62	3.09		1.67	3.49
	1.63	3.11		1.69	3.45
	1.65	3.14		1.70	3.26
	1.68	3.17		1.73	2.58
	1.70	3.20		1.75	1.90
	1.72	3.25		1.77	1.23
	1.73	3.25		1.79	1.03
	1.76	3.22		1.81	0.959
	1.78	3.06		1.82	0.952
	1.80	2.69		1.84	0.950
	1.82	2.27		1.86	0.949
	1.82	2.27		1.88	0.948
↓	1.84	1.83	↓	1.91	0.948

TABLE VI
SHOCK-LAYER PITOT SURVEY DATA ON A 6.0-IN. BASE DIAM, 45-DEG HYPERBOLOID

S/R_N = 1.84					
Re_{∞,R_N}	Y/R_N	P_w/P_o'	$Re_{\infty,R}$	Y/R_N	P_w/P_o'
12,900	0.0245	0.819	63,800	0.0565	1.16
↓	0.0405	0.853	↓	0.0705	1.21
	0.0624	0.940		0.0865	1.26
	0.0845	1.03		0.103	1.31
	0.107	1.13		0.133	1.40
	0.125	1.20		0.147	1.44
	0.143	1.26		0.167	1.50
	0.163	1.31		0.187	1.55
	0.185	1.37		0.213	1.62
	0.211	1.43		0.229	1.66
	0.225	1.48		0.245	1.71
	0.245	1.51		0.265	1.76
	0.263	1.55		0.287	1.81
	0.287	1.59		0.305	1.84
	0.311	1.64		0.329	1.90
	0.327	1.67		0.347	1.89
	0.343	1.71		0.367	1.98
	0.369	1.75		0.387	2.01
	0.387	1.78		0.405	2.04
	0.407	1.81		0.429	2.07
	0.425	1.83		0.443	2.09
	0.447	1.85		0.471	2.12
	0.467	1.87		0.485	2.13
	0.481	1.88		0.511	2.16
	0.509	1.89		0.529	2.17
	0.527	1.89		0.545	2.19
	0.551	1.92		0.573	2.21
	0.559	1.92		0.587	2.23
	0.585	1.94		0.609	2.27
	0.603	1.98		0.631	2.14
	0.627	2.01		0.645	1.92
	0.649	2.05		0.665	1.46
	0.663	2.02		0.689	1.18
	0.691	1.74		0.711	0.983
	0.703	1.40		0.731	0.816
	0.727	1.14		0.745	0.662
	0.753	0.914		0.769	0.450

TABLE VI (Continued)

$S/R_N = 1.84$					
Re_{∞,R_N}	Y/R_N	P_w/P_o'	Re_{∞,R_N}	Y/R_N	P_w/P_o'
12,900	0.767	0.755	63,800	0.787	0.335
↓	0.789	0.572	↓	0.803	0.304
	0.807	0.384		0.825	0.296
	0.827	0.300		0.853	0.292
	0.845	0.269		0.871	0.291
	0.867	0.266		0.893	0.290
	0.895	0.258		0.909	0.290
	0.907	0.258		0.927	0.290
	0.919	0.255	↓	0.927	0.290
	0.947	0.255			
↓	0.967	0.256			

TABLE VI (Continued)

S/R_N = 6.54					
Re_{∞,R_N}	Y/R_N	P_w/P_o'	Re_{∞,R_N}	Y/R_N	P_w/P_o'
12,900	0.0245	0.613	63,800	0.0505	1.09
	0.0525	0.654		0.0665	1.33
	0.0645	0.726		0.0825	1.52
	0.0845	0.815		0.101	1.69
	0.103	0.912		0.121	1.80
	0.133	1.03		0.149	1.93
	0.145	1.10		0.189	2.07
	0.169	1.16		0.207	2.13
	0.197	1.30		0.223	2.17
	0.209	1.42		0.245	2.21
	0.229	1.59		0.265	2.24
	0.245	1.68		0.283	2.27
	0.269	1.79		0.303	2.30
	0.285	1.87		0.325	2.32
	0.305	1.95		0.343	2.32
	0.329	2.00		0.361	2.35
	0.353	2.05		0.385	2.36
	0.369	2.08		0.403	2.37
	0.385	2.11		0.423	2.37
	0.403	2.14		0.449	2.39
	0.427	2.16		0.461	2.39
	0.451	2.19		0.481	2.40
	0.469	2.20		0.503	2.41
	0.491	2.22		0.529	2.41
	0.503	2.23		0.543	2.43
	0.531	2.25		0.563	2.43
	0.549	2.27		0.587	2.44
	0.575	2.28		0.601	2.44
	0.589	2.29		0.621	2.44
	0.611	2.30		0.637	2.45
	0.627	2.30		0.669	2.45
	0.651	2.31		0.685	2.45
	0.665	2.32		0.703	2.44
	0.683	2.32		0.723	2.44
	0.707	2.32		0.749	2.45
	0.721	2.32		0.765	2.45
	0.745	2.32		0.785	2.44
	0.773	2.32		0.803	2.44
	0.791	2.32		0.825	2.45

TABLE VI (Continued)

$S/R_N = 6.54$					
Re_∞, R_N	Y/R_N	P_w/P_o'	Re_∞, R_N	Y/R_N	P_w/P_o'
12,900	0.811	2.32	63,800	0.779	2.41
	0.829	2.33		0.801	2.41
	0.851	2.33		0.819	2.40
	0.867	2.33		0.841	2.41
	0.887	2.33		0.863	2.41
	0.907	2.33		0.881	2.41
	0.931	2.33		0.909	2.41
	0.945	2.33		0.921	2.41
	0.969	2.33		0.939	2.41
	0.925	2.33		0.959	2.41
	0.947	2.33		0.981	2.41
	0.967	2.33		1.00	2.41
	0.991	2.33		1.02	2.41
	1.00	2.34		1.04	2.41
	1.03	2.34		1.06	2.41
	1.04	2.34		1.08	2.41
	1.06	2.34		1.10	2.41
	1.09	2.34		1.13	2.41
	1.11	2.34		1.14	2.41
	1.12	2.34		1.15	2.41
	1.15	2.34		1.18	2.40
	1.16	2.34		1.20	2.40
	1.18	2.34		1.22	2.40
	1.21	2.34		1.24	2.40
	1.22	2.34		1.26	2.41
	1.25	2.33		1.28	2.40
	1.26	2.33		1.30	2.41
	1.28	2.33		1.32	2.41
	1.31	2.33		1.34	2.40
	1.33	2.33		1.36	2.39
	1.35	2.33		1.38	2.36
	1.37	2.33		1.40	2.29
	1.39	2.33		1.42	2.12
	1.40	2.33		1.43	1.97
	1.43	2.32		1.45	1.77
	1.45	2.31		1.45	1.55
	1.47	2.26		1.50	1.55
	1.49	2.18		1.53	0.899
	1.50	2.08		1.61	0.265
	1.52	1.89		1.82	0.250

TABLE VI (Concluded)

$S/R_N = 6.54$		
Re_∞, R_N	Y/R_N	P_w/P_{δ}
12,900	1.54	1.69
	1.56	1.40
	1.58	1.15
	1.60	0.931
	1.63	0.738
	1.64	0.651
	1.67	0.642
	1.69	0.623
	1.70	0.525
	1.73	0.377
	1.74	0.323
	1.77	0.288
	1.78	0.273
	1.81	0.266
	1.83	0.258
	1.85	0.254
	1.86	0.254
	1.88	0.251

TABLE VII
LOW REYNOLDS NUMBER SKIN TEMPERATURE DATA

		Re_∞, 1/in.	126,700	25,800	2974	1290	432
		T_o	1030	920	1040	1674	3005
x/R_N	r/R_N	S/R_N					
			H/.25/45				
0	0	0	0.940	0.860	0.813	0.746	0.500
0.020	0.2	0.203	0.927	0.844	0.808	0.740	0.495
0.077	0.4	0.410	0.921	0.837	0.803	0.722	0.485
0.280	0.8	0.859	0.902	0.825	0.765	0.692	0.429
0.414	1.0	1.100	0.873	0.805	0.765	0.656	0.421
			H/.05/45				
0	0	0	0.943	0.870	0.833	0.776	0.519
0.414	1	1.100	0.908	0.845	0.828	0.764	0.515
1.23	2	2.39	---	---	0.823	0.749	0.506
3.12	4	5.14	0.848	0.786	0.803	0.722	0.482
4.10	5	6.54	---	---	0.784	0.692	0.455
			H/.05/10				
0	0	0	0.877	0.801	0.726	0.674	0.452
2	2.03	2.97	0.872	0.795	0.712	0.659	0.437
4	2.91	5.16	0.868	0.784	0.706	0.656	0.434
6	3.62	7.28	0.863	0.783	0.705	0.644	0.423
8	4.24	9.37	0.855	0.778	0.702	0.635	0.417
10	4.81	11.45	0.795	0.733	0.687	0.623	0.402
12	5.34	13.53	---	---	0.682	0.611	0.390

TABLE VIII
10-DEG HYPERBOLOID DRAG DATA

		M_∞ = 9.92 Re_∞ = 25,800/in.			M_∞ = 9.19 Re_∞ = 2974/in.		
		Uncorrected	Corrected for q_∞		Uncorrected	Corrected for q_∞	
		C_D	C_D	C_D	C_D	C_D	C_D
R_N	R_{B_L}	Based on R_B = 0.300 in.		Based on $R_B=R_{B_L}$	Based on R_B = 0.300 in.		Based on $R_B=R_{B_L}$
0.25	0.300	1.199	1.221	1.221	1.346	1.294	1.294
	0.275	1.007	1.061	1.263	---	---	---
	0.250	---	---	---	---	---	---
	0.225	---	---	---	---	---	---
	0.200	0.5986	0.630	1.418	---	---	---
	0.175	0.481	0.497	1.461	---	---	---
	0.150	0.360	0.372	1.488	---	---	---
	0.125	0.258	0.267	1.538	---	---	---
	0.100	0.160	0.165	1.485	---	---	---
0.15	0.300	0.891	0.881	0.881	1.039	0.999	0.999
0.05	0.300	0.381	0.389	0.389	0.598	0.575	0.575
	0.275	0.345	0.341	0.406	0.523	0.503	0.599
	0.250	0.304	0.311	0.447	0.469	0.451	0.649
	0.225	0.283	0.280	0.498	0.396	0.381	0.677
	0.200	0.230	0.234	0.533	0.357	0.343	0.772
	0.175	0.190	0.196	0.576	0.297	0.286	0.840
	0.150	0.158	0.163	0.652	0.239	0.230	0.920
	0.125	0.122	0.126	0.726	0.179	0.172	0.991
	0.100	0.0809	0.084	0.752	0.140	0.135	1.215

TABLE VIII (Concluded)

		M_∞ = 9.20 Re_∞ = 1790/in.			M_∞ = 9.92 Re_∞ = 432/in.		
		Uncorrected	Corrected for q_∞		Uncorrected	Corrected for q_∞	
		C_D	C_D	C_D	C_D	C_D	C_D
R_N	RB_L	Based on R_B = 0.300 in.		Based on R_B=RB_L	Based on R_B = 0.300 in.		Based on R_B=RB_L
0.25	0.300	1.337	1.269	1.269	1.363	1.306	1.306
	0.275	1.158	1.099	1.308	1.171	1.122	1.335
	0.250	0.986	0.936	1.348	0.962	0.922	1.328
	0.225	0.850	0.807	1.435	0.828	0.793	1.410
	0.200	0.690	0.655	1.474	0.678	0.650	1.463
	0.175	0.542	0.514	1.511	0.546	0.523	1.537
	0.150	0.408	0.387	1.548	0.373	0.357	1.428
	0.125	0.295	0.280	1.613	0.250	0.240	1.382
	0.100	0.196	0.186	1.674	0.149	0.143	1.287
0.15	0.300	1.054	1.000	1.000	1.182	1.133	1.133
0.05	0.300	0.647	0.614	0.614	1.018	0.945	0.945
	0.275	0.585	0.555	0.660	0.885	0.822	0.978
	0.250	0.505	0.479	0.690	0.771	0.716	1.031
	0.225	0.444	0.421	0.748	0.653	0.606	1.077
	0.200	0.377	0.358	0.806	0.557	0.517	1.163
	0.175	0.313	0.297	0.873	0.441	0.410	1.205
	0.150	0.255	0.242	0.968	0.347	0.322	1.288
	0.125	0.194	0.188	1.080	0.246	0.228	1.313
	0.100	0.144	0.140	1.260	0.171	0.159	1.431

TABLE IX
22.5-DEG HYPERBOLOID DRAG DATA

		M_∞ = 9.92 Re_∞ = 25,800/in.			M_∞ = 9.19 Re_∞ = 2974/in.		
		Uncorrected	Corrected for q_∞		Uncorrected	Corrected for q_∞	
		C_D	C_D	C_D	C_D	C_D	C_D
R_N	R_{B_L}	Based on R_B = 0.300 in.		Based on $R_B=R_{B_L}$	Based on R_B = 0.300 in.		Based on $R_B=R_{B_L}$
0.25	0.300	1.181	1.243	1.243	1.354	1.302	1.302
	0.275	1.035	1.090	1.297	---	---	---
	0.250	0.8895	0.937	1.349	---	---	---
	0.225	0.752	0.792	1.408	---	---	---
	0.200	0.601	0.633	1.424	---	---	---
	0.175	0.486	0.502	1.475	---	---	---
	0.150	0.362	0.374	1.496	---	---	---
	0.125	0.259	0.268	1.544	---	---	---
	0.100	0.159	0.164	1.476	---	---	---
0.15	0.300	0.896	0.944	0.944	1.088	1.046	1.046
0.05	0.300	0.533	0.561	0.561	0.746	0.723	0.723
	0.275	0.454	0.478	0.569	0.647	0.631	0.751
	0.250	0.397	0.418	0.602	0.562	0.548	0.789
	0.225	0.337	0.355	0.631	0.484	0.472	0.839
	0.200	0.279	0.294	0.664	0.398	0.388	0.873
	0.175	0.232	0.240	0.705	0.327	0.319	0.937
	0.150	0.181	0.187	0.748	0.265	0.258	1.032
	0.125	0.139	0.144	0.829	0.198	0.193	1.112
	0.100	0.961	0.993	0.894	0.143	0.137	1.251

TABLE IX (Concluded)

		M_∞ = 9.20, Re_∞ = 1790/in.			M_∞ = 9.92, Re_∞ = 432/in.		
		Uncorrected	Corrected for q_∞		Uncorrected	Corrected for q_∞	
		C_D	C_D	C_D	C_D	C_D	C_D
R_N	R_{BL}	Based on R_B = 0.300 in.		Based on $R_B=R_{BL}$	Based on R_B = 0.300 in.		Based on $R_B=R_{BL}$
0.25	0.300	1.349	1.308	1.308	1.447	1.344	1.344
	0.275	1.177	1.141	1.358	1.185	1.135	1.351
	0.250	1.010	0.979	1.410	1.088	1.016	0.454
	0.225	0.826	0.801	1.424	0.809	0.775	1.378
	0.200	0.659	0.639	1.438	0.674	0.653	1.514
	0.175	0.545	0.528	1.552	0.508	0.487	1.431
	0.150	0.412	0.399	1.596	0.375	0.359	1.436
	0.125	0.296	0.287	1.653	0.259	0.248	1.428
	0.100	0.192	0.186	1.674	0.185	0.171	1.534
0.15	0.300	1.120	1.086	1.086	1.287	1.194	1.194
0.05	0.300	0.776	0.752	0.752	1.149	1.059	1.059
	0.275	0.702	0.681	0.810	0.887	0.850	1.012
	0.250	0.612	0.593	0.854	0.832	0.773	1.113
	0.225	0.514	0.498	0.885	0.673	0.645	1.147
	0.200	0.436	0.423	0.952	0.563	0.536	1.203
	0.175	0.351	0.340	0.999	0.451	0.440	1.293
	0.150	0.279	0.271	1.084	0.387	0.340	1.442
	0.125	0.211	0.205	1.181	0.220	0.215	1.238
	0.100	0.148	0.143	1.287	0.178	0.157	1.409

TABLE X
45-DEG HYPERBOLOID DATA

		M_∞ = 9.92, Re_∞ = 25,000/in.			M_∞ = 9.19, Re_∞ = 2974/in.		
		Uncorrected	Corrected for q_∞		Uncorrected	Corrected for q_∞	
		C_D	C_D	C_D	C_D	C_D	C_D
R_N	R_{B_L}	Based on R_B = 0.300 in.		Based on $R_B=R_{B_L}$	Based on R_B = 0.300 in.		Based on $R_B=R_{B_L}$
0.25	0.300	1.362	1.411	1.411	1.499	1.441	1.441
	0.275	1.152	1.194	1.421	---	---	---
	0.250	0.973	1.008	1.452	---	---	---
	0.225	0.795	0.728	1.470	---	---	---
	0.200	0.642	0.665	1.496	---	---	---
	0.175	0.500	0.518	1.522	---	---	---
	0.150	0.375	0.389	1.556	---	---	---
	0.125	0.261	0.270	1.555	---	---	---
	0.100	0.158	0.164	1.476	---	---	---
0.20	0.300	1.307	1.354	1.354	1.442	1.386	1.386
	0.240	0.8732	0.905	1.414	0.951	0.914	1.428
0.15	0.300	1.242	1.287	1.287	1.386	1.333	1.333
	0.180	0.487	0.505	1.403	0.551	0.530	1.472
0.10	0.300	1.176	1.219	1.219	1.346	1.294	1.294
0.05	0.300	1.146	1.197	1.197	1.322	1.271	1.271
	0.275	0.974	1.018	1.210	---	---	---
	0.250	0.790	0.832	1.198	---	---	---
	0.225	0.686	0.723	1.285	---	---	---
	0.200	0.510	0.537	1.208	---	---	---
	0.175	0.400	0.413	1.214	---	---	---
	0.150	0.292	0.302	1.208	---	---	---
	0.125	0.200	0.207	1.192	---	---	---
	0.100	0.130	0.134	1.206	---	---	---

TABLE X (Concluded)

		M_∞ = 9.20 Re_∞ = 1790/in.			M_∞ = 9.92 Re_∞ = 432/in.		
		Uncorrected	Corrected for q_∞		Uncorrected	Corrected for q_∞	
		C_D	C_D	C_D	C_D	C_D	C_D
R_N	R_{B_L}	Based on R_B = 0.300 in.		Based on $R_B=R_{B_L}$	Based on R_B = 0.300 in.		Based on $R_B=R_{B_L}$
0.25	0.300	1.523	1.450	1.444	1.648	1.532	1.532
	0.275	1.288	1.231	1.465	1.413	1.314	1.564
	0.250	1.078	1.031	1.485	1.196	1.112	1.601
	0.225	0.938	0.895	1.591	0.962	0.894	1.589
	0.200	0.707	0.674	1.517	0.793	0.737	1.658
	0.175	0.563	0.536	1.575	0.610	0.567	1.666
	0.150	0.424	0.404	1.616	0.447	0.416	1.664
	0.125	0.305	0.290	1.671	0.311	0.289	1.665
	0.100	0.217	0.207	1.859	0.190	0.177	1.593
0.20	0.300	1.454	1.384	1.381	1.633	1.518	1.518
	0.240	0.997	0.948	1.481	1.080	1.004	1.568
0.15	0.300	1.405	1.334	1.334	1.617	1.459	1.459
	0.180	0.558	0.531	1.475	0.637	0.620	1.725
0.10	0.300	1.356	1.288	1.288	1.512	1.417	1.417
	0.300	1.392	1.317	1.317	1.415	1.380	1.380
	0.275	1.128	1.071	1.274	1.202	1.173	1.396
	0.250	0.930	0.883	1.272	0.952	0.929	1.338
	0.225	0.770	0.731	1.300	0.860	0.839	1.492
	0.200	0.616	0.585	1.316	0.687	0.670	1.508
	0.175	0.484	0.460	1.352	0.523	0.510	1.499
	0.150	0.360	0.342	1.368	0.377	0.368	1.472
	0.125	0.275	0.266	1.532	0.245	0.239	1.377
	0.100	0.174	0.168	1.512	0.149	0.145	1.305

TABLE XI
PARABOLOID DRAG DATA

		M_∞ = 9.92 Re_∞ = 25,800/in.			M_∞ = 9.19 Re_∞ = 2974/in.		
		Uncorrected	Corrected for q_∞		Uncorrected	Corrected for q_∞	
		C_D	C_D	C_D	C_D	C_D	C_D
R_N	R_{B_L}	Based on R_B = 0.300 in.		Based on R_B=R_{B_L}	Based on R_B = 0.300 in.		Based on R_B=R_{B_L}
0.10	0.300	0.562	0.592	0.592	0.797	0.766	0.706
	0.275	0.510	0.537	0.639	0.717	0.699	0.832
	0.250	0.462	0.487	0.701	0.637	0.621	0.894
	0.225	0.408	0.430	0.764	0.547	0.533	0.948
	0.200	0.356	0.375	0.844	0.474	0.462	1.040
	0.175	0.304	0.314	0.923	0.396	0.386	1.134
	0.150	0.247	0.257	1.028	0.316	0.308	1.232
	0.125	0.186	0.192	1.106	0.238	0.232	1.336
	0.100	0.127	0.131	1.179	0.172	0.168	1.512
0.15	0.300	0.795	0.837	0.837	0.991	0.952	0.952
0.20	0.300	0.993	1.046	1.046	1.185	1.139	1.139
0.25	0.300	1.134	1.194	1.194	1.313	1.261	1.261
	0.275	0.997	1.050	1.250	---	---	---
	0.250	0.857	0.903	1.300	---	---	---
	0.225	0.725	0.764	1.358	---	---	---
	0.200	0.598	0.630	1.418	---	---	---
	0.175	0.482	0.498	1.464	---	---	---
	0.150	0.336	0.347	1.388	---	---	---
	0.125	0.257	0.266	1.532	---	---	---
	0.100	---	---	---	---	---	---

TABLE XI (Concluded)

		M_∞ = 9.20 Re_∞ = 1790/In.			M_∞ = 9.92 Re_∞ = 432/In.		
		Uncorrected	Corrected for q_∞		Uncorrected	Corrected for q_∞	
		C_D	C_D	C_D	C_D	C_D	C_D
R_N	R_{B_L}	Based on R_B = 0.300 In.		Based on R_B=R_{B_L}	Based on R_B = 0.300 In.		Based on R_B=R_{B_L}
0.10	0.300	0.795	0.771	0.771	1.158	1.076	1.076
	0.275	0.746	0.723	0.860	1.010	0.939	1.117
	0.250	0.672	0.652	0.939	0.909	0.842	1.213
	0.225	0.583	0.565	1.004	0.805	0.748	1.330
	0.200	0.500	0.485	1.091	0.650	0.608	1.359
	0.175	0.413	0.400	1.176	0.533	0.496	1.458
	0.150	0.323	0.313	1.252	0.397	0.369	1.476
	0.125	0.243	0.237	1.365	0.289	0.269	1.549
	0.100	0.166	0.162	1.458	0.190	0.177	1.593
0.15	0.300	1.010	0.986	0.986	1.325	1.232	1.232
0.20	0.300	1.171	1.143	1.143	1.416	1.316	1.316
0.25	0.300	1.300	1.269	1.269	1.525	1.418	1.418
	0.275	1.134	1.107	1.317	1.356	1.261	1.501
	0.250	0.967	0.944	1.359	1.152	1.071	1.542
	0.225	0.813	0.794	1.412	0.953	0.886	1.575
	0.200	0.678	0.662	1.490	0.792	0.736	1.656
	0.175	0.533	0.520	1.528	0.618	0.575	1.690
	0.150	0.409	0.399	1.596	0.464	0.431	1.724
	0.125	0.292	0.285	1.642	0.328	0.305	1.757
	0.100	0.192	0.187	1.683	0.213	0.198	1.782

TABLE XII
CORRECTED NORMALIZED PRESSURE DATA, p_w/p_o'

		M_∞	10.12*	9.92*	9.19	9.20	9.92
		Re_∞, 1/in.	127,600	25,800	2974	1790	432
z	r_w	S					
			H/.05/10				
-4.00	2.92	5.16	0.145	0.163	0.191	0.191	0.181
-6.00	3.62	7.29	0.113	0.129	0.137	0.154	0.144
-9.00	4.52	10.42	0.0888	0.102	0.111	0.123	0.113
-13.00	5.59	14.56	0.0744	0.0847	0.111	0.119	0.113
			H/.25/10				
0.0799	0.400	0.410	0.889	0.888	0.888	0.869	0.861
0.179	0.600	0.634	0.763	0.764	0.769	0.774	0.746
0.318	0.800	0.878	0.651	0.656	0.674	0.675	0.638
0.496	1.00	1.15	0.528	0.535	0.554	0.541	0.557
			H/.05/22.5				
3.00	2.75	4.22	0.254	0.270	0.307	0.303	0.281
4.00	3.28	5.33	0.230	0.246	0.274	0.270	0.251
6.00	4.26	7.57	0.206	0.219	0.249	0.227	0.226
8.00	5.19	9.78	0.192	0.202	0.217	0.221	0.194
			H/.05/45				
1.08	1.83	2.16	0.642	0.658	0.698	0.694	0.621
2.08	2.91	3.64	0.612	0.633	0.654	0.637	0.597
3.08	3.95	5.08	0.608	0.626	0.641	0.623	0.595
4.08	4.98	6.52	0.600	0.606	0.557	0.599	0.524
			H/.25/45				
0.020	0.200	0.201	0.919	0.916	---	0.906	0.849
0.166	0.600	0.629	0.855	0.852	0.860	0.848	0.792
0.281	0.800	0.859	0.780	0.781	0.774	0.773	0.709
0.356	0.916	0.997	0.752	0.746	0.736	0.727	0.662

TABLE XII (Concluded)

		M_∞	10.12*	9.92*	9.19	9.20	9.92
		Re_∞, 1/in.	127,600	25,800	2974	1790	432
z	r_w	S					
			P/.10				
1.00	1.42	1.80	0.349	0.368	0.417	0.396	0.391
2.00	2.00	2.96	0.220	0.233	0.265	0.260	0.261
3.00	2.45	4.06	0.163	0.174	0.207	0.200	0.213
4.00	2.83	5.13	0.130	0.140	0.178	0.191	0.156
			P/.25				
0.080	0.400	0.410	0.887	0.892	0.870	0.870	0.858
0.180	0.600	0.634	0.765	0.768	0.785	0.757	0.744
0.320	0.800	0.879	0.646	0.649	0.679	0.658	0.641
0.500	1.000	1.15	0.544	0.554	0.584	0.550	0.525

*No corrections required to Tunnel C data.

TABLE XIII
UNCORRECTED NORMALIZED PRESSURE DATA

		M_∞	9.19	9.20	9.92
		Re_∞, 1/in.	2974	1790	432
z	r_w	S			
			H/.05/10		
4.00	2.92	5.16	0.172	0.165	0.125
6.00	3.62	7.29	0.119	0.129	0.0930
9.00	4.52	10.42	0.0942	0.0990	0.0707
13.00	5.59	14.56	0.0942	0.0956	0.0716
			H/.25/10		
0.0799	0.400	0.410	0.876	0.853	0.794
0.179	0.600	0.634	0.755	0.757	0.678
0.318	0.800	0.878	0.659	0.657	0.568
0.496	1.00	1.15	0.538	0.521	0.440
			H/.05/22.5		
3.00	2.75	4.22	0.290	0.280	0.219
4.00	3.28	5.33	0.257	0.247	0.191
6.00	4.26	7.57	0.231	0.203	0.169
8.00	5.19	9.78	0.200	0.198	0.143
			H/.05/45		
1.08	1.83	2.16	0.673	0.675	0.546
2.08	2.91	3.64	0.638	0.617	0.524
3.08	3.95	5.08	0.625	0.604	0.522
4.08	4.98	6.52	0.541	0.580	0.451
			H/.25/45		
0.020	0.200	0.201	---	0.890	0.783
0.166	0.600	0.629	0.848	0.833	0.728
0.281	0.800	0.859	0.760	0.758	0.644
0.356	0.916	0.997	0.723	0.710	0.597

TABLE XIII (Concluded)

		M_∞	9.19	9.20	9.92
		Re_∞, 1/in.	2974	1790	432
z	r_w	S			
			P/.10		
1.00	1.42	1.80	0.391	0.375	0.321
2.00	2.00	2.96	0.248	0.236	0.196
3.00	2.45	4.06	0.189	0.176	0.153
4.00	2.83	5.13	0.146	0.144	0.106
			P/.25		
0.080	0.400	0.410	0.849	0.854	0.790
0.180	0.600	0.634	0.772	0.740	0.674
0.320	0.800	0.879	0.664	0.641	0.571
0.500	1.000	1.15	0.553	0.531	0.452

UNCLASSIFIED

Security Classification

DOCUMENT CONTROL DATA - R & D

(Security classification of title, body of abstract and indexing annotation must be entered when the overall report is classified)

1 ORIGINATING ACTIVITY *(Corporate author)*
Arnold Engineering Development Center
ARO, Inc., Operating Contractor
Arnold Air Force Station, Tennessee

2a. REPORT SECURITY CLASSIFICATION
UNCLASSIFIED

2b. GROUP
N/A

3. REPORT TITLE

AN EXPERIMENTAL INVESTIGATION OF SURFACE CONDITIONS ON HYPERBOLOIDS AND PARABOLOIDS AT A MACH NUMBER OF 10

4. DESCRIPTIVE NOTES *(Type of report and inclusive dates)*
April 1967 through January 1969 - Final Report

5 AUTHOR(S) *(First name, middle initial, last name)*

Herbert R. Little, ARO, Inc.

6 REPORT DATE	7a. TOTAL NO. OF PAGES	7b. NO. OF REFS
January 1970	138	30

8a. CONTRACT OR GRANT NO	9a. ORIGINATOR'S REPORT NUMBER(S)
F40600-69-C-0001	
b. PROJECT NO 8953	AEDC-TR-69-225
c. Program Element 62201F	9b. OTHER REPORT NO(S) *(Any other numbers that may be assigned this report)*
d. Task 03	N/A

10. DISTRIBUTION STATEMENT

This document has been approved for public release and sale; its distribution is unlimited.

11. SUPPLEMENTARY NOTES	12 SPONSORING MILITARY ACTIVITY
Available in DDC	Arnold Engineering Development Center, Air Force Systems Command Arnold Air Force Station, Tenn.

13. ABSTRACT

Data on analytic bodies are presented for Reynolds numbers from 22 to 65,000 (based on model nose radius) at a Mach number of 10. The test bodies are hyperboloids having asymptotic half-angles of 10, 22.5, and 45 deg and paraboloids; data are presented for steady-state skin temperatures, surface pressures, drag, and total skin friction. Shock-layer pitot pressure distributions are presented for two hyperboloids at selected Reynolds numbers. The results include an assessment of the modified Newtonian impact theory for use in inviscid pressure distributions. The effects of viscous interactions on skin temperature, pressure, drag, and skin friction are examined. Comparisons with numerical results of second-order boundary-layer and fully viscous shock-layer theories are made.

DD FORM 1 NOV 65 1473

UNCLASSIFIED

Security Classification

14. KEY WORDS	LINK A		LINK B		LINK C	
	ROLE	WT	ROLE	WT	ROLE	WT
hyperbolas						
parabolas						
geometric surfaces						
skin friction						
pressure measurement						
drag						
temperature measurement						
pressure distribution						
viscosity						